ELECTRON CORRELATION EFFECTS ON RELAXATION AND DECOHERENCE TIMES IN A QUANTUM DOT

by

Catherine J. Stevenson

Submitted in partial fulfillment of the
requirements for the degree of
Doctor of Philosophy

at

Dalhousie University
Halifax, Nova Scotia
September 2014

Table of Contents

List of Figures

Abstract

We use density matrix theory to calculate decay rates of lowest-lying eigenstates in rotationally symmetric quantum dots (QDs). Specifically, we investigate relaxation and decoherence times in single-electron and three-electron systems, where in the latter Coulomb interaction is included. Both systems are studied with and without Rashba and Dresselhaus spin-orbit (SO) effects. Two SO strengths are investigated: A small strength which is more typical of GaAs QDs and a larger strength to better reveal the influence of SO on decay rates. In the single-electron case we consider three different types of electron-phonon interactions as a source of decay: The deformation potential by longitudinal acoustic phonons (LA-DP), and the piezoelectric effect by both longitudinal acoustic phonons (LA-PZ) and transverse acoustic phonons (TA-PZ). When SO is not included the system is a simple 2-level system, independent of spin. Decay times are studied as a function of both confinement frequency (ω_0) and magnetic field (B). Depending on system parameters, either LA-DP or TA-PZ can be the dominant source of decay. When SO is included in the model, the system becomes a four-level system and additional decay channels open due to the additional number of levels in the subspace. In the strong-SO regime the relaxation rates of the single-electron case are reduced by as much as 0.5 ns^{-1} and the decoherence rates by as much as 1 ns^{-1}. In the three-electron QD decay rates are investigated as a function of B. The TA-PZ interaction is primarily investigated as it is found to be the main source of decay for the majority of the B field investigated. Correlation effects on decay rates are isolated from energy effects, revealing that Coulomb-induced correlations between electrons play a significant role in reducing decay rates. We find that for the parameters investigated in this dissertation, SO does not, on average, reduce the peak relaxation rates in the three-electron system, rather it shifts them towards higher magnetic fields.

List of Abbreviations and Symbols Used

2DEG	Two-dimensional electron gas
$\hat{a}, \hat{b}$	Bose annihilation operators
$\hat{a}^\dagger, \hat{b}^\dagger$	Bose creation operators
$\mathbf{A}(\hat{\mathbf{r}})$	Vector potential
α_R	Rashba spin-orbit constant
$\mathbf{B}$ (B_z)	Magnetic field, $\mathbf{B} = B_z$
$\hat{b}_{\mathbf{k}}$	Second quantization Bose annihilation operator
$\hat{b}^\dagger_{\mathbf{k}}$	Second quantization Bose creation operator
β_D	Dresselhaus spin-orbit constant
c	Speed of light
c_ν	Speed of sound for polarization ν
c_{LA}	Speed of sound of the longitudinal acoustic phonon mode
c_{TA}	Speed of sound of the transverse acoustic phonon mode
$\hat{c}_i$	Second quantization Fermi annihilation operator
$\hat{c}^\dagger_i$	Second quantization Fermi creation operator
$C_z(r)$, C	Chirality number of meron state
d	Semiconductor density
D	Deformation constant
δ_{ij}	Kronecker delta
$\delta(x)$	Dirac delta function
e	Magnitude of electron charge
$\varepsilon_{n\,m}$	Single-particle state energy
ϵ	Dielectric constant
ΔE_C	Conduction band energy difference at heterostructure interface; Confinement energy of quantum well
F_i	General reservoir operator in the interaction Hamiltonian
$\hat{\Psi}_s(\hat{r}), \hat{\Psi}^\dagger_s(\hat{r})$	Field operators
g	Electron g-factor

γ	Bulk Dresselhaus coefficient
h_{14}	Piezoelectric constant
$\hbar$	Reduced Planck's constant
$\hat{h}$	Single particle (two-dimensional harmonic oscillator) Hamiltonian
$\hat{H}_{QD}$	Many-body interacting Hamiltonian
$\hat{H}_{SO}$	Spin-orbit Hamiltonian
$\mathbf{k}$	Electron wave vector
l_0	Effective length scale of the electron wave function in a quantum dot
ℓ_z	Width of quantum well
$\hat{L}_z$	Operator for the z-component of the orbital angular momentum
$L_n^{(\alpha)}(x)$	Generalized Laguerre polynomial
LA-DP	Deformation potential electron-phonon interaction due to longitudinal acoustic phonons
LA-PZ	Piezoelectric electron-phonon interaction due to longitudinal acoustic phonons
LLL	Lowest Landau level
λ_q	Phonon wavelength
m_e	Mass of electron
m^*	Effective mass of electron
m'	Azimuthal quantum number of orbital wave function in position-space
$M_\nu(\mathbf{q})$	Matrix element of the electron-phonon interaction of type ν ($\nu = \{$LA-DP, LA-PZ, TA-PZ$\}$)
MDD	Maximum density droplet
μ_B	Bohr magneton
n, m	Orbital quantum numbers
n'	Principle quantum number of orbital wave function in position-space
n_r	Radial quantum number of orbital wave function in position-space
N	Number of particles
NMR	Nuclear magnetic resonance
ν	Electron filling factor of Landau levels in a 2D electron system
$\xi(z)$	Ground state of quantum well

$\hat{\mathbf{p}}$	Momentum operator, $\hat{\mathbf{p}} = (\hat{p}_x, \hat{p}_y)$
$\widehat{\boldsymbol{P}}$	Canonical momentum operator, $\widehat{\boldsymbol{P}} = \hat{\boldsymbol{p}} + \frac{e}{c}\boldsymbol{A}\left(\hat{\boldsymbol{r}}\right)$
$\phi_{nm}(r,\theta)$	Position-space representation of an orbital
$\mathbf{q}$	Phonon wave vector
Q	Topological charge of meron state
Q_i	General quantum system operator in the interaction Hamiltonian
QD	Quantum dot
$\hat{\mathbf{r}}$	Position operator, $\hat{\mathbf{r}} = (\hat{x}, \hat{y})$
r	Radial component of two dimensional polar coordinate system
$R_{m'mn'n}$	Redfield tensor matrix element
$\rho(t)$	Density matrix
$\rho(t)_{m'm}$	Density matrix element
$\hat{\boldsymbol{S}}(\boldsymbol{r})$	Spin-density operator
$\hat{S}^2$	Spin angular moment operator
$\hat{S}_z$	Operator for the z-component of the spin angular momentum
SO	Spin-orbit
SP state	Single-particle state
$\sigma_x, \sigma_y, \sigma_z$	Pauli spin matrices
T	Temperature
T_1	Relaxation time of the QD system
T_2	Decoherence time of the QD system
T_ϕ	Dephasing time of the QD system
TA-PZ	Piezoelectric electron-phonon interaction due to transverse acoustic phonons
tr_R	Partial trace over reservoir R
θ	Angular component of two dimensional polar coordinate system
τ	Reservoir correlation time
V	Volume of semiconductor
V	General interaction Hamiltonian
ω_0	Confinement frequency of quantum dot
ω_c	Cyclotron frequency

ω	Characteristic frequency, equal to $\sqrt{\omega_0^2 + \frac{1}{4}\omega_c^2}$
ω_{mn}	Frequency difference between quantum states m and n, $\omega_{mn} = (E_m - E_n)/\hbar$
$\Omega_\pm$	Characteristic frequencies of the two-dimensional harmonic oscillator

Acknowledgements

This project was made possible by financial support from the Natural Sciences and Engineering Research Council of Canada (NSERC), Dalhousie University, and Lockheed Martin.

I would like to thank my supervisor, Professor Jordan Kyriakidis, for his support, guidance, and patience in my completion of this endeavour. I would like to thank Eduardo Vaz and all other Kyriakidis group members, past and present, for sharing this experience with me. I would like to thank the administrative staff in the Department of Physics and Atmospheric Science, past and present, for all of their assistance during my time as a student. I would like to thank my parents, Jav and Carol Stevenson, for believing in me that I could do this. And finally, I would like to thank my husband, Jock Smith, and my little helpers, Oren and Laurel; I would have never finished my PhD without their unwaivering support.

Halifax, September 2014

Catherine J. Stevenson

Chapter 1

Introduction

This dissertation investigates the existence of long-lived quantum states in semiconductor quantum dot (QD) systems. We study the lifetimes of both correlated charge states and correlated spin states and compare them against the lifetimes of uncorrelated single-particle states. The correlated charge states investigated in this work are the two lowest energy eigenstates of an interacting three-electron QD system. The correlated spin states investigated in this work are topological states called merons and can be found in both single-electron and multielectron QDs. The QD system is coupled to a phonon reservoir and the evolution of the system is examined. We expect a correlated QD state to be more robust against system perturbations and therefore longer-lived than an uncorrelated QD state. Such a state could be exploited for use in a quantum computing scheme. A brief literature review of QDs and QD quantum computing is given in Section 1.1. An introduction to topological spin states is given in Section 1.2.

1.1 Semiconductor Quantum Dots and Quantum Computing

The miniaturization of standard computer CPUs will ultimately be limited by the emergence of quantum effects in the system. This impediment can be taken advantage of to develop a new type of computing scheme, namely quantum computing. A significant advantage of quantum computers over their classical counterparts is the expected speed-up in problem-solving times of up to exponential order for difficult problems such as the factoring of large numbers [1].

Semiconductor QDs are a potential platform for quantum computing due to their scalability [2–4] and the already existing infrastructure for fabricating semiconductor materials. A QD can be thought of as an artificial atom [5] housed in a semiconductor material which can capture a controllable number of electrons [6]. The QD can serve as a transistor in the quantum computer [7,8]. QD states used for this implementation must be long lived relative to the time-scales required to execute quantum algorithms, and remain coherent against system perturbations. A natural logical quantum bit, or qubit, in the QD transistor can be formed from either the spin or the charge of the electron. Both have their advantages and disadvantages. Spin is an intrinsic property of electrons and can exist in a superposition of different states, that is the electron can be in both a spin-up state and a spin-down state at the same time. Spin states of electrons confined in semiconductor QDs are an appealing platform in quantum computing due to their long dephasing times and controllability [9–12]. The use of pump-probe laser spectroscopy for state set-up and measurement allows for the manipulation of spin qubits on picosecond and femtosecond timescales [13–16]. Spin states are not impervious to noise. They can couple to the nuclear spins of the host semiconductor material, impurities in the semiconductor, or local magnetic fields, all of which can affect the lifetimes of the states. Electrons are also characterized by another intrinsic property, charge. Charge-based qubits can be readily manipulated by electrical pulses on electrodes placed near to the QD. The lifetimes of charge qubits are usually limited by the fast relaxation and decoherence rates of electronic charge states and can present a bottleneck for their use in quantum computing algorithms, though there are new techniques using shaped electrical pulses for controlling charge qubits on a picosecond scale [17]. For both spin states and charge states, those states with high degrees of correlation, such as those in a multielectron QD, have been shown to have longer lifetimes than states in a single-electron QD [18–20].

In this dissertation the theory developed is based on a semiconductor lateral QD platform. Lateral QDs are electrostatically defined QDs in semiconductor heterostructures. They are created using electron beam lithography, a process whereby a pattern of metal electrodes, or gates, with a resolution of tens of nanometers is formed on the surface of a semiconductor crystal. This semiconductor material is first deposited onto another different semiconductor material; excess electrons are confined between the two crystals by the difference in the conduction band energies of the two semiconductor materials [21]. These confined electrons form a two-dimensional electron gas (2DEG) between the two semiconductor materials. Voltages applied to the surface gates produce an electric field that is felt by the 2DEG below, forming a potential well that traps electrons from the 2DEG current into the QD. Electrical pulses applied to these gates can be used to manipulate the states of the electrons in the QD.

To meet the criteria for scalable quantum computing, qubit states must be well-defined, reliably prepared, and readily measured [1]. Charge qubits are advantageous in that the difference in energies between the ground state system (where the qubit is defined) and the remaining electron states can be relatively large, leaving the qubit states well decoupled from the remainder of the states. With respect to control, the number of electrons trapped in the lateral QD, and the electromagnetic landscape experienced by the electrons therein, is precisely controlled by tuning the voltages across the metal gates [22–24]. States can be differentiated in a QD using experimental techniques such as photoluminescence excitation spectroscopy [25] and magnetoconductance measurements [26]. Another important criterion is that qubit states must be able to undergo coherent evolution for the application of quantum logic operations. This requirement imposes a lower limit on the coherent lifetime of the states; they must be much longer than the time required to perform quantum logic operations. Unfortunately, the electron charge is more susceptible to couple to sources of noise found in the semiconductor environment, such as phonons and electrical noise, which shortens the lifetimes of the states. At low temperature (T≈100 mK or less) the relaxation process of QD states with energy scales on the order of millielectronvolts has been experimentally shown to be dominated by spontaneous emission of acoustic phonons [18, 27, 28], with single-electron relaxation rates on the order of a few nanoseconds [18, 29, 30]. However, highly correlated states may have reduced decay rates. Numerical works indicate that the lifetimes of electronic states can be improved by as much as an order of magnitude in multielectron systems where Coulomb interactions increase the degree of spatial correlation of the states [19, 20].

Creating qubits out of spin states in a QD presents an alternative to charge qubits. There is a collection of advantages which make using a spin-based lateral QD platform viable for quantum computing. Spin qubits do not couple as readily to the environment as charge qubits, making them more resilient to noise. Coupling between spin qubits in adjacent QDs can be controlled by the same electrostatic metal gates which define the lateral QDs. The individual spin of an electron in a lateral QD can be coherently controlled. Also, the relaxation and decoherence times of the spin states are continually being improved. Presently, the lifetime of a spin state in a

QD system is on the order of nanoseconds to microseconds [29,31–33]. By applying electric field pulses to electrons in QDs, the electron spins can be coherently manipulated on a nanosecond timescale [34,35]. Using ultrafast optical pulses, single qubit operation times have been further reduced to the picosecond and even femtosecond timescales [13–16]. Petta *et al.* (2005) (Ref. [32]) have demonstrated a 180 ps two-qubit exchange gate between two electron spins in a double quantum dot. With qubit operation times on the order of a hundred picoseconds, a decoherence time on the order of a microsecond would allow for about 10^4 operations to be performed within the coherent lifetime of the spin qubit.

Amasha *et al.* (Ref. [36]) have shown that through the manipulation of the gate voltages the spin relaxation rate of a single trapped electron can be controlled, enabling one to vary the relaxation rate by over an order of magnitude. In this same work, the spin relaxation time at low magnetic field (near 1 T) has been measured to be greater than 1 s. In addition to having long relaxation lifetimes, the evolution of the spin state must be coherently controlled and the final state must be measurable in order to perform meaningful quantum algorithms. Koppens *et al.* (Ref. [34]) have demonstrated the coherent manipulation of the spin state of a single electron in a double lateral quantum dot for a timescale of 1 μs by exposing the spin to short bursts of an oscillating magnetic field. The final state is read-out by measuring the current (or lack-there-of) through the QD. Press *et al.* (Ref. [33]) have also investigated the coherence of the spin of an electron in a single QD. Using an all-optical spin-echo technique, they reversed the dephasing of the electron spin due to the hyperfine interaction of the surrounding bath of nuclear spins. They pushed the decoherence time of the spin qubit to as long as several microseconds. Information that is stored in the spin qubit lasts for the entire decoherence time of the qubit. In theory, a coherent lifetime on the order of microseconds is just long enough to perform some large-scale quantum algorithms [1].

Despite the above mentioned breakthroughs, the lifetime of a state in a semiconductor QD can be impeded by many things including vibrations in the semiconductor material, the hyper-fine interaction with the nuclear spin of atoms in the semiconductor, and electromagnetic fluctuations in the local environment. A longer-lived, more robust state is therefore desirable for implementing quantum algorithms. We expect that correlated states will fill this role. In general the effect of Coulomb interaction between the electrons in a QD has been shown to increase the relaxation time of the QD system, making the excited state longer lived than that of a non-interacting QD system [19, 20]. Coulomb interaction affects the system in two ways: It increases the degree of spatial correlation in the electronic states, and it changes the energy levels of the system. It is not clear what impact the correlations alone have on improving the relaxation times in a fully-interacting QD system. In Ref. [20] Climente *et al.* calculate the rate of relaxation between the first excited state and the ground state in fully-interacting QD systems containing between two and five electrons. They find that the fully-interacting systems have longer lifetimes than the uncorrelated single-electron system, and attribute this finding to both the change in transition energies between the fully-interacting states and the Coulomb-induced correlation within the fully-interacting states. They do not isolate the Coulomb-induced correlation effects from the Coulomb-induced energy effects on the relaxation rates in the fully-interacting system.

In Ref. [19] Bertoni *et al.* investigate the effects of Coulomb-induced correlations on relaxation rates in the following ways. They first consider a fully interacting two-electron system and compare the relaxation rate from the first excited state of the system to the ground state by *artificially* fixing the transition energy between the states to be the single-electron transition energy. In this case they find no significant change in the relaxation rate from when the true (interacting) state energies are used in the rate calculation. Then, for systems containing between two and six fully-interacting electrons, they compare the relaxation between any two of the first 20 lowest-energy eigenstates with the relaxation between the first excited state and the ground state in a single-electron system where the transition energy in the single-electron case is either the usual single-electron transition energy, or fixed to represent the energy difference between the same orbitals in the fully-interacting case. Generally speaking they find a reduction in the relaxation rates of the many-electron systems when compared to the single-electron cases, however by comparing the relaxation rates of a many-electron system with those for a single-electron system the correlation effect within each many-electron system are not strictly separated from the overall effects of Coulomb interaction. In this dissertation we disentangle the effect of state correlation from the effect of the transition energy on the relaxation rates of a QD system with Coulomb interaction without artificially fixing any of the the parameters of the system. Furthermore, we wish to compare this effect within a system where the number of electrons stays the same, instead of comparing it only to the relaxation rates of a single-electron system. This is because the addition of electrons to the QD changes the orbital configuration of the state and, even in the non-interacting (uncorrelated) limit, can introduce new relaxation channels between the orbitals which may not exist in the single-electron system. We will show that correlations alone play a significant role in reducing the relaxation rates in a many-electron QD system.

Another type of correlated state is a topological qubit state. This state is advantageous in that it should be resilient to local disturbances in the system that might otherwise shorten the lifetime of the state. A promising candidate for the topological qubit in a lateral QD is the meron spin texture, and is described in the proceeding section.

1.2 Topological Spin Textures in Quantum Dots

In general, a topological state is defined by having properties which remain unchanged under a continuous deformation of the system. Topological states are promising candidates for quantum computing in that they are expected to have long decoherence times due to their global correlations, and should be robust against local perturbations [37]. A meron is a topological spin texture characterized by a centralized "up" or "down" spin which smoothly transitions into an in-plane winding away from the central spin. Four orthogonal meron states are illustrated in Fig. 1.1.

Vortices, skyrmions, and merons are examples of topological spin textures that are predicted to form in 2DEG systems [38–40]. (Note these spin textures also form in bosonic systems, but this dissertation will be restricted to discussions in fermionic systems.) Vortices can appear inside a QD when an external magnetic field is applied perpendicular to the plane of the QD [41–43]. The external field causes the electrons in the QD to orbit. As the magnetic field is increased beyond the formation of the spin-polarized maximum density droplet (MDD)[1] in the system, vortices begin to

---

[1] The maximum density droplet occurs at finite magnetic field when all of the spins in the system

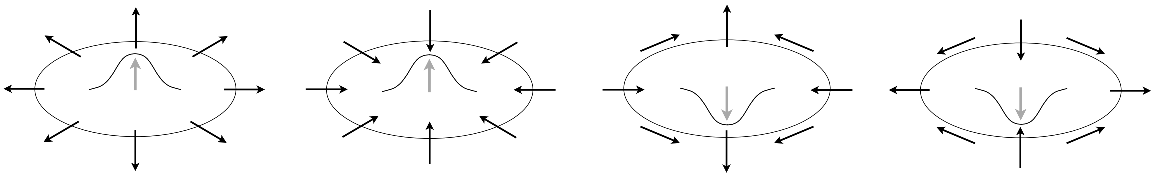

Figure 1.1: Cartoon of four orthogonal meron configurations.

appear, one by one, in the QD. These vortices are manifested as charge currents circulating about voids in the particle density.

Saarikoski *et al.* (Ref. [41]) have studied a two-dimensional (2D) parabolic QD in strong magnetic fields (B $\sim$ 5 T to B $\sim$ 22 T) which contained as few as 6 and as many as 24 electrons using mean-field density functional theory (DFT) and exact diagonalization (ED) with the lowest Landau level (LLL) approximation. The strengths of the magnetic field used were such that the filling factor ν (the ratio of electrons to magnetic flux quanta) ranged from $\nu = 1$ to $\nu = \frac{1}{3}$. As the magnetic field was increased, the orbital angular momentum of the ground state increased in a step-wise manner; the start of each plateau in the orbital angular momentum was associated with the materialization of an additional vortex to the system. These vortices are detectable as zeros in the electron wave function, or as depressions in plots of the electron densities, as determined using ED and DFT, respectively. Their interpretation of the DFT solution was that the external magnetic field penetrates the electron density at these vortices, inducing current to rotate around them. Saarikoski and Harju (Ref. [42]) further developed a theory by which to experimentally test vortex formation in a QD. Specifically, the emergence of vortices beyond the MDD regime should appear as peaks in the chemical potential of the QD as a function of increasing magnetic field.

Skyrmions are spin textures that are characterized by a central spin perpendicular to the 2D plane which transitions smoothly into a spin arrangement along its boundary that is antiparallel to the central spin. Skyrmion quasiparticle excitations in bulk systems have been predicted in the $\nu = 1$ quantum Hall regime [39, 40, 45], and can condense into the ground state away from $\nu = 1$ [46]. In addition to the theoretical predictions, experimental evidence supports the existence of skyrmion spin textures

---

are parallel and individually occupy the lowest-lying angular momentum states. It corresponds to a filling factor of $\nu = 1$, and is the densest spin-polarized state in the system [44].

in GaAs/AlGaAs quantum wells at $\nu = 1$ [47–50]. Specifically, NMR measurements and spin polarization measurements of GaAs/AlGaAs quantum wells at low temperatures (between 0 and 5 K) have yielded evidence for skyrmionic excitations above the ground state. The emergence of a skyrmion lattice has also been detected in the chiral magnet MnSi using neutron scattering [51]. To date there has been no experimental detection of skyrmions in QDs, however spin pair-correlation calculations of DFT electron wave functions in graphene quantum dots have revealed skyrmion-like magnetic textures [52].

A meron can be described as half a skyrmion since its spin arrangement transitions from a central spin-up or spin-down to an in-plane configuration instead of an antiparallel arrangement at its boundary. Recent literature predicts the formation of merons in confined systems such as QDs in high-magnetic field regimes which can nucleate in the ground state [53–55]. Petković and Milovanović (Ref. [54]) investigated the existence of merons in the lowest-lying states of a few-particle QD (N=4 and N=6). They used ED and the LLL approximation to describe the states of the system. A mapping between the 2D QD system and a one-dimensional spin-chain was used to examine the meron formation in the QD. They found that as the magnetic field was increased from the MDD state, a vortex appeared at the center of the QD. Two-point spin correlations were used to resolve spin-windings in the QD. In each of the four-electron and the six-electron systems, an antiferromagnetic winding was observed along the edge of the QD. Milovanović *et al.* continued their investigation in larger system sizes of 20 and 100 particles (Ref. [55]). The states of these large-particle regimes cannot be efficiently obtained from ED techniques. Instead they used the LLL approximation and derived an expression for the meron wave function confined to a QD from a mean-field ansatz description of a skyrmion in bulk systems. For small systems the meron states were found to be the ground states of the system, however when the particle number exceeded ∼100 this was no longer true.

The above cited works regarding meron formation in quantum dots use either lowest Landau level approximations, Hartree-Fock approximations, or semiclassical interpretations. In this work we use exact diagonalization to obtain the states of the fully interacting QD system. The spin expectation values of these exact states are measured to provide evidence for the formation of merons and other spin textures in the ground state of the QD system.

1.3 Overview

This dissertation is organized in the following manner: Our model for the QD system is presented in Chapter 2. The states under consideration include eigenstates of the QD system which can be characterized by conserved quantities such as spin and orbital angular momentum, henceforth referred to in this document as the "base" eigenstates, as well as topological meron states. Evidence for the existence of four distinct meron states in the lowest energy subspace of a QD is presented in Chapter 3 of this dissertation. Furthermore, we will discuss a method by which these states can be predictably generated and individually distinguished according to their energy. The decay rates of the QD system are calculated in consideration of the electron-phonon interaction. We calculate the relaxation and decoherence rates of the system using density matrix theory. This is detailed in Chapter 4. Relaxation and decoherence rates of a single-electron state are studied in Chapter 5. The effects of including spin-orbit as a perturbation to the system are examined and the decay rates of the induced meron eigenstates are compared to the decay rates of the base QD eigenstates in the absence of spin-orbit. Relaxation and decoherence rates of three-electron states, in both the absence of spin-orbit interaction and the presence of spin-orbit interaction, are studied in Chapter 6. Here we present a novel way to isolate the effect of Coulomb-induced correlations from the effect of the transition energies, which are also affected by Coulomb interaction, on the lifetime of the system. Finally, Chapter 7 concludes with a summary of our findings, their implications in the field, and suggestions for further investigations.

Chapter 2

The Quantum Dot

Our model is based on a lateral QD embedded in a GaAs quantum well. A GaAs quantum well is formed when a layer of GaAs is grown between two layers of a semiconductor material with a larger band gap, such as AlGaAs. The quantum well that forms within the conduction band of the GaAs layer traps conduction band electrons. In this quantum well the electrons are free to move in the lateral (xy) plane, but are confined in the growth direction (z), thus forming a 2DEG. We model this quantum well in the z direction as a finite square well, as discussed in the next section. The electrons are further confined in the lateral plane by applying a negative voltage to the metal gates on the surface of the semiconductor. Following the literature, we model this electrostatic confinement as a two-dimensional harmonic oscillator [56–59]. The details of this model are presented in Sec. 2.2.

2.1 Quantum Well Model

The quantum well in the z direction is approximated as a finite square well, as illustrated in Fig. 2.1. Here ΔE_C is the conduction band offset between the outer semiconductor cladding and the inner GaAs layer. The well width ℓ_z is the width of the GaAs layer in the growth direction, z. We choose ℓ_z=10 nm, which is a typical thickness for a quantum well heterostructure [60] and ΔE_C=243 meV, which is consistent with a GaAs/Al$_{0.3}$Ga$_{0.7}$As quantum well heterostructure [61]. The ground state of the well is a symmetric function with a single node, and is of the form

$$\begin{aligned} \xi(z) &= Ce^{Qz}, && z < -\ell_z/2, \\ \xi(z) &= A\cos(Kz), && -\ell_z/2 \leqslant z \leqslant \ell_z/2, \\ \xi(z) &= Ce^{-Qz}, && z > \ell_z/2, \end{aligned} \tag{2.1}$$

where $A = 0.39$ and $C = 2.97$ are derived from normalization and boundary conditions, and K and Q are related to the bound state energy E and particle mass, in

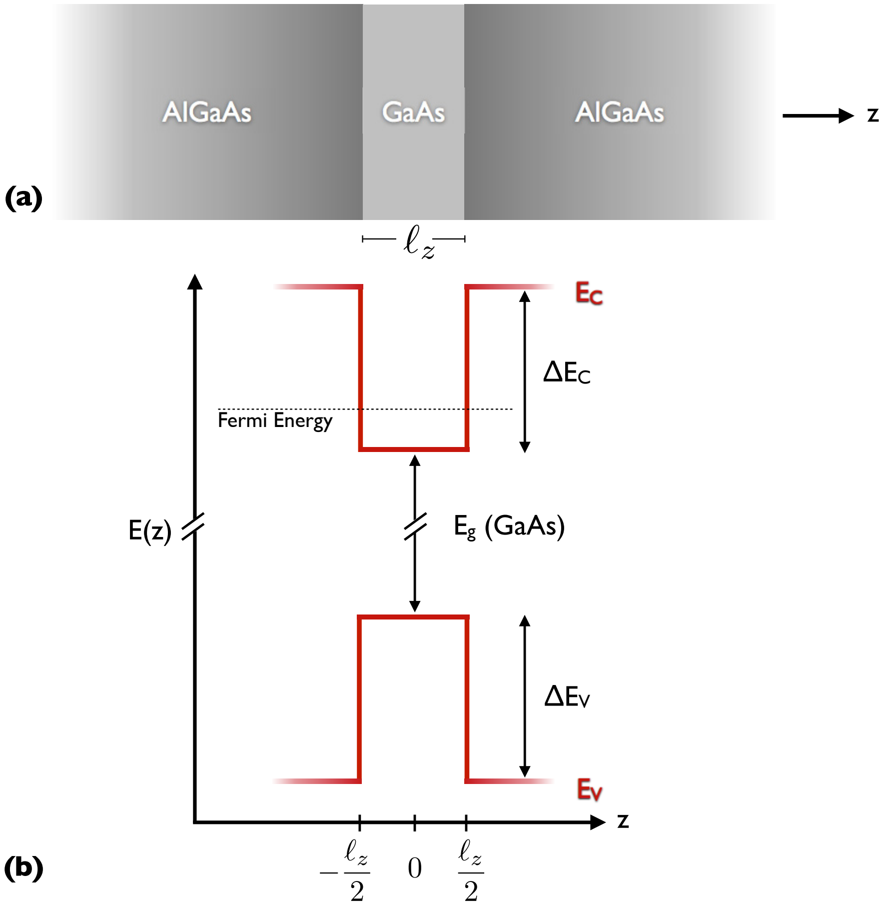

Figure 2.1: (a) Cartoon of an AlGaAs/GaAs/AlGaAs quantum well with growth direction along the z-axis. (b) The band edge diagram of the above quantum well. ℓ_z is the thickness of the quantum well, typically around 20-100 Å [60]. ΔE_C and ΔE_V are the differences in conduction band energies and valence band energies, respectively, of AlGaAs and GaAs at the interface. E_g is the energy of the band gap, typically around 1.43 eV for GaAs at room temperature [62].

this case the effective mass of a conduction band electron in GaAs, m^*. Specifically, $K = \sqrt{2m^*E}/\hbar$ and $Q = \sqrt{2m^*(\Delta E_C - E)}/\hbar$, where $\hbar$ is Planck's constant. The ground state of this quantum well has energy $E = 32.5$ meV from the bottom of the well and is separated from the next excited state by almost 100 meV.

2.2 Quantum Dot Model

The QD system consists of N interacting electrons of charge $-e$, bound to a 2D plane and laterally confined by an electrostatic potential. The 2D Hamiltonian used to describe this system is

$$\hat{H}_{QD} = \sum_{i}^{N} \hat{h}_i + \frac{1}{2} \sum_{i \neq j}^{N} \frac{e^2}{\epsilon |\hat{\boldsymbol{r}}_i - \hat{\boldsymbol{r}}_j|} + \hat{H}_{SO} + \frac{1}{2} g \mu_B B \hat{\sigma}_z, \tag{2.2a}$$

where $\hat{h}$ is the single-particle (SP) Hamiltonian describing harmonic confinement in a perpendicular magnetic field, the second term describes the Coulomb interaction between electrons in the QD (ϵ is the dielectric constant of the semiconductor material), the third term is the spin-orbit interaction, and the fourth term represents the Zeeman effect. The spin-orbit interaction is applied perturbatively to our model, and is described in further detail in Sec. 3.5. In the Zeeman term, g is the characteristic g-factor for the semiconductor material, μ_B is the Bohr magneton, B is an external magnetic field pointing along the growth direction (z), and $\hat{\sigma_z}$ is the z component of the Pauli spin matrix. Finally, the SP harmonic confinement is described as follows:

$$\hat{h} = \frac{1}{2m^*} \widehat{\boldsymbol{P}}^2 + \frac{1}{2} m^* \omega_0^2 \hat{r}^2. \tag{2.2b}$$

Here $\widehat{\boldsymbol{P}} = \hat{\boldsymbol{p}} + \frac{e}{c} \boldsymbol{A}(\hat{\boldsymbol{r}})$ is the canonical momentum, $\hat{\boldsymbol{r}} = (\hat{x}, \hat{y})$ the position operator, and ω_0 the parabolic confinement frequency. $\boldsymbol{A}(\hat{\boldsymbol{r}})$ is taken to be in the symmetric gauge, $\boldsymbol{A}(\hat{\boldsymbol{r}}) = \frac{B}{2}(-\hat{y}, \hat{x}, 0)$.

In all that follows, the material parameters in Eq. (2.2) are fixed as follows: $m^* = 0.067 m_e$ (m_e is the mass of an electron), $\epsilon = 12.4$, and $g = -0.44$. These parameters are standard values for GaAs [63–65]. Due to the relatively small g-factor for GaAs, the Zeeman spin-splitting is very small in the cases investigated in this dissertation, on the order of 0.1 meV in the single-electron system, and on the order of 0.01 meV when Coulomb interaction is considered in the three-electron system. We do include the Zeeman energy in all of our calculations, but in the interacting system use it as a measure of precision in the state energies. The degree of Zeeman splitting in the lowest-lying states of the three-electron system for a fixed confinement potential of $\hbar\omega_0 = 1$ meV can be seen in Fig. 2.2.

The eigenstates of the SP Hamiltonian, Eq. (2.2b), are characterized by two harmonic-oscillator quantum numbers, $n, m = 0, 1, 2, \ldots$ [21]. These eigenstates, also known as "Fock-Darwin" states after Refs. [66, 67], are the "atomic orbitals" of the QD, and are given by

$$|nm\rangle = \frac{1}{\sqrt{n!m!}} (a^\dagger)^n (b^\dagger)^m |00\rangle, \tag{2.3}$$

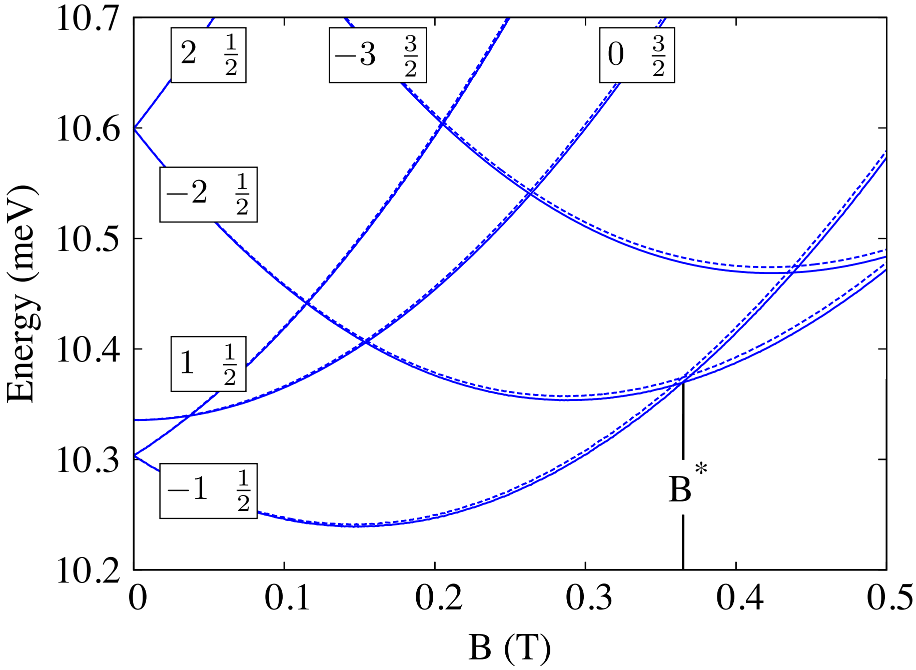

Figure 2.2: Zeeman splitting in the lowest lying states of the fully-interacting three-electron QD system (Eq. (2.2a)) with $\hbar\omega_0 = 1$ meV. L_z and S quantum numbers are displayed for each state. Spin-up states are shown with solid lines and spin-down states are shown with dashed lines. At B* the four $|L_z,\, S_z\rangle$ states $\left|-1, \pm\frac{1}{2}\right\rangle$, $\left|-2, \pm\frac{1}{2}\right\rangle$ are degenerate to within less than 0.005 meV. In general we consider the states to be spin-degenerate.

where, $a^\dagger$ and $b^\dagger$ are the usual Bose creation operators (see Eq. (B.3)), and $|00\rangle$ is the SP ground state. These orbitals have energy ε_{nm} given by

$$\varepsilon_{nm} = \hbar\Omega_+(n + \tfrac{1}{2}) + \hbar\Omega_-(m + \tfrac{1}{2}), \tag{2.4}$$

where $\Omega_\pm = (\sqrt{4\omega_0^2 + \omega_c^2} \pm \omega_c)/2$, and $\omega_c = eB/(m^*c)$ is the cyclotron frequency. This energy reduces to $\hbar\omega_0(n + m + 1)$ in the absence of a magnetic field.

The SP Hamiltonian, the z-component of the orbital angular momentum, $\hat{L}_z$, and a component of the spin operator—which is taken to be the z-component $\hat{S}_z$—form a set of commuting observables which is used to classify the QD states: $\hat{L}_z|nms\rangle = \hbar(n - m)|nms\rangle$, $\hat{S}_z|nms\rangle = \hbar s|nms\rangle$, $\hat{h}|nms\rangle = \varepsilon_{nm}|nms\rangle$.

In our calculations we require the position-space representation of the orbitals.

These are given by [68]

$$\phi_{nm}(r,\theta) = (-1)^{n_r} \frac{1}{\sqrt{2\pi} l_0} \sqrt{\frac{n_r!}{(n_r + |m'|)!}} \times e^{im'\theta} e^{-r^2/(4l_0^2)} \left(\frac{r}{\sqrt{2} l_0}\right)^{|m'|} L_{n_r}^{|m'|} \left(\frac{r^2}{2l_0^2}\right), \quad (2.5)$$

where r and θ are the polar coordinates in the lateral plane, $l_0 = \sqrt{\hbar/(2m^*\omega)}$ is the effective length with $\omega = \sqrt{4\omega_0^2 + \omega_c^2}/2$, $n' = n + m$, $m' = n - m$, $n_r = (n' - |m'|)/2$, and $L_n^{(\alpha)}(x)$ is the generalized Laguerre polynomial. [69]

Neglecting for now the spin-orbit interaction, the eigenstates of the interacting system are determined by exact diagonalization of Eq. (2.2a). This procedure begins by determining many-particle basis states (Slater determinants), eigenstates of Eq. (2.2b), that are composed of antisymmetrized products of the SP states in Eq. (2.3). As many as 288 SP states, and as many as 25,000 many-particle basis states are used in the diagonalization routine[1]. Block-diagonalization is performed for a given set of parameters. These include system parameters (B, ω_0, m^*, ϵ) and the conserved quantities N, L_z, S_z, S^2. The Coulomb matrix elements are evaluated using the convenient closed-form expression derived in Ref. [24]. These eigenstates, which are characterized by the aforementioned commuting observables, are referred to in this document as the "base" eigenstates. This is to differentiate them from the meron states. The meron states are superpositions of these "base" eigenstates, however they cannot be characterized by $\hat{L}_z$ and $\hat{S}_z$ quantum numbers. The meron states are discussed in detail in Chap. 3.

Once the eigenstates are determined, position-dependent spin expectation values are calculated to reveal meron textures in the QD (see Chap. 3). In addition, decay times for these states are calculated for the single-electron system in Chap. 5 and for the three-electron system in Chap. 6.

---

[1] In the fully interacting three-particle system, state and energy convergence is achieved with approximately 500 many-particle basis states.

Chapter 3

Merons

In this chapter we discuss the conditions under which merons, topological spin structures, form in the QD system. We begin with an introduction to the spin-density operator, used to calculate the spin-textures in the meron states. Next is the analytic development of chirality, a topological characteristic that partially defines the meron state. Merons are characterized by a winding spin vector field which smoothly transforms into a central spin that is perpendicular to the plane in which the spin winds. This is followed by an example demonstrating how merons form in a three-particle QD at low magnetic field. Spin-orbit interaction, a common QD perturbation which can induce the formation of some of these meron states, is also discussed. The chapter concludes with an analysis on predicting when merons form in the QD ground state.[1]

3.1 Spin Expectation Values

In order to reveal the spin texture in a meron state, the spin-expectation value must be calculated in position-space for each spatial direction, x, y, and z. In general, the spin-density operator is expressed as

$$\hat{\boldsymbol{S}}(\boldsymbol{r}) = \frac{\hbar}{2} \sum_{\sigma,\sigma'} \hat{\Psi}^{\dagger}_{\sigma}(\boldsymbol{r}) \hat{\boldsymbol{\sigma}}_{\sigma\sigma'} \hat{\Psi}_{\sigma'}(\boldsymbol{r}), \tag{3.1}$$

where $\hat{\Psi}^{\dagger}_{\sigma}(\boldsymbol{r})$ ($\hat{\Psi}_{\sigma}(\boldsymbol{r})$) is the field operator creating (annihilating) a fermion with spin $\pm\hbar/2$ at position $\boldsymbol{r}$, and $\hat{\boldsymbol{\sigma}}$ is the vector of Pauli matrices. The field operators are specifically given by

$$\hat{\Psi}^{\dagger}_{\sigma}(\mathbf{r}) = \sum_{n\,m} \phi^{*}_{nm}(\mathbf{r})\, \hat{c}^{\dagger}_{nm\sigma}, \tag{3.2a}$$

$$\hat{\Psi}_{\sigma}(\mathbf{r}) = \sum_{n\,m} \phi_{nm}(\mathbf{r})\, \hat{c}_{nm\sigma}, \tag{3.2b}$$

---

[1] The results presented in this chapter have been published in Ref. [70].

where $\phi_{nm}(\mathbf{r})$ is the 2D position-space representation of the SP $[n\,m]$ orbital in the QD (see Eq. (2.5)), and $\hat{c}^{\dagger}_{nm\sigma}$ ($\hat{c}_{nm\sigma}$) is a second quantization Fermi operator which creates (annihilates) an electron of spin σ (as projected onto the z-axis) in the $[n\,m]$ orbital.

The individual components of $\hat{\boldsymbol{S}}(\boldsymbol{r})$ can be expressed in canonical form in the S_z basis as:

$$\hat{S}_x(\boldsymbol{r}) = \frac{\hbar}{2}\sum_{i\,j\,\sigma} \phi_i^*(\boldsymbol{r})\phi_j(\boldsymbol{r})\hat{c}^{\dagger}_{i\sigma}\hat{c}_{j\bar{\sigma}}, \tag{3.3a}$$

$$\hat{S}_y(\boldsymbol{r}) = \frac{i\hbar}{2}\sum_{i\,j\,\sigma} \sigma\phi_i^*(\boldsymbol{r})\phi_j(\boldsymbol{r})\hat{c}^{\dagger}_{i\sigma}\hat{c}_{j\bar{\sigma}}, \tag{3.3b}$$

$$\hat{S}_z(\boldsymbol{r}) = \frac{\hbar}{2}\sum_{i\,j\,\sigma} \sigma\phi_i^*(\boldsymbol{r})\phi_j(\boldsymbol{r})\hat{c}^{\dagger}_{i\sigma}\hat{c}_{j\sigma}, \tag{3.3c}$$

where $\sigma = \pm 1$ and $\bar{\sigma}$ has the opposite spin of σ. The composite indexes i and j each represent a set of orbital quantum numbers n and m.

3.2 Chirality

The chirality $C_n(\mathcal{C})$ of a vector field $\boldsymbol{v}(s)$, over a closed curve $\mathcal{C}$ in the direction of the unit vector $\boldsymbol{n}$ can be defined as

$$C_n(\mathcal{C}) = \oint_{\mathcal{C}} ds\, \frac{\boldsymbol{n}\cdot(\boldsymbol{v}(s)\times\partial_s\boldsymbol{v}(s))}{|\boldsymbol{v}_{\perp}(s)|^2}, \tag{3.4}$$

where $\boldsymbol{v}_{\perp}(s) \equiv \boldsymbol{n}\times\boldsymbol{v}(s)$ is a vector perpendicular to the direction $\boldsymbol{n}$ and serves as a normalization factor; it is the global chiral character of the vector field which is of primary interest.

The system is a two-dimensional, rotationally-symmetric QD centred at the origin, with the curve $\mathcal{C}$ a circle about the origin with radius r. Furthermore, the direction of $\boldsymbol{n}$ is taken to be perpendicular to the plane of the QD. The vector field in question is the spin density $\boldsymbol{S}(\boldsymbol{r}) \equiv \langle\hat{\boldsymbol{S}}(r,\theta)\rangle$. Taking the QD to lie in the x-y plane, Eq. (3.4) takes the form

$$C_z(r) = \frac{1}{2\pi}\int_0^{2\pi} d\theta\, \frac{\boldsymbol{z}\cdot(\boldsymbol{S}(r,\theta)\times\partial_\theta\boldsymbol{S}(r,\theta))}{|\boldsymbol{S}_{\perp}(r,\theta)|^2}, \tag{3.5}$$

where $\boldsymbol{S}_{\perp}(r,\theta) = \boldsymbol{z}\times\boldsymbol{S}(r,\theta)$.

In general we are concerned with a correlated many-body fermionic system. The spin-density operator is defined in Eq. (3.1), and with this the chirality takes the form of a chiral spin current

$$C_z(r) = \frac{1}{2\pi}\int_0^{2\pi} d\theta\, j_{\text{spin}}(r,\theta), \tag{3.6a}$$

with the chiral spin current density given by

$$j_{\text{spin}}(r,\theta) = \frac{i}{2\left|S_+\right|^2}\left(S_+\partial_\theta S_+^* - S_+^*\partial_\theta S_+\right), \tag{3.6b}$$

where $S_+ = \langle\hat{\psi}_\uparrow^\dagger(\boldsymbol{r})\,\hat{\psi}_\downarrow(\boldsymbol{r})\rangle$. (A full derivation this result can be found in Appendix A.1.) Windings occur for states composed of different angular momenta and spin. This is further discussed in the proceeding section.

C_z, which shall be shorten to C from now on, is an integer winding number whose magnitude indicates the number of full 2π rotations along a closed curve $\mathcal{C}$ about the QD origin, and whose sign indicates the sense of rotation. The meron states discussed in this dissertation are characterized by their winding number. In the next section we discuss the conditions under which meron states can occur. In Sec. 3.4 we demonstrate how these meron states can occur in parabolic QDs containing three strongly-interacting electrons. In Sec. 3.5 it is further shown that some of these winding states are eigenstates of the QD system when perturbed by the spin-orbit interaction, whose degeneracy may be split into four spectroscopically distinct meron states $|QC\rangle$, where Q represents the topological charge of the meron. The topological charge can be defined using the Pontryagian index [40]. We define it in terms of the orientation of the (x-y) planar component of the spin density field. That is to say, states which have the same chirality but different topological charge differ from each other by a complete spin flip of the entire in-plane component of the spin density field in real space.

3.3 Predicting Merons

Windings occur only for specific combinations of "base" QD eigenstates, that is states that are a superposition of eigenstates with certain L_z and S_z quantum numbers. Consider a state of the form $|\psi\rangle = (|L_z\, S_z\rangle + \gamma|L_z'\, S_z'\rangle)/\sqrt{2}$, where $|L_z\, S_z\rangle$ and $|L_z'\, S_z'\rangle$ are either SP eigenstates of the QD or fully interacting N-particle eigenstates. For these particular states $|\psi\rangle$, Eq. (3.6) yields

$$C = (L'_z - L_z)(S_z - S'_z)\delta_{|S_z - S'_z|,\,1}, \tag{3.7}$$

where δ_{ij} is the Kronecker delta. (Please refer to Appendix A.2 for details.) Equation (3.7) predicts that superpositions of states of *different* orbital and spin angular momentum contain winding spin textures. This superposition can be induced by spin-orbit interaction (see Sec. 3.5). Furthermore, the magnitude of the winding number associated with the winding state is equal to the difference between the orbital angular momentum of the degenerate states. For example, if we had four orthogonal QD eigenstates, the state $|\psi\rangle$ above can be generalized to

$$\begin{aligned} |QC\rangle = \frac{1-c}{2\sqrt{2}}(|L_z, S_z\rangle + \gamma q\,|L'_z, S'_z\rangle) \\ + \frac{1+c}{2\sqrt{2}}(|L_z, S'_z\rangle + \gamma' q\,|L'_z, S_z\rangle), \end{aligned} \tag{3.8}$$

where $L_z \neq L'_z$, $|S_z - S'_z| = 1$, $c \equiv C/|C|$, $q \equiv Q/|Q|$, and $\gamma^{(\prime)}$ is a general coefficient. According to Eq. (3.7), states of this form are winding states (see Appendix A.3 for details).

The condition stated in Eq. (3.7) is *necessary* but not sufficient to predict merons specifically. It will predict winding states in general. Merons are winding states, but they are further distinguished by their central spin-up or spin-down. In the QD system, this can arise from mixing states with L_z quantum numbers that are different in *magnitude*: States of differing orbital angular momentum have different amounts of particle density accumulated throughout the QD in position space, including about the origin. Note that points of four-fold degeneracy in the three-electron and five-electron QD spectra contain only $|L_z,\, S,\, S_z\rangle$ states with $S = 1/2$. By the condition $|S_z - S'_z| = 1$ outlined in Eq. (3.7), the winding states at these four-fold degeneracy points will contain states with opposite S_z quantum numbers (namely $S_z = \pm 1/2$). Therefore, the winding states in Eq. (3.8) with L_z quantum numbers exactly equal in magnitude will have exactly zero S_z density at the origin and throughout the QD, while winding states with L_z quantum numbers that differ in magnitude will have some finite S_z density at the origin. The $|L_z,\, S,\, S_z\rangle$ states with L_z quantum numbers equal in magnitude are degenerate only at zero magnetic field; as the magnetic field is increased, degenerate points in the ground state form between states with L_z values that are different in magnitude.

To summarize, for merons to be present around four-fold degenerate points in the QD spectra, the condition stated in Eq. (3.7) must be satisfied. Furthermore, the degenerate states must have L_z values that are different in magnitude, which occurs for magnetic field strengths above zero.

3.4 Merons in a QD

The simplest interacting system exhibiting meron textures occurs for $N = 3$ confined electrons. The low-lying spectra as a function of magnetic field are shown in Fig. 2.2 for $\hbar\omega_0 = 1$ meV. For the system parameters given in Chapt. 2, a ground state degeneracy exists at a field of $B^* = 0.365$ T. This degenerate manifold is spanned by the four spin-1/2 states $|L_z, S_z\rangle = |{-1}, \pm 1/2\rangle\,, |{-2}, \pm 1/2\rangle$.

This degenerate subspace at B^* contains merons. An explicit form of Eq. (3.8) in this subspace is

$$\begin{aligned} |QC\rangle = \frac{1-C}{2\sqrt{2}}\big(\left|-1, \tfrac{1}{2}\right\rangle - iQ\left|-2, -\tfrac{1}{2}\right\rangle\big) \\ + \frac{1+C}{2\sqrt{2}}\big(\left|-1, -\tfrac{1}{2}\right\rangle + Q\left|-2, \tfrac{1}{2}\right\rangle\big). \end{aligned} \tag{3.9}$$

These four states have a chirality $C = \pm 1$ and a topological charge $Q = \pm 1$ and are orthogonal. They display the spin textures $\langle \hat{\boldsymbol{S}}(\boldsymbol{r}) \rangle$ shown in Fig. 3.1. These windings can come about even in the case of single electron states as long as the spin and angular moment numbers are different (see Eq. (3.7)). They are independent of the Coulomb interaction between the electrons. Previous work [53–55] has focused on lowest-Landau-level physics or on semiclassical approximations. The present numerically exact results show that merons can exist far beyond the semiclassical regime; right down to the extreme quantum limit of very few confined particles where correlations are strongest. In particular, the three-particle ground states shown in Fig. 3.1 are *not* spin-polarized states, nor do they correspond to the $\nu = 1$ maximum density droplet. The states in Fig. 3.1 correspond to a filling factor of $2 > \nu > 1$. (The angular momentum of the N-particle maximum density droplet is $L_z = -N(N-1)/2$ [71].)

In order to produce these meron states, we consider next the perturbing effect of spin-orbit in the QD system.

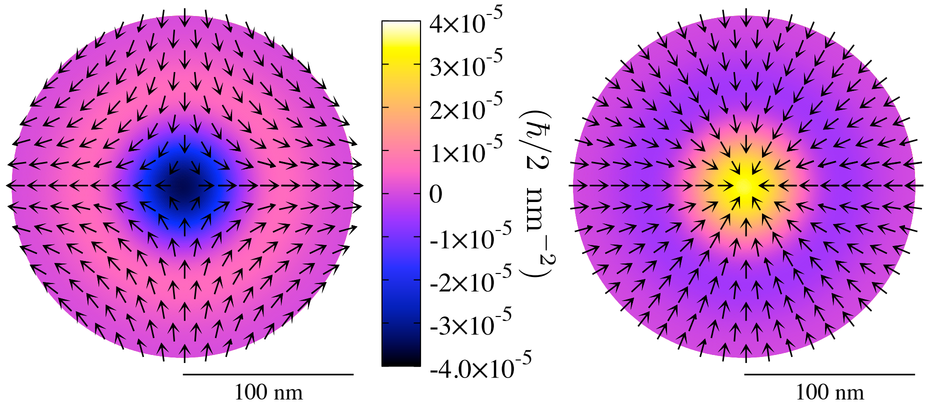

Figure 3.1: Two of the four meron textures for the three-particle states given in Eq. (3.9). $\langle S_x(\boldsymbol{r})\rangle$ and $\langle S_y(\boldsymbol{r})\rangle$ are represented by the vector field, while $\langle S_z(\boldsymbol{r})\rangle$ is represented by the colour bar. The remaining two configurations are obtained from these by a local in-plane spin rotation of π. The textures shown were obtained at the four-fold degeneracy point $B = B^*$ (see Fig. 2.2).

3.5 Spin-Orbit Interaction

Spin-orbit (SO) interaction occurs when a charged particle with an intrinsic spin magnetic moment $\boldsymbol{\mu}$ moves through an electric field, $\mathbf{E}$ [72]. This effect occurs in atoms. For example, consider a hydrogen-like atom with a single valence electron and an atomic core of inner-shell electrons and a charged nucleus. The atomic core has a central electrostatic potential of $V(r)$ and therefore emits an electric field $\mathbf{E} = -\boldsymbol{\nabla} V(r)$ as felt by the valence electron. In the rest frame of the electron, the orbit of the atomic core produces an effective magnetic field,

$$\mathbf{B}_{\text{eff}} = -\left(\frac{\mathbf{v}}{c}\right) \times \mathbf{E}, \tag{3.10}$$

where $\mathbf{v}$ is the velocity of the orbiting atomic core. This effective magnetic field couples with the magnetic moment of the electron, $\boldsymbol{\mu} = e\mathbf{S}/(m_e c)$, i.e. the spin $\mathbf{S}$ of the electron, to produce the SO interaction,

$$\hat{H}_{\text{SO}} = \frac{1}{2m_e^2c^2}\frac{1}{r}\frac{dV}{dr}\hat{\mathbf{L}} \cdot \hat{\mathbf{S}}. \tag{3.11}$$

Because this interaction involves magnetic fields and moving charges, the SO interaction is in fact a relativistic effect. The full quantum-mechanical derivation of Eq. (3.11) can be found in Ref. [73]. The energy of this interaction perturbatively changes the kinetic energy of the electron.

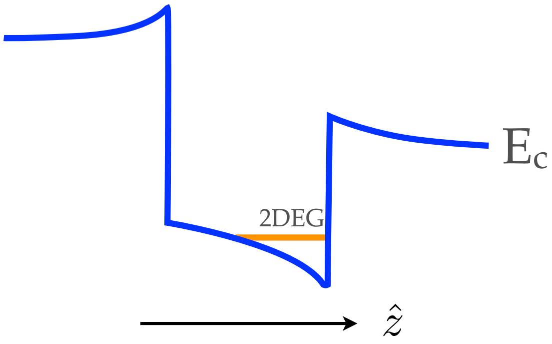

Figure 3.2: The confinement potential of the quantum well may be asymmetric.

The SO interaction is also a common perturbation in semiconductor heterostructures [74–79]. Two types of SO interaction are commonly investigated in these 2DEG systems: The Rashba SO interaction which arises from the structural inversion asymmetry of the heterostructure, and the Dresselhaus SO interaction which arises from the bulk inversion asymmetry of the semiconductor medium.

We model the potential of the 2DEG quantum well as a finite square well, but the shape of the potential well can in fact be skewed (see Fig. 3.2). This asymmetry can be affected by the doping concentrations of the semiconductors forming the heterostructure [60, 80, 81], or by an applied electric field, e.g. by changing the gate voltages on the surface electrodes of a semiconductor heterostructure [82–85], thus making the strength of the Rashba SO interaction tunable. The gradient of the confinement potential in the quantum well creates an electric field $\mathbf{E}$ along the growth direction, z. Writing $\hat{\mathbf{L}} = \hat{\mathbf{r}} \times \hat{\mathbf{P}}$, and taking $\mathbf{E} = \mathrm{E}\hat{\mathbf{z}}$, we can write the Rashba SO Hamiltonian in a form analogous to the atomic SO equation in Eq. (3.11):

$$\hat{H}_{\mathrm{R}} = \frac{\alpha_R}{\hbar}\left(\hat{\sigma}_x \hat{\mathrm{P}}_y - \hat{\sigma}_y \hat{\mathrm{P}}_x\right), \tag{3.12}$$

where $\hat{\sigma}_x$ and $\hat{\sigma}_y$ are the x and y components of the Pauli spin matrix and α_R is the Rashba SO coupling constant. The Rashba SO constant is material-dependent and proportional to the applied electric field.

Bulk zinc blende semiconductors such as GaAs lack inversion symmetry, giving rise to the Dresselhaus SO effect [86]. Specifically, in bulk GaAs there is a polar bond between the gallium and the arsenic atoms which creates an electric field [87]. This intrinsic electric field results in the Dresselhaus SO interaction. In a two-dimensional system, the Dresselhaus SO Hamiltonian reduces to a term that is linear in the electron momentum and a term that is cubic in the electron momentum:

$$\hat{H}_{\mathrm{D}} = -\frac{\beta_D}{\hbar}\left(\hat{\sigma}_x\hat{\mathrm{P}}_x - \hat{\sigma}_y\hat{\mathrm{P}}_y\right) + \frac{\gamma}{\hbar}\left(\hat{\sigma}_x\hat{\mathrm{P}}_x\hat{\mathrm{P}}_y^2 - \hat{\sigma}_y\hat{\mathrm{P}}_y\hat{\mathrm{P}}_x^2\right), \tag{3.13}$$

where γ is the bulk Dresselhaus coefficient which characterizes the strength of the polar bond, $\beta_D = \gamma\langle \mathrm{P}_z^2\rangle$, and $\langle \mathrm{P}_z^2\rangle$ is the expectation value of $\hat{\mathrm{P}}_z^2$ with respect to the ground state wave function of the quantum well in the growth direction, z [79,88,89]. In this dissertation we do not consider the cubic term since for a narrow quantum well (i.e. strong electron confinement) its contribution can be neglected with respect to the linear Dresselhaus term [89,90]. We therefore consider the total SO interaction to be the sum of the Rashba SO Hamiltonian in Eq. (3.12) and the linear part of the Dresselhaus SO Hamiltonian in Eq. (3.13) [58,86,91–95]:

$$\hat{H}_{SO} = \frac{\alpha_R}{\hbar}\left(\hat{\sigma}_x\hat{\mathrm{P}}_y - \hat{\sigma}_y\hat{\mathrm{P}}_x\right) - \frac{\beta_D}{\hbar}\left(\hat{\sigma}_x\hat{\mathrm{P}}_x - \hat{\sigma}_y\hat{\mathrm{P}}_y\right). \tag{3.14}$$

We treat the SO interaction perturbatively and diagonalize the total SO Hamiltonian in Eq. (3.14) in the degenerate subspace of the four lowest-lying $|L_z, S_z\rangle$ QD states, henceforth referred to as the ground state subspace. The form of the four $|QC\rangle$ states in Eq. (3.9) are special because they are eigenstates of the SO-perturbed QD system at B^*. It may also be that, to linear order, the Dresselhaus and Rashba SO interactions can split their degeneracy at B^*. In general, the linear SO interaction can only mix QD states which contain orbital angular momentum states with L_z values that differ by 1 only, and spin angular momentum states with S_z values that differ by 1 only (refer to App. B.1 for details). We restrict ourselves to subspaces which contain only spin-half states, that is states with $S_z = \pm 1/2$. This is because the ground state manifolds in both the one-electron and three-electron system are comprised of spin-half states for the parameter values investigated in this dissertation. Meron states in these spin-half subspaces can be generalized as

$$\begin{aligned} |QC\rangle = \frac{1-C}{2\sqrt{2}}&\left(\left|L_z, \tfrac{1}{2}\right\rangle - iQ\left|L_z-1, -\tfrac{1}{2}\right\rangle\right) \\ &+ \frac{1+C}{2\sqrt{2}}\left(\left|L_z, -\tfrac{1}{2}\right\rangle + Q\left|L_z-1, \tfrac{1}{2}\right\rangle\right), \end{aligned} \tag{3.15}$$

where the chirality of the meron state is $C = \pm 1$ and the topological charge is $Q = \pm 1$.

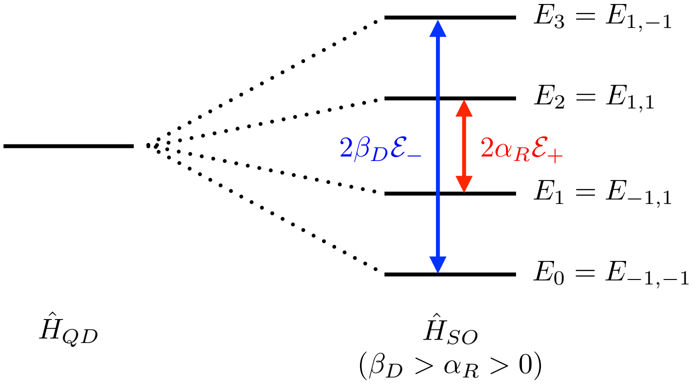

Figure 3.3: Spin-orbit interaction is expected to lift the four-fold degeneracy of the states $\left|L_z - 1, \pm\frac{1}{2}\right\rangle$, $\left|L_z, \pm\frac{1}{2}\right\rangle$ in the ground state manifold.

Within the ground state subspace, the SO-induced energy splittings E_{QC} associated with each of the above $|QC\rangle$ state are determined to be

$$\mathrm{E}_{QC} = \frac{Q}{2}\big(\alpha_R\mathcal{E}_+(1+C) + \beta_D\mathcal{E}_-(1-C)\big), \tag{3.16}$$

where

$$\mathcal{E}_\pm \equiv \lambda \left\langle L_z - 1, \pm\tfrac{1}{2}\right| \hat{\sigma}_\pm\big(\hat{a}\left(1+\tfrac{1}{\nu}\right) - \hat{b}^\dagger\left(1-\tfrac{1}{\nu}\right)\big)\left|L_z, \mp\tfrac{1}{2}\right\rangle, \tag{3.17}$$

with $\lambda = 1/(2\sqrt{2}\ell_0)$ and $\nu = \sqrt{1+4\omega_0^2/\omega_c^2}$. (Please refer to App. B.1 for details.) Figure 3.3 illustrates this energy splitting. In Eq. (3.17), $\hat{a}$ and $\hat{b}^\dagger$ independently lower the orbital angular momentum of the $|L_z, S_z\rangle$ states, while $\hat{\sigma}_\pm$ raises or lowers the spin. Note that if either α_R or β_D are zero, or if $\alpha_R = \beta_D$, the energy splitting of the states is two-fold degenerate. If $\alpha_R \neq \beta_D$, and if neither α_R nor β_D are zero, the energy is split into four distinct levels. We find that the Rashba term couples only to merons with positive chirality, whereas the Dresselhaus term couples only to merons with negative chirality. Since the Rashba term is to some extent tunable through externally-applied gate voltages, Eq. (3.16) demonstrates a measure of experimental control over the merons.

3.6 Finding Merons

The existence criteria for merons is expected to occur throughout the phase space of the QD. We do not investigate two-electron systems because their degenerate ground state manifolds involve more than four QD states which is beyond the scope of the winding state model developed in this dissertation. Some of the degenerate ground state manifolds in four-electron systems are four-fold degenerate, however the degenerate QD states do not fit the mould of the four generalized winding states in Eq. (3.8). We therefore restrict our exploration to three-electron systems and five-electron systems.

$\mathbf{N = 3}$

The next four-fold degeneracy point in the $N = 3$ ($\hbar\omega_0 = 1$ meV) ground state spectrum occurs at a magnetic field of $B^* = 1.07$ T between the $|L_z,\ S,\ S_z\rangle$ eigenstates of $|-4,\ 1/2,\ \pm 1/2\rangle$ and $|-5,\ 1/2,\ \pm 1/2\rangle$, as indicated in Fig. 3.4. (There is a level-crossing in the ground state at a lower magnetic of B=0.94 T, however it is six-fold degenerate and involves states with spin 3/2. The meron model developed in this thesis is restricted to four spin-half states and so meron formation is not explored at this point.) Based on the arguments made in Sec. 3.3, winding states should occur around the degeneracy point of these particular states. Furthermore, because the degenerate states have L_z quantum numbers that are different in magnitude, these winding states should be meron states. In the form of Eq. (3.8) the four states can be written as

$$\begin{aligned} |QC\rangle = \frac{1-c}{2\sqrt{2}}\big(|{-4},1/2\rangle - iq\,|{-5},-1/2\rangle\big) \\ + \frac{1+c}{2\sqrt{2}}\big(|{-4},-1/2\rangle + q\,|{-5},1/2\rangle\big). \end{aligned} \tag{3.18}$$

Note that at B^* these states are eigenstates of the SO-perturbed system. The spin expectation values for each spin component $\langle S_x(r)\rangle$, $\langle S_y(r)\rangle$, and $\langle S_z(r)\rangle$ are plotted in Fig. 3.5 for two of these states. Indeed these states have windings, and the central spin that is polarized perpendicular to the plane of winding indicates that these spin textures are merons. Furthermore, they have a winding number of one, commensurate with the prediction in Eq. (3.7).

$\mathbf{N = 5}$

We next look to the five-electron system. Figure 3.6 shows the ground state and some of the lowest-lying states for five interacting electrons as a function of magnetic

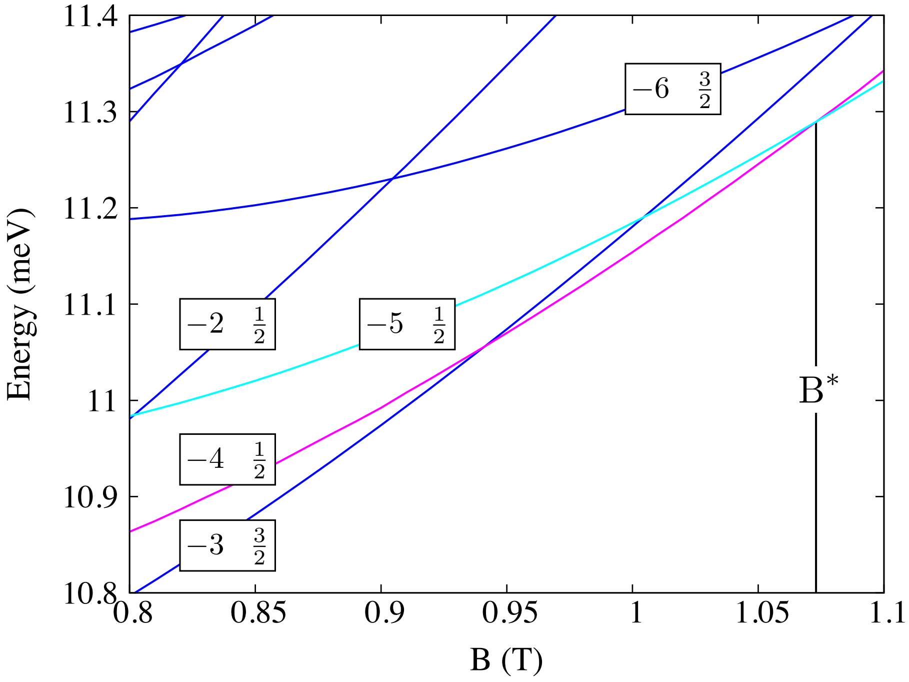

Figure 3.4: A second four-fold degeneracy point in the spectra for $N = 3$ interacting particles ($\hbar\omega_0 = 1$ meV). The quantum numbers L_z and S of selected levels are shown. The field B^* at which this degeneracy occurs is marked.

field. The four-fold degeneracy at $B^* = 0.16$ T occurs between the states $|L_z, S_z\rangle = |-1,\, 1/2,\, \pm 1/2\rangle$ and $|-4,\, 1/2,\, \pm 1/2\rangle$.

Based on the existence criteria discussed in Sec 3.3, four orthogonal meron states are expected to exist around this degeneracy point. From Eq. (3.8), these four $N = 5$ meron states are

$$|QC\rangle = \frac{1-c}{2\sqrt{2}} \left(|-1, 1/2\rangle - iq\,|-4, -1/2\rangle\right) + \frac{1+c}{2\sqrt{2}} \left(|-1, -1/2\rangle + q\,|-4, 1/2\rangle\right). \quad (3.19)$$

Since the difference in L_z quantum numbers between the degenerate states is ±3, the merons which exist here are expected to have a winding of three. The expectation value of the individual spin components are plotted in Fig. 3.7 for two of these four meron states. Indeed it is clear from the plots of the spin expectation values in Fig. 3.7 that these states have a winding number of 3. Figure 3.8 shows the $\langle S_z(r)\rangle$ dependence on radius for the merons with $C = -3$. The large, off-centre peak in the

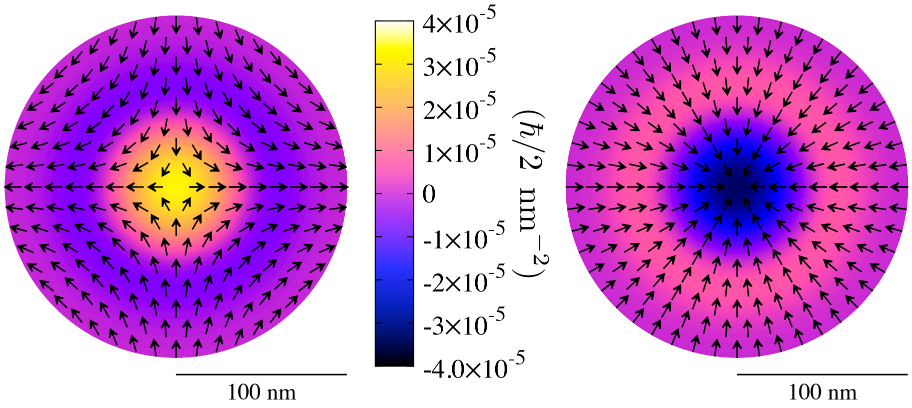

Figure 3.5: More meron spin textures in the three-particle system at the degeneracy point $B^* = 1.07$ T (Fig. 3.4). The state on the left has $Q, C = 1, -1$ while the state on the right has $Q, C = -1, 1$. The remaining two configurations are obtained from these by a local in-plane spin rotation of π.

$\langle S_z(r) \rangle$ distribution is due to the increased Coulomb interaction strength relative to the three-particle system.

Unlike the two examples discusses in the three-electron case, these meron states are *not* eigenstates of the SO-perturbed system since they contain orbital angular momentum states with L_z values that differ by more than 1.

We have shown above cases where merons exist in the four-fold degenerate manifold of states with different L_z and S_z quantum numbers. These merons form in accordance with the predictions made in Sec. 3.3. If the meron states are composed of "base" QD eigenstates which differ in their L_z and S_z values by 1, their existence will be induced in the system by the perturbing effects of the SO interaction. Furthermore, it may be possible that the SO interaction will lift their degeneracy. To determine if these meron states are long-lived, their relaxation and decoherence times must be determined. In the next chapter we develop the theory used to calculate these decay times. In Chapters 5 and 6 we calculate the decay rates of single- and three-electron states, with and without spin-orbit interaction, in the presence of a phonon bath.

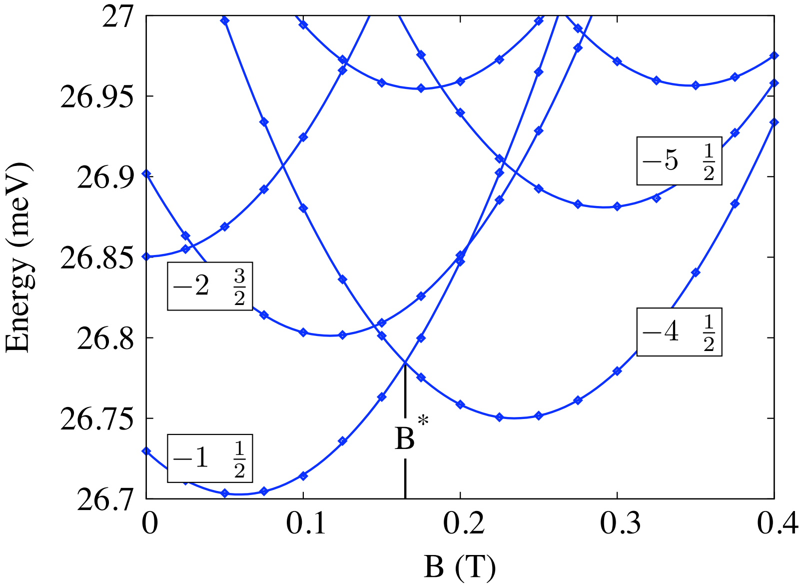

Figure 3.6: Low-lying spectra for $N = 5$ interacting particles with 2D harmonic confinement, Eq. (2.2). The quantum numbers L_z and S of selected levels are shown. B^* marks the field around which merons form in the ground state.

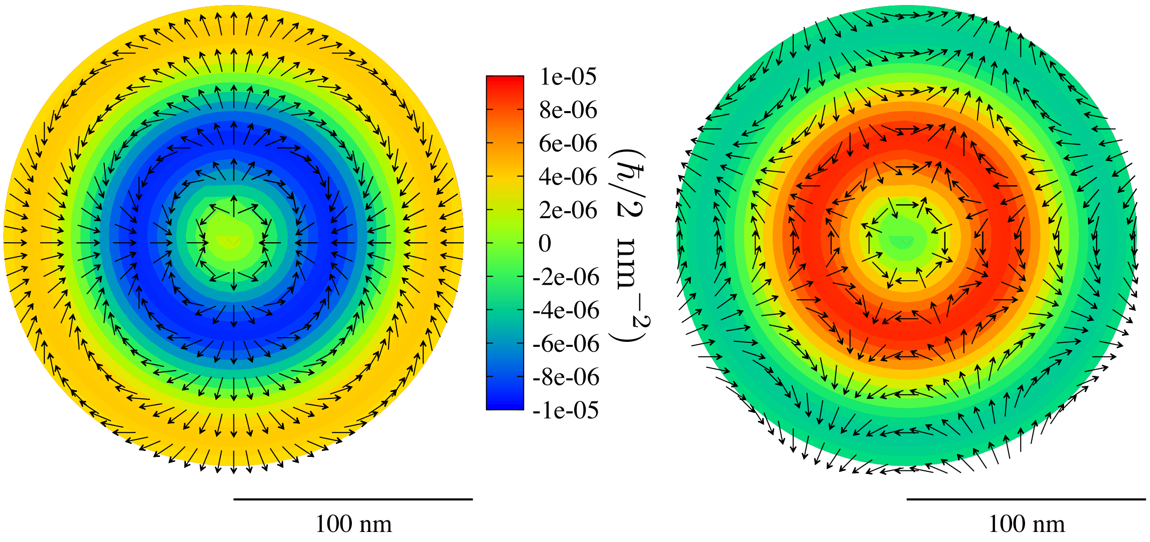

Figure 3.7: Meron textures in the five-particle system at the degeneracy point B^* (Fig. 3.6). For the state on the left $C = 3$, while the state on the right has $C = -3$. The remaining two configurations are obtained from these by a local in-plane spin rotation of π.

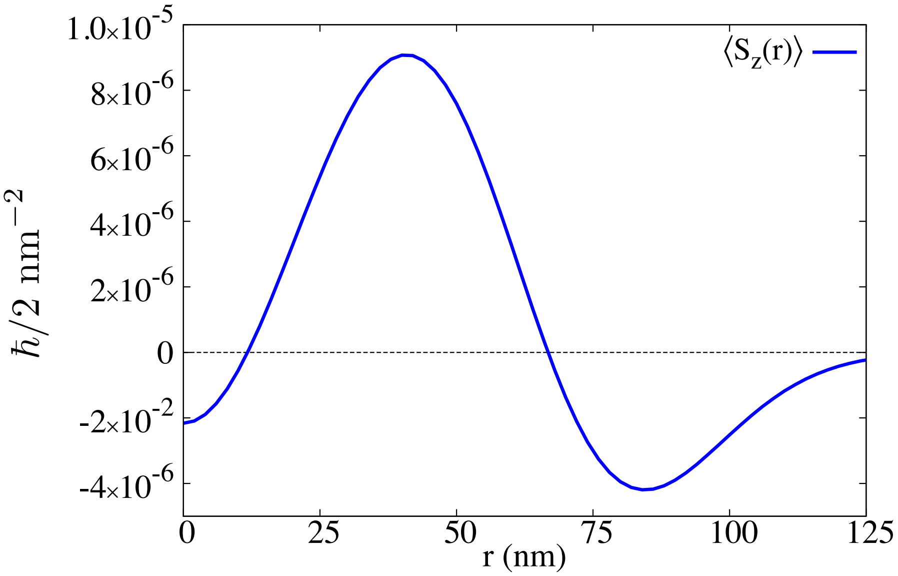

Figure 3.8: $\langle S_z(r) \rangle$ dependence on radius for $N = 5$ merons with $C = -3$.

Chapter 4

The Theory of Relaxation and Decoherence

To calculate relaxation and decoherence rates we use the formalism of density matrix theory. In order for our system to evolve from an initial nonequilibrium state to a final state of equilibrium, it must interact with an external system, or reservoir. As mentioned in Chap. 1, electron scattering with phonons are a common source of dissipation in QDs. At low temperature (T) only acoustic phonons are relevant in this process since scattering by higher energy optical phonons freezes out [63, 96]. In this chapter we develop the framework for the evolution of our QD system in the presence of an acoustic phonon reservoir in the T→ 0 limit.

4.1 Generalized Master Equation for a Dissipative Quantum System

In this section we develop the mathematical framework for considering relaxation processes in a general quantum system. Our framework follows closely that of Blum in ref. [97]. Consider a quantum system S interacting with a reservoir R. This quantum system will be our QD system whose Hamiltonian is described in Eq. (2.2), but for now we will keep the system general. The total Hamiltonian is $H = H_S + H_R + V$, where V describes the interaction between S and R. (Please note the hat notation $\hat{O}$ to denote an operator has been dropped for brevity.)

To determine how the system changes in time, we calculate the time evolution of the density matrix of the quantum system, $\rho(t)_S$. Specifically, we evaluate the Liouville equation in the interaction picture,

$$i\hbar \frac{\partial \rho(t)_I}{\partial t} = \Big[V(t)_I,\, \rho(t)_I \Big], \tag{4.1}$$

where $\rho(t)_I = e^{iH_0 t/\hbar} \rho(t) e^{-iH_0 t/\hbar}$ is the density operator of the *total* system in the interaction picture, $H_0 = H_S + H_R$, and $V(t)_I$ is the interaction operator in the interaction picture. Formal integration of Eq. (4.1) yields

$$\rho(t)_I = \rho(t_0)_I - \frac{i}{\hbar} \int_{t_0}^{t} \Big[V(t')_I,\, \rho(t')_I \Big] dt'. \tag{4.2}$$

Using the notation $\partial\rho(t)_I/\partial t \equiv \dot{\rho}(t)_I$ and inserting Eq. (4.2) into Eq. (4.1) yields

$$\begin{aligned}
\dot{\rho}(t)_I &= -\frac{i}{\hbar}\Big[V(t)_I,\, \rho(t)_I\Big] \\
&= -\frac{i}{\hbar}\Big(V(t)_I\rho(t)_I - \rho(t)_I V(t)_I\Big) \\
&= -\frac{i}{\hbar}\Big(V(t)_I\Big(\rho(t_0)_I - \frac{i}{\hbar}\int_{t_0}^{t}\Big[V(t')_I,\, \rho(t')_I\Big]dt'\Big) \\
&\qquad\qquad - \Big(\rho(t_0)_I - \frac{i}{\hbar}\int_{t_0}^{t}\Big[V(t')_I,\, \rho(t')_I\Big]dt'\Big)V(t)_I\Big) \\
&= -\frac{i}{\hbar}\Big[V(t)_I,\, \rho(t_0)_I\Big] - \frac{1}{\hbar^2}\int_{t_0}^{t}\Big[V(t)_I,\, \Big[V(t')_I,\, \rho(t')_I\Big]\Big]dt'.
\end{aligned} \tag{4.3}$$

We are only interested in the time evolution of the quantum system, therefore we trace out the elements of the reservoir: $\rho(t)_{SI} = \mathrm{tr}_R\{\rho(t)_I\}$. Then Eq. (4.3) becomes

$$\dot{\rho}(t)_{SI} = -\frac{i}{\hbar}\mathrm{tr}_R\Big[V(t)_I,\, \rho(t_0)_I\Big] - \frac{1}{\hbar^2}\int_{t_0}^{t}\mathrm{tr}_R\Big[V(t)_I,\, \Big[V(t')_I,\, \rho(t')_I\Big]\Big]dt'. \tag{4.4}$$

We assume that S is uncorrelated with R before time t_0. The density matrix for the total system at this initial time can be written as a product state, $\rho(t_0)_I = \rho(t_0)_{SI}\,\rho(t_0)_{RI}$.

A key assumption we make about the interaction between S and R is that, while R affects S, S has no effect on R; R remains indefinitely in thermal equilibrium at a constant temperature and is independent of time, $\rho(t)_{RI} = \rho(t_0)_{RI} = \rho_R$. Therefore, energy dissipated by S into R cannot be returned to S at a later time. This is known as the condition of irreversibility. The density matrix of the total system can then be written as

$$\rho(t)_I = \rho(t)_{SI}\,\rho_R, \tag{4.5}$$

where $\rho_R = (e^{-\beta H_R})/\mathcal{Z}$, $\beta = 1/k_BT$, k_B is Boltzmann's constant, T is temperature, and $\mathcal{Z} = \mathrm{tr}\left(e^{-\beta H_R}\right)$ is the reservoir partition function. Inserting Eq. (4.5) into Eq. (4.4), we get

$$\dot{\rho}(t)_{SI} = -\frac{i}{\hbar}\mathrm{tr}_R\Big[V(t)_I,\, \rho(t_0)_{SI}\,\rho_R\Big] - \frac{1}{\hbar^2}\int_{t_0}^{t}\mathrm{tr}_R\Big[V(t)_I,\, \Big[V(t')_I,\, \rho(t')_{SI}\,\rho_R\Big]\Big]dt'. \tag{4.6}$$

This equation of motion is valid to second order in the interaction. Higher order interaction terms are eliminated under the condition of irreversibility.

Another key assumption we use is that $\dot{\rho}(t)_{SI}$ depends only on $\rho(t)_{SI}$, its value at the present time t. In a manner of speaking, S has no memory. We refer to this as the Markov approximation. Then $\rho(t')_{SI} \to \rho(t)_{SI}$ and Eq. (4.6) becomes

$$\dot{\rho}(t)_{SI} = -\frac{i}{\hbar}\mathrm{tr}_R\Big[V(t)_I,\, \rho(t_0)_{SI}\,\rho_R\Big] - \frac{1}{\hbar^2}\int_{t_0}^{t} \mathrm{tr}_R\Big[V(t)_I,\, \Big[V(t')_I,\, \rho(t)_{SI}\,\rho_R\Big]\Big]dt'. \quad (4.7)$$

Regarding the interaction operator V, it is written as a product of S and R operators, $V = \sum_i F_i Q_i$, where F_i are reservoir operators and Q_i are operators that act only on the quantum system. In the interaction picture, the interaction operator is

$$\begin{aligned} V(t)_I &= e^{i(H_S+H_R)t/\hbar} V e^{-i(H_S+H_R)t/\hbar} \\ &= \sum_i F(t)_i Q(t)_i, \end{aligned} \quad (4.8)$$

where $F(t)_i = e^{iH_R t/\hbar} F_i e^{-iH_R t/\hbar}$ and $Q(t)_i = e^{iH_S t/\hbar} Q_i e^{-iH_S t/\hbar}$.

Consider the first term in Eq. (4.7). Since system operators commute with reservoir operators, and taking advantage of the fact that the trace allows for cyclic permutations, the first term becomes

$$\begin{aligned} &\mathrm{tr}_R\Big\{\sum_i F(t)_i Q(t)_i \rho(t_0)_{SI}\,\rho_R - \rho(t_0)_{SI}\,\rho_R \sum_i F(t)_i Q(t)_i\Big\} \\ &= \sum_i \Big(Q(t)_i \rho(t_0)_{SI} \mathrm{tr}_R\big\{F(t)_i \rho_R\big\} - \rho(t_0)_{SI} Q(t)_i \mathrm{tr}_R\big\{\rho_R F(t)_i\big\}\Big) \\ &= \sum_i \Big[Q(t)_i,\, \rho(t_0)_{SI}\Big]\mathrm{tr}_R\big\{F(t)_i \rho_R\big\}. \end{aligned}$$

Now, ρ_R is diagonal in the basis of the eigenstates of the reservoir. Taking the eigenstates to be $|N\rangle$, the trace above becomes $\mathrm{tr}_R\big\{F(t)_i\rho_R\big\} = \sum_N \langle N|\, F(t)_i\, |N\rangle \,\langle N|\, \rho_R\, |N\rangle$. The operator $F(t)_i$ is part of the interaction and is assumed to have no diagonal elements in this basis. Consequently, the trace $\mathrm{tr}_R\big\{F(t)_i\rho_R\big\} = 0$, and therefore the first term in Eq. (4.7) is zero, as well. The second term in Eq. (4.7) can be rewritten in a manner similar to the first term such that Eq. (4.7) becomes

$$\begin{aligned} \dot{\rho}(t)_{SI} = -\frac{1}{\hbar^2}\sum_{ij}\int_{t_0}^{t} \Big(&\Big[Q(t)_i, Q(t')_j\, \rho(t)_{SI}\Big]\mathrm{tr}_R\big\{F(t)_i\, F(t')_j\, \rho_R\big\} \\ &- \Big[Q(t)_i, \rho(t)_{SI}\, Q(t')_j\Big]\mathrm{tr}_R\big\{F(t')_j\, F(t)_i\, \rho_R\big\}\Big)dt'. \end{aligned} \quad (4.9)$$

Consider the trace $\mathrm{tr}_R\big\{F(t)_i\,F(t')_j\,\rho_R\big\}$ in the equation above:

$$\begin{aligned}
&\mathrm{tr}_R\big\{F(t)_i\,F(t')_j\,\rho_R\big\}\\
&=\mathrm{tr}_R\big\{e^{iH_Rt/\hbar}\,F_i\,e^{-iH_Rt/\hbar}\,e^{iH_Rt'/\hbar}\,F_j\,e^{-iH_Rt'/\hbar}\,\rho_R\big\}\\
&=\mathrm{tr}_R\big\{e^{iH_R(t-t')/\hbar}\,F_i\,e^{-iH_R(t-t')/\hbar}\,F_j\rho_R\big\}\\
&=\mathrm{tr}_R\big\{F(t-t')_i\,F_j\,\rho_R\big\}\\
&=\langle F(t-t')_i\,F_j\rangle.
\end{aligned}$$

Similarly, $\mathrm{tr}_R\big\{F(t')_j\,F(t)_i\,\rho_R\big\} = \langle F_j\,F(t-t')_i\rangle$. These expectation values are time correlation functions. They measure the correlation between the reservoir as it exists at time t and as it exists at time t'. Due to the previously mentioned assumptions about the reservoir, it is expected that these correlation functions tend to zero for values of $(t-t')$ that are much longer than the inherent correlation time of the reservoir, τ. This means that the result of Eq. (4.9) is nonzero only for time intervals $(t-t') \lesssim \tau$. For small values of τ this implies that $\dot{\rho(t)}_{SI}$ depends only on $\rho(t')$ for values of t' that lie within this time interval, i.e. t' values that are close to the present time, t. This is in keeping with the Markov approximation made above, where we have assumed that any changes in the system depend only on the present state of the system. This method neglects some details about the transient behaviour of the system on shorter time scales, however we are only interested in the behaviour of the system over long time scales $((t-t')>\tau)$.

We now consider the matrix elements of $\dot{\rho}(t)_{SI}$ in the basis of system eigenstates, $|m\rangle$. Note that

$$\langle m|\,Q(t)_i\,|n\rangle = e^{i\omega_{mn}t}\,\langle m|\,Q\,|n\rangle\,, \tag{4.10}$$

where

$$\omega_{mn} = (E_m - E_n)/\hbar. \tag{4.11}$$

Then the matrix elements of $\rho(t)_{SI}$ become,

$$\begin{aligned}\dot{\rho}(t)_{m'm} = -\frac{1}{\hbar^2}\sum_{ij}\Bigg\{&\sum_{kn'n}\int_{t_0}^{t} e^{i\omega_{m'k}t}\langle m'|Q_i|k\rangle e^{i\omega_{kn'}t'}\langle k|Q_j|n'\rangle\langle n'|\rho(t)|n\rangle\delta_{mn}\langle F(t-t')_i F_j\rangle dt' \\ &-\sum_{n'n}\int_{t_0}^{t} e^{i\omega_{m'n'}t'}\langle m'|Q_j|n'\rangle\langle n'|\rho(t)|n\rangle e^{i\omega_{nm}t}\langle n|Q_i|m\rangle\langle F(t-t')_i F_j\rangle dt' \\ &-\sum_{n'n}\int_{t_0}^{t} e^{i\omega_{m'n'}t}\langle m'|Q_i|n'\rangle\langle n'|\rho(t)|n\rangle e^{i\omega_{nm}t'}\langle n|Q_j|m\rangle\langle F_j F(t-t')_i\rangle dt' \\ &+\sum_{kn'n}\int_{t_0}^{t}\langle n'|\rho(t)|n\rangle e^{i\omega_{nk}t'}\langle n|Q_j|k\rangle e^{i\omega_{km}t}\langle k|Q_i|m\rangle\delta_{m'n'}\langle F_j F(t-t')_i\rangle dt'\Bigg\}\end{aligned} \tag{4.12}$$

which reduces to

$$\begin{aligned}\dot{\rho}(t)_{m'm} &= \sum_{n'n}\rho(t)_{n'n}\, e^{i(\omega_{nm}+\omega_{m'n'})t} \\ &\quad\times\Big\{\Gamma^+(t)_{nmm'n'} + \Gamma^-(t)_{nmm'n'} - \sum_k\Big(\delta_{mn}\Gamma^+(t)_{m'kkn'} + \delta_{m'n'}\Gamma^-(t)_{nkkm}\Big)\Big\} \\ &= \sum_{n'n}\rho(t)_{n'n}\, e^{i(\omega_{nm}+\omega_{m'n'})t}\, R_{m'mn'n}(t),\end{aligned} \tag{4.13}$$

where

$$\Gamma^+(t)_{abcd} = \frac{1}{\hbar^2}\sum_{ij}\langle a|Q_i|b\rangle\langle c|Q_j|d\rangle\int_{t_0}^{t} e^{-i\omega_{cd}(t-t')}\langle F(t-t')_i F_j\rangle dt', \tag{4.14a}$$

$$\Gamma^-(t)_{abcd} = \frac{1}{\hbar^2}\sum_{ij}\langle a|Q_j|b\rangle\langle c|Q_i|d\rangle\int_{t_0}^{t} e^{-i\omega_{ab}(t-t')}\langle F_j F(t-t')_i\rangle dt', \tag{4.14b}$$

where $(\Gamma^-(t)_{abcd})^* = \Gamma^+(t)_{dcba}$[1], and $R_{m'mn'n}(t)$ are elements of the Redfield tensor. Note that in evaluating the matrix elements of $\rho(t)_{SI}$ above we have dropped the subscript SI. From this point onward the density matrix for the system in the interaction picture will be shortened to $\rho(t)$.

Recall that the correlation functions tend to zero as $(t - t') \gg \tau$. Therefore, under the Markov approximation, we can extend the upper limit of the integrals in Eq. (4.14) to infinity. Also, we assume the reservoir and system have always been in

---

[1] Upon evaluating these elements in our system, $\Gamma^+(t)_{abcd}$ and $\Gamma^-(t)_{abcd}$ are in fact real, so that $\Gamma^-(t)_{abcd} = \Gamma^+(t)_{dcba}$. This is not generally true.

contact, and take the lower limit of the above integrals to be negative infinity. With the change of variables $t'' = (t - t')$, the functions in Eq. (4.14) become

$$\Gamma^{+}_{abcd} = \frac{1}{\hbar^2} \sum_{ij} \langle a|Q_i|b\rangle\langle c|Q_j|d\rangle \int_{-\infty}^{\infty} e^{-i\omega_{cd}t''} \langle F(t'')_i F_j\rangle dt'', \tag{4.15a}$$

$$\Gamma^{-}_{abcd} = \frac{1}{\hbar^2} \sum_{ij} \langle a|Q_j|b\rangle\langle c|Q_i|d\rangle \int_{-\infty}^{\infty} e^{-i\omega_{ab}t''} \langle F_j F(t'')_i\rangle dt'', \tag{4.15b}$$

and they, along with the elements of the Redfield tensor, are no longer time-dependent. Our final form of $\dot{\rho}(t)_{m'm}$ is

$$\dot{\rho}(t)_{m'm} = \sum_{n'n} \rho(t)_{n'n}\, e^{i(\omega_{nm}+\omega_{m'n'})t}\, R_{m'mn'n}, \tag{4.16a}$$

where

$$R_{m'mn'n} = \Gamma^{+}_{nmm'n'} + \Gamma^{-}_{nmm'n'} - \sum_{k} \Big(\delta_{mn} \Gamma^{+}_{m'kkn'} + \delta_{m'n'} \Gamma^{-}_{nkkm} \Big). \tag{4.16b}$$

It is worth noting that we do *not* make the secular approximation, as discussed by Blum in Ref. [97]. The secular approximation assumes that the energy levels of the system are far apart such that, except in the case where $E_{m'} = E_m$ and $E_{n'} = E_n$, or where $E_m = E_n$ and $E_{m'} = E_{n'}$, the exponential term in Eq. (4.16a) oscillates rapidly and averages to zero over the time-scale investigated. In this dissertation we examine situations where the energy levels of the system are close to each other, such as near a degeneracy point. We therefore do not apply the secular approximation to our model.

In Eq. (4.16) we have developed a general expression for evaluating the time-evolution of a general quantum system in dissipative contact with a general vast reservoir. This expression is our *generalized Master equation*, where it assumes the reservoir does not change in time despite interacting with the system, and we have taken the Markov approximation where any change in the system depends only on its current state.

We are specifically interested in how the QD system as described in Chap. 2 evolves in time when coupled to a phonon reservoir. In the next section we introduce the electron-phonon interaction as our interaction operator V and specify the types of electron-phonon interactions expected to contribute to the evolution of the QD system. In Sec. 4.3 we tailor our generalized Master equation to the QD system coupled with the phonon reservoir.

4.2 Electron-Phonon Interaction

As mentioned previously, we consider interactions with acoustic phonons only. Specifically we consider long-wavelength (small wave-vector $\mathbf{q}$) acoustic phonons. In this regard the acoustic phonon dispersion curve is approximated as linear, with $\omega_q = c_\nu q$ where c_ν is the speed of sound in the semiconductor.

We examine two different mechanisms for electron-phonon couplings: Coupling induced by the deformation potential and coupling induced by the piezoelectric effect. Both types of electron-acoustic phonon interactions have been shown, experimentally and theoretically, to play a role in electron relaxation processes in a QD [28, 98–101].

Deformation potentials arise from the deformation of the crystal lattice, where the atoms of the semiconductor are displaced from their equilibrium positions due to their interactions with charge carriers. It is treated as a perturbation of the electronic energies due to the lattice vibration [63]. In GaAs, the conduction band minimum is at the Γ-point ($\mathbf{k}$=0) and is nondegenerate[2] (spin degeneracy aside). Therefore, for long wavelength phonons, only longitudinal phonons are significant [103].

GaAs is a weakly piezoelectric semiconductor, where a stress in the crystal lattice induces a global electric field that is proportional to the stress [63, 103]. The induced electric field points in the direction of the phonon. This is known as the piezoelectric effect. The piezoelectric electron-phonon interaction is anisotropic, and depends on the polarization (longitudinal or transverse) of the acoustic phonon. We therefore look at both cases.

In general the electron-phonon interaction can be expressed as

$$V = \sum_{ij} c_i^\dagger c_j \sum_{\mathbf{q}} \left(\gamma_{\mathbf{q}}^{ij} b_{\mathbf{q}} + (\gamma_{\mathbf{q}}^{ji})^* b_{\mathbf{q}}^\dagger \right) \tag{4.17}$$

where $c_i^\dagger$ and c_i are the same second quantized Fermi operators introduced in Chap. 3 which create or annihilate an electron in state i, and $b_{\mathbf{q}}^\dagger$ and $b_{\mathbf{q}}$ are second quantized Bose operators which create or annihilate a phonon with wave vector $\mathbf{q}$. The coefficients $\gamma_{\mathbf{q}}^{ij}$ and $(\gamma_{\mathbf{q}}^{ji})^*$ depend on the explicit electron-phonon interaction. This interaction conserves the spin of the electron. Note that V is Hermitian. In contrast

---

[2] The conduction band in GaAs *can* be made degenerate if it is strongly n-doped (e.g. $n \approx 10^{19}$ cm^{-3}), which raises the Fermi energy to or above the conduction band energy [102]. In our system we assume the doping of the GaAs layer of the quantum well to be intrinsic or very weak.

with the general expression $V = \sum_i F_i Q_i$, we see that

$$F_{ij} = \sum_{\mathbf{q}} \left(\gamma_{\mathbf{q}}^{ij} b_{\mathbf{q}} + (\gamma_{\mathbf{q}}^{ji})^* b_{\mathbf{q}}^{\dagger} \right), \tag{4.18}$$

and

$$Q_{ij} = c_i^{\dagger} c_j \tag{4.19}$$

and the sum is taken over two indices.

The coefficients $\gamma_{\mathbf{q}}^{ij}$ $((\gamma_{\mathbf{q}}^{ji})^*)$ can be expressed as follows:

$$\begin{aligned} \gamma_{\mathbf{q}}^{ij,\,\nu} &\equiv M_\nu(\mathbf{q})\, (i|\, e^{i\mathbf{q}\cdot\mathbf{r}}\, |j) \\ &= M_\nu(\mathbf{q}) \int \psi_i^*(\boldsymbol{r}) \psi_j(\boldsymbol{r}) e^{i\mathbf{q}\cdot\mathbf{r}} d^3\boldsymbol{r}, \end{aligned} \tag{4.20}$$

where the index ν is used to denote a specific type of electron-phonon interaction. Here $|i)$ is a single-electron state, $\psi_i(\boldsymbol{r})$ is the three-dimensional position-space representation of the electron state, and $M_\nu(\mathbf{q})$ is the matrix element of the electron-phonon interaction. We examine the same electron-phonon interactions studied by Climente *et al.* in references [20, 100, 101]. Specifically, we look at the deformation potential by longitudinal acoustic phonons (ν = LA-DP), the piezoelectric effect by longitudinal acoustic phonons (ν = LA-PZ), and the piezoelectric effect by transverse acoustic phonons (ν = TA-PZ). In each case, the matrix element $M_\nu(\mathbf{q})$ takes on the following values:

$$|M_{LA-DP}(\mathbf{q})|^2 = \frac{\hbar D^2}{2\, d\, c_{LA} \mathrm{V}} |\mathbf{q}|, \tag{4.21}$$

$$|M_{LA-PZ}(\mathbf{q})|^2 = \frac{32\pi^2 \hbar e^2 h_{14}^2}{\epsilon^2\, d\, c_{LA} \mathrm{V}} \frac{(3 q_x q_y q_z)^2}{|\mathbf{q}|^7}, \tag{4.22}$$

$$|M_{TA-PZ}(\mathbf{q})|^2 = \frac{32\pi^2 \hbar e^2 h_{14}^2}{\epsilon^2\, d\, c_{TA} \mathrm{V}} \times \left| \frac{q_x^2 q_y^2 + q_y^2 q_z^2 + q_z^2 q_x^2}{|\mathbf{q}|^5} - \frac{(3 q_x q_y q_z)^2}{|\mathbf{q}|^7} \right|, \tag{4.23}$$

where c_{LA} is the sound velocity of the longitudinal acoustic phonon mode in the semiconductor, c_{TA} is the sound velocity of the transverse acoustic phonon mode, D is the deformation constant for the semiconductor, d is the semiconductor density, V is the semiconductor volume, and h_{14} is the piezoelectric constant for semiconductors with zinc-blende structure. As before, e is the magnitude of the electron charge, and ϵ is the semiconductor dielectric constant. Note the matrix element in Eq. (4.23) takes into consideration the two transverse phonon modes [104]. A derivation of the deformation potential electron-acoustic phonon interaction is given by Mahan in ref. [103], and a derivation of the piezoelectric electron-acoustic phonon interaction is given by Zook in ref. [104]. We use the following GaAs parameters: $D = 8.6$ eV, $d = 5310$ kg/m^3, and $h_{14} = 1.41 \times 10^9$ V/m. With the growth of the QD in the z (<100> type) direction, we take the acoustic phonon speeds to be $c_{LA} = 4.72 \times 10^3$ m/s and $c_{TA} = 3.34 \times 10^3$ m/s [20, 100, 101].

4.3 Electron Relaxation and Decoherence in a Quantum Dot

In this section we apply our generalized Master equation in Eq. (4.16) to our QD model in consideration of the electron-phonon interactions discussed above. Consider first the reservoir correlation functions, $\langle F(t{-}t')_{ij}\, F_{mn}\rangle$ and $\langle F_{mn}\, F(t{-}t')_{ij}\rangle$, where the reservoir operator F_{ij} is defined in Eq. (4.18). The reservoir is a bath of noninteracting bosons (acoustic phonons) with Hamiltonian

$$H_R = \sum_{\mathbf{k}} \epsilon_k\, b^\dagger_{\mathbf{k}} b_{\mathbf{k}}. \tag{4.24}$$

The sum in the above equation runs over a continuous number of **k**-states in the reservoir. For a linear dispersion, the energy eigenvalues are taken to be

$$\epsilon_k = \hbar\omega_k = \hbar c_\nu k, \tag{4.25}$$

We assume the particle number of the reservoir is not fixed. The complete set of reservoir states can be expressed as

$$\begin{aligned} &\sum_{n_1}\sum_{n_2}\sum_{n_3} \cdots |n_1\mathbf{k}_1\; n_2\mathbf{k}_2\; n_3\mathbf{k}_3 \cdots\rangle \\ \equiv &\sum_{\{n_\lambda\}} |\vec{n}\rangle\,, \end{aligned} \tag{4.26}$$

where $\{n_\lambda\}$ is the set of occupation numbers which specifies the reservoir eigenstate: Each single-particle state $\mathbf{k}_i$ can have n_i bosons, where n_i can range from 0 to infinity.

The reservoir operators H_R, $b^\dagger_{\mathbf{k}}$, and $b_{\mathbf{k}}$ act in the following ways on the reservoir eigenstates:

$$\begin{aligned} H_R \left| n_1\mathbf{k}_1\, n_2\mathbf{k}_2 \cdots \right\rangle &= (n_1\epsilon_{k_1} + n_2\epsilon_{k_2} + \cdots) \left| n_1\mathbf{k}_1\, n_2\mathbf{k}_2 \cdots \right\rangle \\ &\equiv E_{\vec{n}} \left| \vec{n} \right\rangle \qquad (4.27) \\ b^\dagger_{\mathbf{k}} \left| n_1\mathbf{k}_1\, n_2\mathbf{k}_2 \cdots \right\rangle &= \sum_\alpha \delta_{kk_\alpha} \sqrt{n_\alpha + 1} \left| \cdots (n_\alpha + 1)\mathbf{k}_\alpha \cdots \right\rangle \qquad (4.28) \\ b_{\mathbf{k}} \left| n_1\mathbf{k}_1\, n_2\mathbf{k}_2 \cdots \right\rangle &= \sum_\alpha \delta_{kk_\alpha} \sqrt{n_\alpha} \left| \cdots (n_\alpha - 1)\mathbf{k}_\alpha \cdots \right\rangle \qquad (4.29) \end{aligned}$$

The partition function $\mathcal{Z}$ of this reservoir can be expressed as

$$\mathcal{Z} = \Pi_i\, \mathcal{Z}_i = \sum_{\{n_\lambda\}} e^{-\beta E_{\vec{n}}}, \qquad (4.30)$$

where for bosons,

$$\mathcal{Z}_i = \sum_{n_i=0}^{\infty} e^{-\beta n_i \epsilon_i} = \frac{1}{1 - e^{-\beta\epsilon_i}}. \qquad (4.31)$$

We now evaluate the correlation function $\langle F(t-t')_{ij}\, F_{mn} \rangle$. For a general electron-phonon interaction, and in the interaction picture,

$$\begin{aligned} F(t)_{ij}\, F_{mn} &= e^{iH_R t/\hbar}\, F_{ij}\, e^{-iH_R t/\hbar}\, F_{mn} \\ &= \sum_{\mathbf{q}\mathbf{q}'} e^{iH_R t/\hbar} \left(\gamma^{ij}_{\mathbf{q}} b_{\mathbf{q}} + (\gamma^{ji}_{\mathbf{q}})^* b^\dagger_{\mathbf{q}} \right) e^{-iH_R t/\hbar} \left(\gamma^{mn}_{\mathbf{q}'} b_{\mathbf{q}'} + (\gamma^{nm}_{\mathbf{q}'})^* b^\dagger_{\mathbf{q}'} \right). \end{aligned}$$

We keep only particle-conserving terms since, upon taking the trace over the reservoir states when evaluating the expectation value in the next step, non-particle conserving terms ($\propto b_{\mathbf{q}}\, b_{\mathbf{q}'}$, $b^\dagger_{\mathbf{q}}\, b^\dagger_{\mathbf{q}'}$) will give zero. The correlation function becomes

$$\begin{aligned} \langle F(t)_{ij}\, F_{mn} \rangle = \mathrm{tr}_R \Bigg\{ \frac{e^{-\beta H_R}}{\mathcal{Z}} \sum_{\mathbf{q}\mathbf{q}'} e^{iH_R t/\hbar} \Big[&(\gamma^{ji}_{\mathbf{q}})^* \gamma^{mn}_{\mathbf{q}'} b^\dagger_{\mathbf{q}} e^{-iH_R t/\hbar} b_{\mathbf{q}'} \\ &+ \gamma^{ij}_{\mathbf{q}} (\gamma^{nm}_{\mathbf{q}'})^* b_{\mathbf{q}} e^{-iH_R t/\hbar} b^\dagger_{\mathbf{q}'} \Big] \Bigg\}. \qquad (4.32) \end{aligned}$$

Consider the first term. The trace is

$$\frac{1}{\mathcal{Z}} \sum_{\{n_\lambda\}} \sum_{\mathbf{q}\mathbf{q}'} (\gamma^{ji}_{\mathbf{q}})^* \gamma^{mn}_{\mathbf{q}'} \left\langle \vec{n} \right| e^{-\beta H_R} e^{iH_R t/\hbar} b^\dagger_{\mathbf{q}} e^{-iH_R t/\hbar} b_{\mathbf{q}'} \left| \vec{n} \right\rangle. \qquad (4.33)$$

Using Eqs. (4.27), (4.28) and (4.29) this becomes

$$\begin{aligned}
&\frac{1}{\mathcal{Z}}\sum_{\{n_\lambda\}}\sum_{\mathbf{q}\mathbf{q}'}(\gamma_{\mathbf{q}}^{ji})^*\gamma_{\mathbf{q}'}^{mn}e^{-\beta E_{\vec{n}}}e^{iE_{\vec{n}}t/\hbar}\sum_{\alpha\alpha'}\delta_{\mathbf{q}\mathbf{k}_\alpha}\delta_{\mathbf{q}'\mathbf{k}_{\alpha'}}\sqrt{n_\alpha}\sqrt{n_{\alpha'}}e^{-i(E_{\vec{n}}-\epsilon_{k_{\alpha'}})t/\hbar} \\
&\qquad\qquad\qquad\qquad\qquad\qquad\qquad\qquad \times\langle\cdots(n_\alpha-1)\mathbf{k}_\alpha\cdots|\cdots(n_{\alpha'}-1)\mathbf{k}_{\alpha'}\cdots\rangle \\
&=\frac{1}{\mathcal{Z}}\sum_{\{n_\lambda\}}\sum_{\mathbf{q}\mathbf{q}'}(\gamma_{\mathbf{q}}^{ji})^*\gamma_{\mathbf{q}'}^{mn}e^{-\beta E_{\vec{n}}}e^{iE_{\vec{n}}t/\hbar}\sum_{\alpha\alpha'}\delta_{\mathbf{q}\mathbf{k}_\alpha}\delta_{\mathbf{q}'\mathbf{k}_{\alpha'}}\sqrt{n_\alpha}\sqrt{n_{\alpha'}}e^{-i(E_{\vec{n}}-\epsilon_{k_{\alpha'}})t/\hbar}\delta_{\alpha\alpha'} \\
&=\frac{1}{\mathcal{Z}}\sum_{\{n_\lambda\}}\sum_{\mathbf{q}\mathbf{q}'}(\gamma_{\mathbf{q}}^{ji})^*\gamma_{\mathbf{q}'}^{mn}e^{-\beta E_{\vec{n}}}e^{iE_{\vec{n}}t/\hbar}\sum_{\alpha\alpha'}\delta_{\mathbf{q}\mathbf{k}_\alpha}\delta_{\mathbf{q}'\mathbf{k}_{\alpha'}}\sqrt{n_\alpha}\sqrt{n_{\alpha'}}e^{-i(E_{\vec{n}}-\epsilon_{k_{\alpha'}})t/\hbar}\delta_{\alpha\alpha'} \\
&=\frac{1}{\mathcal{Z}}\sum_{\{n_\lambda\}}\sum_{\mathbf{q}\mathbf{q}'}(\gamma_{\mathbf{q}}^{ji})^*\gamma_{\mathbf{q}'}^{mn}e^{-\beta E_{\vec{n}}}\sum_{\alpha}\delta_{\mathbf{q}\mathbf{k}_\alpha}\delta_{\mathbf{q}'\mathbf{k}_\alpha}n_\alpha e^{i\epsilon_{k_\alpha}t/\hbar} \\
&=\frac{1}{\mathcal{Z}}\sum_{\{n_\lambda\}}\sum_{\mathbf{q}}(\gamma_{\mathbf{q}}^{ji})^*\gamma_{\mathbf{q}}^{mn}\,e^{-\beta E_{\vec{n}}}\,n_q\,e^{i\epsilon_q t/\hbar}.
\end{aligned} \tag{4.34}$$

Note that $n_q\,e^{-\beta E_{\vec{n}}}=-\frac{1}{\beta}\frac{\partial}{\partial\epsilon_q}e^{-\beta E_{\vec{n}}}$. Then the last line in Eq. (4.34) becomes

$$\begin{aligned}
&\frac{1}{\mathcal{Z}}\sum_{\mathbf{q}}(\gamma_{\mathbf{q}}^{ji})^*\gamma_{\mathbf{q}}^{mn}e^{i\epsilon_q t/\hbar}\left(-\frac{1}{\beta}\right)\frac{\partial}{\partial\epsilon_q}\sum_{\{n_\lambda\}}e^{-\beta E_{\vec{n}}} \\
&=\frac{1}{\mathcal{Z}}\sum_{\mathbf{q}}(\gamma_{\mathbf{q}}^{ji})^*\gamma_{\mathbf{q}}^{mn}e^{i\epsilon_q t/\hbar}\left(-\frac{1}{\beta}\right)\frac{\partial}{\partial\epsilon_q}\mathcal{Z} \\
&=\frac{1}{\mathcal{Z}}\sum_{\mathbf{q}}(\gamma_{\mathbf{q}}^{ji})^*\gamma_{\mathbf{q}}^{mn}e^{i\epsilon_q t/\hbar}\left(-\frac{1}{\beta}\right)\left(-\frac{\beta e^{-\beta\epsilon_q}}{1-e^{-\beta\epsilon_q}}\mathcal{Z}\right) \\
&=\sum_{\mathbf{q}}(\gamma_{\mathbf{q}}^{ji})^*\gamma_{\mathbf{q}}^{mn}e^{i\epsilon_q t/\hbar}\left(\frac{1}{e^{\beta\epsilon_q}-1}\right),
\end{aligned} \tag{4.35}$$

where $1/(e^{\beta\epsilon_q}-1)$ is the Bose-Einstein distribution for the phonon state $\mathbf{q}$ (the chemical potential $\mu=0$).

In a similar manner, the second term in Eq. (4.32) reduces to

$$\sum_{\mathbf{q}}\gamma_{\mathbf{q}}^{ij}(\gamma_{\mathbf{q}}^{nm})^*e^{-i\epsilon_q t/\hbar}\left(\frac{1}{1-e^{-\beta\epsilon_q}}\right). \tag{4.36}$$

Then the correlation functions become

$$\langle F(t)_{ij}\,F_{mn}\rangle=\sum_{\mathbf{q}}\left\{(\gamma_{\mathbf{q}}^{ji})^*\gamma_{\mathbf{q}}^{mn}\left(\frac{e^{i\epsilon_q t/\hbar}}{e^{\beta\epsilon_q}-1}\right)+\gamma_{\mathbf{q}}^{ij}(\gamma_{\mathbf{q}}^{nm})^*\left(\frac{e^{-i\epsilon_q t/\hbar}}{1-e^{-\beta\epsilon_q}}\right)\right\} \tag{4.37a}$$

$$\langle F_{mn}\,F(t)_{ij}\rangle=\sum_{\mathbf{q}}\left\{\gamma_{\mathbf{q}}^{ij}(\gamma_{\mathbf{q}}^{nm})^*\left(\frac{e^{-i\epsilon_q t/\hbar}}{e^{\beta\epsilon_q}-1}\right)+(\gamma_{\mathbf{q}}^{ji})^*\gamma_{\mathbf{q}}^{mn}\left(\frac{e^{i\epsilon_q t/\hbar}}{1-e^{-\beta\epsilon_q}}\right)\right\}. \tag{4.37b}$$

At this point we apply the zero-temperature limit. As T $\rightarrow 0$ ($\beta \rightarrow \infty$), only the second terms in Eqs. (4.37a) and (4.37b) are retained, since

$$\lim_{\beta\rightarrow\infty} \frac{1}{e^{\beta\epsilon_q}-1} = 0$$
$$\lim_{\beta\rightarrow\infty} \frac{1}{1-e^{-\beta\epsilon_q}} = 1.$$

This indicates that, as T$\rightarrow 0$, phonons cannot be emitted by the reservoir; they can only be absorbed. The correlation functions reduce to

$$\langle F(t)_{ij}\, F_{mn}\rangle = \sum_{\mathbf{q}} \gamma_{\mathbf{q}}^{ij}(\gamma_{\mathbf{q}}^{nm})^* e^{-i\epsilon_q t/\hbar} \tag{4.38a}$$

$$\langle F_{mn}\, F(t)_{ij}\rangle = \sum_{\mathbf{q}} (\gamma_{\mathbf{q}}^{ji})^* \gamma_{\mathbf{q}}^{mn} e^{i\epsilon_q t/\hbar}. \tag{4.38b}$$

We now reconsider the expressions $\Gamma^{+}_{nmm'n'}$ and $\Gamma^{-}_{nmm'n'}$ from our generalized Master equation (see Eqs. (4.15) and (4.16)). Using Eq. (4.38) above, $\Gamma^{+}_{nmm'n'}$ becomes

$$\begin{aligned}
\Gamma^{+}_{nmm'n'} &= \frac{1}{\hbar^2}\sum_{ijkl} \langle n|Q_{ij}|m\rangle\langle m'|Q_{kl}|n'\rangle \int_{-\infty}^{\infty} e^{-i\omega_{m'n'}t}\langle F(t)_{ij}F_{kl}\rangle dt \\
&= \frac{1}{\hbar^2}\sum_{ijkl}\langle n|Q_{ij}|m\rangle\langle m'|Q_{kl}|n'\rangle\sum_{\mathbf{q}} \gamma_{\mathbf{q}}^{ij}(\gamma_{\mathbf{q}}^{lk})^* \int_{-\infty}^{\infty} e^{-i\omega_{m'n'}t}e^{-i\epsilon_q t/\hbar}dt \\
&= \frac{2\pi}{\hbar^2 c_\nu}\sum_{ijkl}\langle n|Q_{ij}|m\rangle\langle m'|Q_{kl}|n'\rangle\sum_{\mathbf{q}} \gamma_{\mathbf{q}}^{ij}(\gamma_{\mathbf{q}}^{lk})^*\delta(q-q_{n'm',\nu}),
\end{aligned} \tag{4.39}$$

where we have defined the quantity

$$q_{nm,\nu} \equiv \frac{\omega_{nm}}{c_\nu} = \frac{E_n - E_m}{\hbar c_\nu}, \tag{4.40}$$

and used the identity for the Dirac delta function $\delta(x) = \frac{1}{2\pi}\int_{-\infty}^{\infty} e^{ixk}dk$.

Similarly, $\Gamma^{-}_{nmm'n'}$ becomes

$$\Gamma^{-}_{nmm'n'} = \frac{2\pi}{\hbar^2 c_\nu}\sum_{ijkl} \langle n|Q_{kl}|m\rangle\langle m'|Q_{ij}|n'\rangle \sum_{\mathbf{q}}(\gamma_{\mathbf{q}}^{ji})^*\gamma_{\mathbf{q}}^{kl}\delta(q-q_{nm,\nu}). \tag{4.41}$$

Consider next the sum over $\mathbf{q}$. For a d-dimensional system, we can convert a sum to an integral in the following manner [105]:

$$\sum_{\mathbf{k}} \rightarrow \frac{\mathrm{V}}{(2\pi)^d}\int d^d\mathbf{k}, \tag{4.42}$$

where V is the volume of the system, and $\mathrm{V}/(2\pi)^d$ is the density of states in **k**-space. From Eq. (4.20), let

$$\gamma_{\mathbf{q}}^{ij,\,\nu} \equiv M_\nu(\mathbf{q})\widetilde{\gamma}_{\mathbf{q}}^{ij}. \tag{4.43}$$

Furthermore, from Eqs. (4.21), (4.22), and (4.23), let

$$|M_\nu(\mathbf{q})|^2 \equiv \frac{1}{\mathrm{V}}|\widetilde{M}_\nu(\mathbf{q})|^2. \tag{4.44}$$

Then $\gamma_{\mathbf{q}}^{ij,\,\nu}(\gamma_{\mathbf{q}}^{lk,\,\nu})^* = \frac{1}{\mathrm{V}}|\widetilde{M}_\nu(\mathbf{q})|^2\widetilde{\gamma}_{\mathbf{q}}^{ij}(\widetilde{\gamma}_{\mathbf{q}}^{lk})^*$. The elements $\Gamma^+_{nmm'n'}$ and $\Gamma^-_{nmm'n'}$ can be written in terms of an integral over **q**,

$$\Gamma^+_{nmm'n'} = \frac{1}{(2\pi\hbar)^2 c_\nu}\sum_{ijkl}\langle n|Q_{ij}|m\rangle\langle m'|Q_{kl}|n'\rangle\int d^3\mathbf{q}|\widetilde{M}_\nu(\mathbf{q})|^2\widetilde{\gamma}_{\mathbf{q}}^{ij}(\widetilde{\gamma}_{\mathbf{q}}^{lk})^*\delta(q-q_{n'm',\nu}), \tag{4.45a}$$

$$\Gamma^-_{nmm'n'} = \frac{1}{(2\pi\hbar)^2 c_\nu}\sum_{ijkl}\langle n|Q_{kl}|m\rangle\langle m'|Q_{ij}|n'\rangle\int d^3\mathbf{q}|\widetilde{M}_\nu(\mathbf{q})|^2(\widetilde{\gamma}_{\mathbf{q}}^{ji})^*\widetilde{\gamma}_{\mathbf{q}}^{kl}\delta(q-q_{nm,\nu}), \tag{4.45b}$$

for the specific electron-phonon interaction ν. To evaluate the **q** integral, we write the phonon momentum using spherical coordinates,

$$\mathbf{q} = q(\cos\theta_q\sin\phi_q, \sin\theta_q\sin\phi_q, \cos\phi_q), \tag{4.46}$$

where $\int d^3\mathbf{q} \to \int_0^\infty dq\int_0^{2\pi} d\theta_q\int_0^\pi d\phi_q\, q^2\sin\phi_q$.

At this point we consider the expansion of the coefficients $\widetilde{\gamma}_{\mathbf{q}}^{ij}$ and $(\widetilde{\gamma}_{\mathbf{q}}^{lk})^*$. From Eqs. (4.20) and (4.43),

$$\widetilde{\gamma}_{\mathbf{q}}^{ij} = \int \psi_i^*(\boldsymbol{r})\psi_j(\boldsymbol{r})e^{i\mathbf{q}\cdot\mathbf{r}}d^3\boldsymbol{r} = \int_0^\infty dr\int_{-\pi}^{\pi} d\theta\int_{-\infty}^{\infty} dz\, r\,\phi_i^*(r,\theta)\phi_j(r,\theta)\xi(z)^2e^{i\mathbf{q}\cdot\mathbf{r}}. \tag{4.47}$$

The three-dimensional position-space representation of the electron in the QD, is

$$\psi_i(\boldsymbol{r}) = \phi_i(r,\theta)\xi(z) \tag{4.48}$$

where $\phi_i(r,\theta)$ is the position-space representation of the QD orbitals (see Eq. (2.5)) and $\xi(z)$ is the ground state of the quantum square well in the z-direction (see Eq. (2.1)). (The azimuthal direction in position space, θ, is not to be confused with the azimuthal direction in momentum space, θ_q.) Note that the indices i and j in Eq. (4.47) each represent a different set of orbital quantum, n and m. As such, the sum $\sum_{ijkl}$ in the Redfield tensor elements is in fact a sum over eight different indices (four sets of n and m). The integration over θ involves the angular part of the QD orbital wave function, $e^{im'\theta}$, and the position-space azimuthal angle of $e^{i\mathbf{q}\cdot\mathbf{r}}$ in Eq. (4.47), and can be done analytically. Eq. (4.47) becomes

$$\begin{aligned}\widetilde{\gamma}^{ij}_{\mathbf{q}} &= 2\pi e^{-i\widetilde{m}_{ij}(\theta_q-\pi/2)}\int_0^\infty dr\, r\, \mathrm{R}_{n_i m_i}(r)\mathrm{R}_{n_j m_j}(r)\mathrm{J}_{\widetilde{m}_{ij}}(qr\sin\phi_q)\int_{-\infty}^{\infty} dz\, \xi(z)^2 e^{iqz\cos\phi_q}\\ &= 2\pi e^{-i\widetilde{m}_{ij}(\theta_q-\pi/2)}\mathbb{I}^{ij}_r(q,\phi_q)\mathbb{I}_z(q,\phi_q),\end{aligned} \tag{4.49}$$

where $\widetilde{m}_{ij} = m'_i - m'_j$ ($m' = n - m$, see Eq. (2.5)), $\mathrm{R}_{n_i m_i}(r) = \frac{(-1)^{n_{r_i}}}{\sqrt{2\pi}l_0}\sqrt{\frac{n_{r_i}!}{(n_{r_i}+|m'_i|)!}} \times e^{-r^2/(4l_0^2)}\left(\frac{r}{\sqrt{2}l_0}\right)^{|m'_i|} L^{|m'_i|}_{n_{r_i}}\left(\frac{r^2}{2l_0^2}\right)$ is the radial part of the QD orbital, and $\mathrm{J}_n(x)$ is the Bessel function of the first kind. In the second line of Eq. (4.49), $\mathbb{I}^{ij}_r(q,\phi_q)$ represents the integration over r; it returns a function of q and ϕ_q. Similarly, $\mathbb{I}_z(q,\phi_q)$ represents the integration over z, which also returns a function of q and ϕ_q. The decoupling of the vertical, or growth-direction (z), component of $\widetilde{\gamma}^{ij}_{\mathbf{q}}$ from the lateral (x, y) component is a reflection of our assumption that the vertical and lateral degrees of freedom of the electron wave function are decoupled [61, 98, 101].

We now return to the integration over $\mathbf{q}$. The integration over θ_q can be done analytically, and depends on the interaction type, $\nu = \{$LA-DP, LA-PZ, TA-PZ$\}$. The matrix elements $|\widetilde{M}_\nu(\mathbf{q})|^2$ (see Eqs. (4.21), (4.22), and (4.23)) can be expressed in terms of the spherical coordinates in Eq. (4.46):

$$|\widetilde{M}_{LA-DP}(\mathbf{q})|^2 = \frac{\hbar D^2}{2\,d\,c_{LA}}|q_{LA}| \tag{4.50}$$

$$|\widetilde{M}_{LA-PZ}(\mathbf{q})|^2 = \frac{32\pi^2\hbar e^2 h_{14}^2}{\epsilon^2\,d\,c_{LA}}\left(\frac{9\cos^2\theta_q\sin^2\theta_q\sin^4\phi_q\cos^2\phi_q}{|q_{LA}|}\right), \tag{4.51}$$

$$|\widetilde{M}_{TA-PZ}(\mathbf{q})|^2 = \frac{32\pi^2\hbar e^2 h_{14}^2}{\epsilon^2\,d\,c_{TA}}\left(\frac{\cos^2\theta_q\sin^2\theta_q\sin^4\phi_q(1-9\cos^2\phi_q)+\sin^2\phi_q\cos^2\phi_q}{|q_{TA}|}\right). \tag{4.52}$$

The entire integration over $\mathbf{q}$ can be defined as

$$\begin{aligned}\mathbb{I}^{nm,\nu}_{ijkl} &\equiv \frac{1}{(2\pi\hbar)^2 c_\nu}\int d^3\mathbf{q}|\widetilde{M}_\nu(\mathbf{q})|^2\widetilde{\gamma}^{ij}_{\mathbf{q}}(\widetilde{\gamma}^{lk}_{\mathbf{q}})^*\delta(q-q_{nm,\nu})\\ &= \int_0^\pi d\phi_q\sin\phi_q\,\mathbb{I}^\nu_{\theta_q}(\phi_q)\,\mathbb{I}^{ij}_r(\phi_q)\,\mathbb{I}^{lk}_{r'}(\phi_q)\,\mathbb{I}_z(\phi_q)\,\mathbb{I}^*_{z'}(\phi_q),\end{aligned} \tag{4.53}$$

where,

$$\mathbb{I}^{\nu}_{\theta_q}(\phi_q) \equiv \frac{q^2_{nm,\nu}}{\hbar^2 c_\nu} \int_0^{2\pi} d\theta_q \, e^{-i(\widetilde{m}_{ij}-\widetilde{m}_{lk})(\theta_q-\pi/2)} |\widetilde{M}_\nu(\theta_q,\phi_q)|^2, \tag{4.54}$$

and we have used the delta function to evaluate the integration over q ($q \to q_{nm,\nu}$). For each of $\nu = \{\text{LA-DP, LA-PZ, TA-PZ}\}$, the $\mathbb{I}^{\nu}_{\theta_q}(\phi_q)$ integral evaluates to

$$\mathbb{I}^{\text{LA-DP}}_{\theta_q}(\phi_q) \equiv \frac{\pi D^2 |q_{nm,LA}|^3}{\hbar\, d\, c^2_{LA}} \delta_{\widetilde{m}_{ij}\widetilde{m}_{lk}}, \tag{4.55}$$

$$\mathbb{I}^{\text{LA-PZ}}_{\theta_q}(\phi_q) \equiv \frac{72\pi^3 e^2 h^2_{14} |q_{nm,LA}|}{\hbar\, \epsilon^2\, d\, c^2_{LA}} \sin^4\phi_q \cos^2\phi_q \delta_{\widetilde{m}_{ij}\widetilde{m}_{lk}}, \tag{4.56}$$

$$\mathbb{I}^{\text{TA-PZ}}_{\theta_q}(\phi_q) \equiv \frac{8\pi^3 e^2 h^2_{14} |q_{nm,TA}|}{\hbar\, \epsilon^2\, d\, c^2_{TA}} (8\sin^2\phi_q \cos^2\phi_q + \sin^4\phi_q(1-9\cos^2\phi_q))\delta_{\widetilde{m}_{ij}\widetilde{m}_{lk}}. \tag{4.57}$$

The remaining five integrals (over r, r', z, z', and ϕ_q) are performed numerically (see App. C).

4.4 Relaxation, Decoherence, and Dephasing

We are interested in how the QD system changes in time when coupled with an acoustic phonon reservoir. To quantitatively evaluate this evolution, we calculate the relaxation time and the decoherence time of the QD system.

Decoherence of a state can arise in one of two ways; from interactions with the bath in which, due to the exchange of energy, it evolves into another state, or from loss of phase coherence between the basis states in the superposition which makes up the eigenstate. In the former case, decoherence is due to relaxation, while in the latter case decoherence is due to dephasing. In general, decoherence can be due to both. We define the relaxation time, T_1, to be the time constant used for describing how quickly the energy of an excited system eigenstate is lost to the reservoir when it decays to a system eigenstate of lesser energy. We define the decoherence time, T_2, to be the time constant used for describing how quickly the coherence of the eigenstate is destroyed.

The relationship between these two time constants is given by [106–110]

$$\frac{1}{T_2} = \frac{1}{2T_1} + \frac{1}{T_\phi}, \tag{4.58}$$

where T_ϕ is the dephasing time constant. This imposes an upper bound on T_2, $T_2 \leqslant 2T_1$. In a "pure" dephasing process there is no energy dissipation in the system, and $T_2 = T_\phi$. That is to say that only elastic processes contribute to the decoherence of the state, and the state populations do not change. In general, elastic and inelastic processes contribute to decoherence.

Let us now consider the solution to the differential equation for the density matrix in Eq. (4.16a). It is convenient to express $\rho(t)_{m'm}$ as

$$\widetilde{\rho}(t)_{m'm} \equiv e^{-i\omega_{m'm}t}\rho(t)_{m'm}. \tag{4.59}$$

Equation (4.16a) becomes

$$\begin{aligned}\dot{\widetilde{\rho}}(t)_{m'm} &= \sum_{n'n}\bigl(-i\omega_{n'n}\delta_{n'm'}\delta_{nm} + R_{m'mn'n}\bigr)\widetilde{\rho}(t)_{n'n} \\ &= \sum_{n'n}\widetilde{R}_{m'mn'n}\widetilde{\rho}(t)_{n'n},\end{aligned} \tag{4.60}$$

where

$$\widetilde{R}_{m'mn'n} \equiv \bigl(-i\omega_{n'n}\delta_{n'm'}\delta_{nm} + R_{m'mn'n}\bigr). \tag{4.61}$$

In analogy with the vector equation

$$\dot{\boldsymbol{r}}(t) = A\,\boldsymbol{r}(t) \tag{4.62}$$

where A is a matrix of constant coefficients, we can treat the set of elements of $\widetilde{\boldsymbol{\rho}}(t)$ as a vector and the elements of $\widetilde{R}$ as a matrix. The solution to the homogeneous linear system in Eq. (4.62) with the substitution of $\widetilde{\boldsymbol{\rho}}(t)$ for $\boldsymbol{r}(t)$ and $\widetilde{R}$ for A is

$$\widetilde{\boldsymbol{\rho}}(t) = \sum_i c_i e^{\lambda_i t}\boldsymbol{u}_i, \tag{4.63}$$

where $\boldsymbol{u}_i$ are the eigenvectors of $\widetilde{R}$ and λ_i the corresponding eigenvalues [111]. The coefficients c_i are determined by initial conditions.

The relaxation time constant T_1 is related to the eigenvalues in the solutions for the diagonal elements of $\widetilde{\rho}(t)_{m'm}$ $(m' = m)$, while the decoherence time constant T_2 is related to the eigenvalues in the solutions for the off-diagonal elements of $\widetilde{\rho}(t)_{m'm}$ $(m' \neq m)$. The details of the expressions for T_1, T_2, and T_ϕ will be evaluated for the single-electron system, with and without SO, in Chap. 5, and for the three-electron interacting system, with and without SO, in Chap. 6.

Chapter 5

Phonon-Induced Decay of a Single-Electron State

In this chapter we examine the relaxation and decoherence rates of single-electron states in the QD system due to the phonon interactions introduced in Chap. 4. Section 5.1 examines the decay rates when the SO interaction is excluded from the model. Specifically, Sec. 5.1.1 explores the relaxation rates of the first excited state to the ground state as a function of confinement frequency ω_0, while Sec. 5.1.2 explores the relaxation rates of the first excited state to the ground state as a function of a magnetic field applied perpendicular to the plane of the QD, $B \equiv B_z$. In Sec. 5.2 we examine the decay rates when the SO interaction is included in the model as a perturbation to the QD system. To explain the results observed in our model, we analyze the decay rates obtained under the secular approximation in Sec. 5.2.1. Two different SO interaction strengths are considered. In Sec. 5.2.2 and Sec. 5.2.3 the relaxation rates and decoherence rates, respectively, are analyzed as a function of ω_0 when the SO effect is small. In Sec. 5.2.4 and Sec. 5.2.5 the relaxation rates and decoherence rates, respectively, are analyzed as a function of ω_0 when the SO effect is increased.

5.1 Decay of Single-Electron States in Absence of Spin-Orbit Interaction

For all cases investigated in this section the initial state of the system is the first excited state of the single-electron QD, the $L_z = -1$ p-shell, and the final state of the system is the ground state, the $L_z = 0$ s-shell. The electron-phonon interaction does not change the spin of the electron, therefore the results are independent of the electron-spin of the states used. Note that in the absence of an applied magnetic field the p-shell is actually doubly degenerate, one state with orbital angular momentum $L_z = -1$ and the other with orbital angular momentum $L_z = 1$. The orbital configuration of these states in the absence of an applied magnetic field is shown in Fig. 5.1.

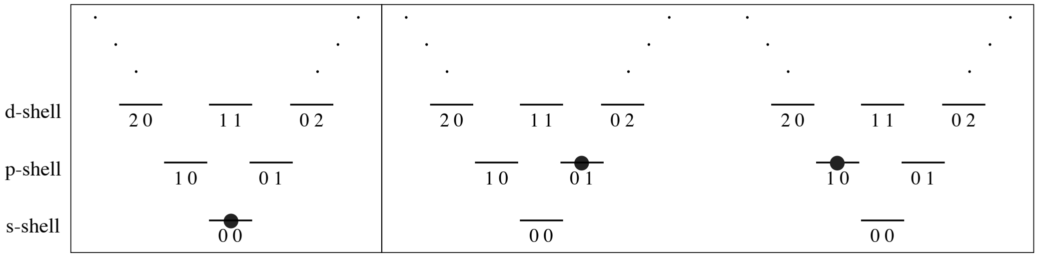

Figure 5.1: Orbital configuration of the ground state (left) and doubly degenerate first excited state (right) in the N=1 QD in the absence of an applied magnetic field. Each orbital is labeled by its orbital quantum numbers, n and m.

The decay rates for both shell states at $B = 0$ are identical [98]. This degeneracy is lifted as B is increased, leaving the $L_z = -1$ state as the sole first excited state. Therefore only the $L_z = -1$ initial state is considered in the results shown below.

The decay from the excited state to the ground state is a two-level system. The density matrix of a two-level system is, in general,

$$\rho = \begin{pmatrix} \rho_{00} & \rho_{01} \\ \rho_{10} & \rho_{11} \end{pmatrix} \tag{5.1}$$

where ρ_{01} and ρ_{10} are complex conjugates of each other. From Sec. 4.4, we wish to write the elements of our density matrix as a vector,

$$\widetilde{\boldsymbol{\rho}}(t) \rightarrow \begin{pmatrix} \widetilde{\rho}(t)_0 \\ \widetilde{\rho}(t)_1 \\ \widetilde{\rho}(t)_2 \\ \widetilde{\rho}(t)_3 \end{pmatrix} \equiv \begin{pmatrix} \widetilde{\rho}(t)_{00} \\ \widetilde{\rho}(t)_{01} \\ \widetilde{\rho}(t)_{10} \\ \widetilde{\rho}(t)_{11} \end{pmatrix}, \tag{5.2}$$

where each single index on the elements in the left column vector is in fact a double index representing an element of the density matrix $\widetilde{\boldsymbol{\rho}}(t)$ (see Eq. (4.59)). In a similar way, the elements of the Redfield tensor can be expressed in matrix form as

$$\widetilde{R} \rightarrow \begin{pmatrix} \widetilde{R}_{00} & \widetilde{R}_{01} & \widetilde{R}_{02} & \widetilde{R}_{03} \\ \widetilde{R}_{10} & \widetilde{R}_{11} & \widetilde{R}_{12} & \widetilde{R}_{13} \\ \widetilde{R}_{20} & \widetilde{R}_{21} & \widetilde{R}_{22} & \widetilde{R}_{23} \\ \widetilde{R}_{30} & \widetilde{R}_{31} & \widetilde{R}_{32} & \widetilde{R}_{33} \end{pmatrix} \equiv \begin{pmatrix} \widetilde{R}_{0000} & \widetilde{R}_{0001} & \widetilde{R}_{0010} & \widetilde{R}_{0011} \\ \widetilde{R}_{0100} & \widetilde{R}_{0101} & \widetilde{R}_{0110} & \widetilde{R}_{0111} \\ \widetilde{R}_{1000} & \widetilde{R}_{1001} & \widetilde{R}_{1010} & \widetilde{R}_{1011} \\ \widetilde{R}_{1100} & \widetilde{R}_{1101} & \widetilde{R}_{1110} & \widetilde{R}_{1111} \end{pmatrix}, \tag{5.3}$$

where, like above, each pair of indices in the left matrix represents the four indices required to specify a Redfield tensor element.

For the two-level systems investigated in this dissertation, we have found that $\widetilde{R}$ has the general form

$$\widetilde{R} = \begin{pmatrix} 0 & 0 & 0 & 2\Gamma^+_{1001} \\ 0 & -\Gamma^+_{1001} + i\omega_{10} & 0 & 0 \\ 0 & 0 & -\Gamma^+_{1001} - i\omega_{10} & 0 \\ 0 & 0 & 0 & -2\Gamma^+_{1001} \end{pmatrix}, \tag{5.4}$$

where $\Gamma^+_{nmm'n'}$ is defined in Eqs. (4.15a), (4.39), and (4.45a). In the above matrix $\omega_{10} = (E_1 - E_0)/\hbar$, where E_0 and E_1 are the energy eigenvalues of the ground state and the first excited state, respectively. The matrix in Eq. (5.4) can be diagonalized to obtain the following eigenvectors and eigenvalues:

$$\lambda_0 = 0,\ \boldsymbol{u}_0 = [1, 0, 0, 0]^{\mathrm{T}}, \tag{5.5a}$$

$$\lambda_1 = \left(-\Gamma^+_{1001} + i\omega_{10}\right),\ \boldsymbol{u}_1 = [0, 1, 0, 0]^{\mathrm{T}}, \tag{5.5b}$$

$$\lambda_2 = \left(-\Gamma^+_{1001} - i\omega_{10}\right),\ \boldsymbol{u}_2 = [0, 0, 1, 0]^{\mathrm{T}}, \tag{5.5c}$$

$$\lambda_3 = -2\Gamma^+_{1001},\ \boldsymbol{u}_3 = \frac{1}{\sqrt{2}}[-1, 0, 0, 1]^{\mathrm{T}}. \tag{5.5d}$$

From Eqs. (4.59), (4.63), and (5.5) the elements of $\rho(t)$, the density matrix for the QD system in the interaction picture, for this two-level system are:

$$\rho_{00}(t) = 1 + \tilde{c_1} e^{-2\Gamma^+_{1001} t}, \tag{5.6a}$$

$$\rho_{01}(t) = \tilde{c_2} e^{-\Gamma^+_{1001} t}, \tag{5.6b}$$

$$\rho_{10}(t) = \rho_{01}(t)^*, \tag{5.6c}$$

$$\rho_{11}(t) = -\tilde{c_1} e^{-2\Gamma^+_{1001} t}, \tag{5.6d}$$

where the coefficients $\tilde{c}_i$ are fixed by initial conditions.

The transition between the excited state and the ground state of the QD is described by the evolution of the diagonal elements of $\rho(t)$. Each diagonal element undergoes exponential decay, where the constant in the exponential term of each element is the relaxation rate. In this two-level system, the characteristic relaxation time is

$$T_1 = 1/(2\Gamma^+_{1001}). \tag{5.7}$$

The evolution of the off-diagonal elements describes the loss of coherence of the two-level system. In this case the decoherence time is

$$T_2 = 1/\Gamma^{+}_{1001}. \tag{5.8}$$

Since $T_2 = 2T_1$, we have from Eq. (4.58) that the dephasing rate is zero, meaning that the decoherence in the system is due exclusively to the relaxation from the excited state to the ground state. The decoherence rates would be affected by electron-phonon scattering, however this is not included in our model. The Master equation developed in Sec. 4.1 is valid only to second order in the interaction V. Higher order terms in the Liouville expansion of Eq. (4.4) are necessary to account for scattering events.

5.1.1 Decay Rates as a Function of Confinement Frequency

Here we present a study of the decay rates, the inverse of the characteristic decay times described above, of the single-electron state as a function of ω_0 at constant B. Since the decoherence rate is simply half of the relaxation rate, we show results only for the relaxation rate in this section. We examine the system at $B = 0$, $B = 1$ T, $B = 5$ T, and $B = 10$ T.

In the absence of an applied magnetic field, the energies of the single-electron states are directly proportional to ω_0 (see Eq. (2.4)). The energy spectrum of the lowest lying states for the single-electron QD system at $B = 0$ is shown in Fig. 5.2. As mentioned previously, the s-shell is non-degenerate (excluding spin) with an orbital angular moment of $L_z = 0$. The p-shell is the first excited state, and is doubly degenerate with two states of orbital angular momentum $L_z = \pm 1$. The degeneracy of each subsequent shell in the single-electron QD at zero magnetic field increases by one. (As B increases from zero this degeneracy lifts.)

Figure 5.3 shows the relaxation rate ($1/T_1$) from the initial $L_z = -1$ excited state to the final $L_z = 0$ ground state. These results are very similar to those derived numerically in Refs. [100, 101], and at their peak are of the same order of magnitude of the relaxation rates found experimentally in Refs. [18,29,30]. For small values of ω_0 ($\omega_0 < 0.4$ meV$/\hbar$), the relaxation rate is dominated by the piezoelectric effect. As ω_0 increases, the influence of the piezoelectric effect on the relaxation rate diminishes, and the relaxation rate is due almost exclusively to the deformation

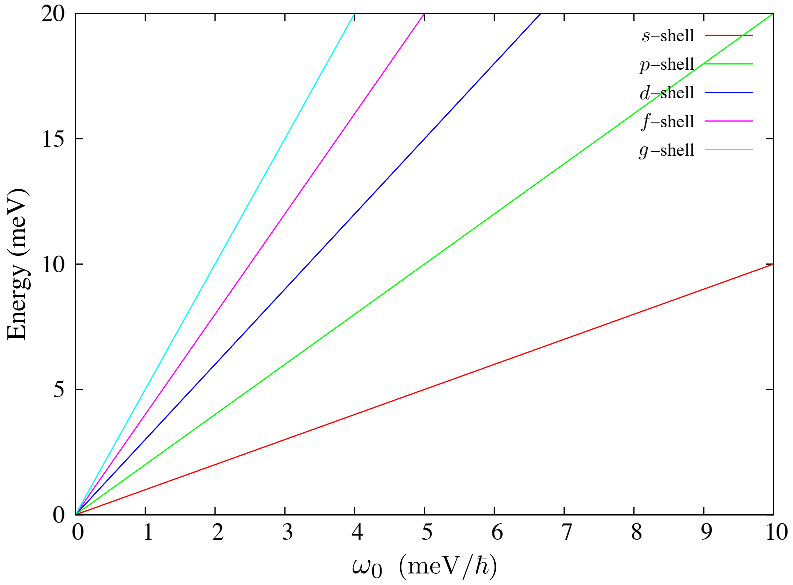

Figure 5.2: Energy spectrum of the lowest-lying single-electron states a function of confinement frequency $\hbar\omega_0$ at zero magnetic field. Note the degeneracy of each subsequent shell from the s-shell increases by one.

potential. This can be explained in the following manner: The relaxation rate varies with the square of the electron-phonon matrix element for each interaction, $|M_\nu(\mathbf{q})|^2$. For the deformation potential, the square of the matrix element is proportional to $|\mathbf{q}|$ (see Eq. (4.21)), whereas for the piezoelectric effect, it is proportional to $1/|\mathbf{q}|$ (see Eqs. (4.22) and (4.23)). When $B = 0$ the magnitude of $|\mathbf{q}|$ is directly proportional to ω_0 since the energy of the emitted phonon ($E_{ph} = \hbar\omega_q = \hbar c_\nu q$) is equal to the energy difference between the excited state and the ground state in the QD ($\Delta E = \hbar\omega_0$). This means that the deformation potential will be the governing scattering mechanism when the phonons emitted by the QD system are greater in energy, and the piezoelectric effect will be the governing scattering mechanism when the emitted phonons are lower in energy. Since the energy scale of the QD grows with ω_0, the relaxation rate is dominated by the piezoelectric effect at lower values of ω_0 and by the deformation potential at higher values of ω_0. In all cases studied in this chapter, the relaxation rate due to the TA-PZ interaction has a larger peak than that of the LA-PZ interaction. This result has been reported in the literature [100].

For both interaction mechanisms the relaxation rates tend to zero as ω_0 tends to zero, due to the depletion of the density of phonon states as the energy of the emitted

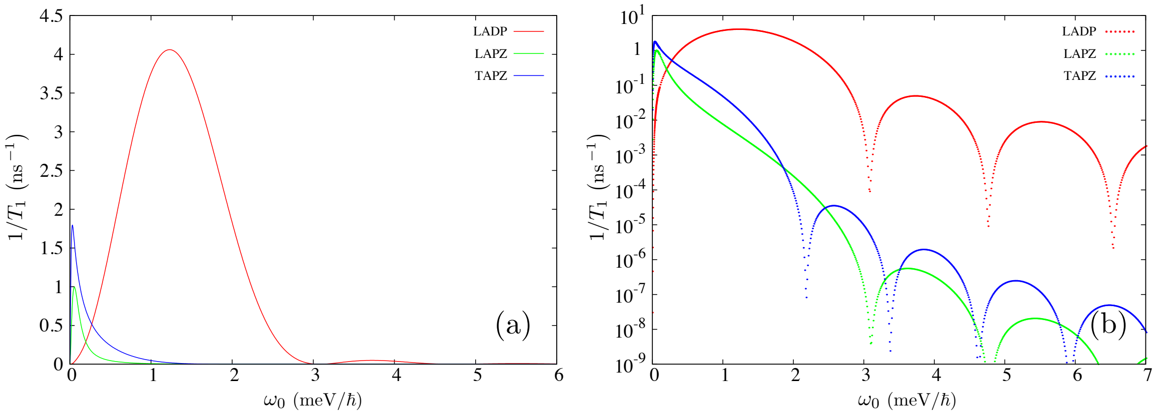

Figure 5.3: Relaxation rates in a single-electron QD system from the initial $L_z = -1$ state to the final $L_z = 0$ state as a function of confinement frequency ω_0 at zero magnetic field. The relaxation rate via emission of (i) a LA-DP phonon is shown in red, (ii) a LA-PZ phonon is shown in green, and (iii) a TA-PZ phonon is shown in blue. The right-hand graph shows the data in the left-hand graph as plotted on a log scale, revealing well-defined minima in the relaxation time.

phonon approaches zero. The relaxation rates for both interaction mechanisms approach zero as ω_0 becomes large, as well. As pointed out in Sec. 4.3, the vertical and lateral contributions to the electron-phonon interaction decouple. As the magnitude of the phonon momentum grows with increasing ω_0, the vertical contribution decays rapidly to zero. This coincides with the phonon-wavelength being less than ℓ_z, the width of the quantum well, in this case the smallest confinement length of the electron wave function. This result points out that the electron-phonon interaction is weak when the phonon wavelength is small compared to that of the electron wave function along a certain direction [98].

Another feature present in the relaxation rate is its oscillatory nature, made clear in the log plot of Fig. 5.3 (b). At certain values of ω_0 phonon emission from the QD is greatly suppressed. The peaks correspond to when the wave function of the emitted phonon provides a maximum overlap between the (orthogonal) initial and final states of the electron in the QD. As the energy, and hence the wavelength, of the emitted phonon is varied with ω_0, the phonon wave function changes and allows for alternating minimum and maximum overlap between the electron states [61,100,101]. The maxima and minima occur at different values of ω_0 depending on the polarization mode of the emitted phonon (LA or TA). This is because the sound velocity is different

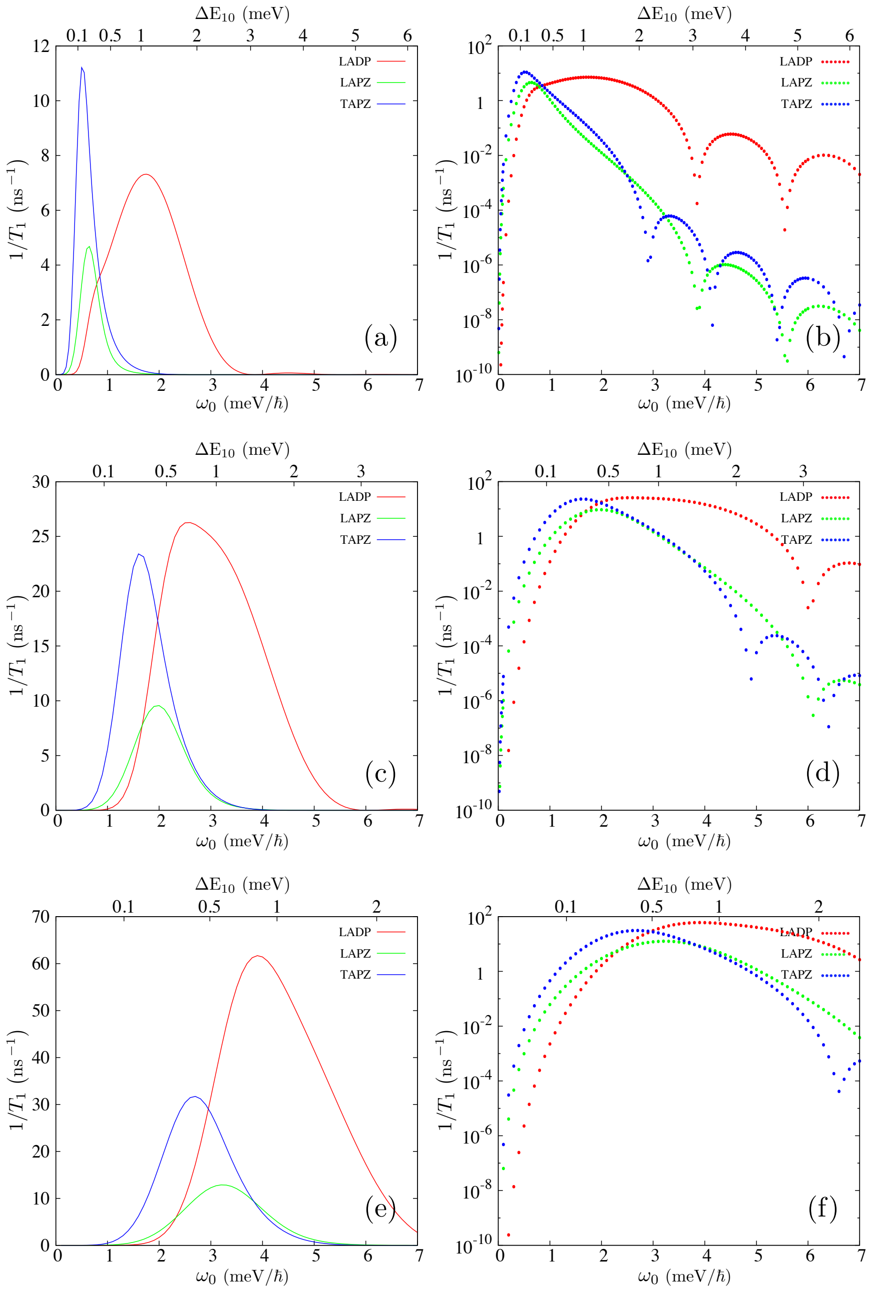

Figure 5.4: Relaxation rates from the initial $L_z = -1$ state to the final $L_z = 0$ state as a function of confinement frequency $\hbar\omega_0$ at a constant magnetic field of $B = 1$ T (panels (a) and (b)), $B = 5$ T (panels (c) and (d)), and $B = 10$ T (panels (e) and (f)). The upper x-axis in each plot shows the energy difference between the first excited state and the ground state for the single-electron QD.

for each mode, and corresponds to different phonon wavelengths for the same value of ω_0. These maxima and minima correspond to the maxima and minima in the vertical contribution function.

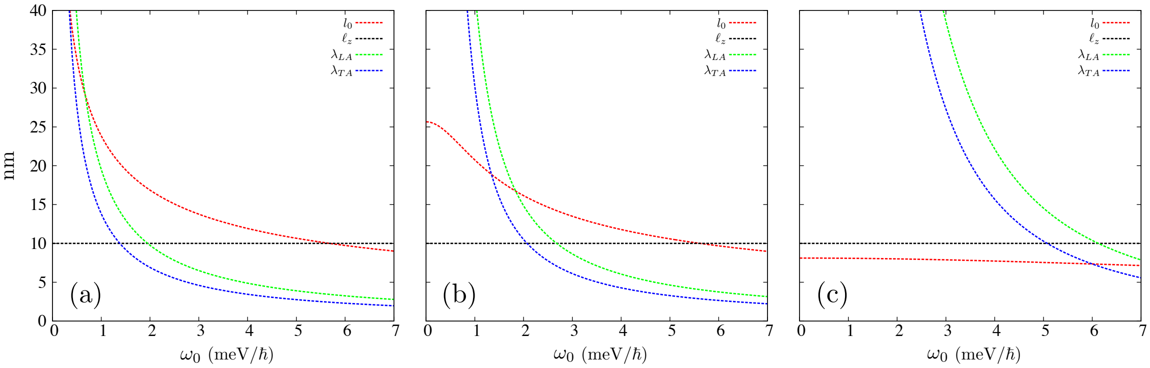

Figure 5.5: Wavelength dependence on confinement frequency ω_0 at a constant magnetic field $B = 0$ (a), $B = 1$ T (b), and $B = 10$ T (c). The lateral effective length of the electron wave function, l_0, (shown in red) decreases with increasing ω_0 and increasing B. As B increases, the phonon wavelength for each polarization mode, λ_{LA} (shown in green) and λ_{TA} (shown in blue), becomes greater than l_0 for an increasing range of ω_0. However, for large enough values of ω_0 the phonon wavelengths become smaller than the width of the quantum well, ℓ_z (shown in black).

We next look at the relaxation rates as B grows to 1 T, 5 T and 10 T. These results are shown in Fig. 5.4. In general, as B increases, the energy difference between the ground state and first excited state decreases. This means that the energy of the emitted phonon gets smaller, and therefore the contribution to the relaxation rate by the PZ interaction grows. In addition, as B increases, the electron wave functions become more localized. While l_0, the lateral effective length of the electron wave function, shrinks, the phonon wavelength λ_q grows for both phonon modes. Furthermore, λ_q becomes greater than l_0 for an increasing range of ω_0 with increasing B. This behaviour is shown in Fig. 5.5. In keeping with the above statement that the electron-phonon interaction is weak when the phonon wavelength is smaller than that of the electron wave function, the relaxation rate increases as λ_q becomes greater than l_0. Despite growing with B, λ_q still shrinks with increasing ω_0 as before. For each increasing value of B shown, the relaxation rate is suppressed at a greater value of ω_0, when λ_q finally becomes smaller than ℓ_z, the width of the quantum well.

Another consequence of increasing B is that the width of the peaks broaden over a greater range of ω_0. This is due to the initially slower rate of energy change between the electron states as a function of ω_0 for increasing B, as displayed in Fig. 5.6. Note that, as the energy of the emitted phonon shifts with ω_0, so do the peak locations for each interaction in the relaxation rates, coinciding approximately with the same

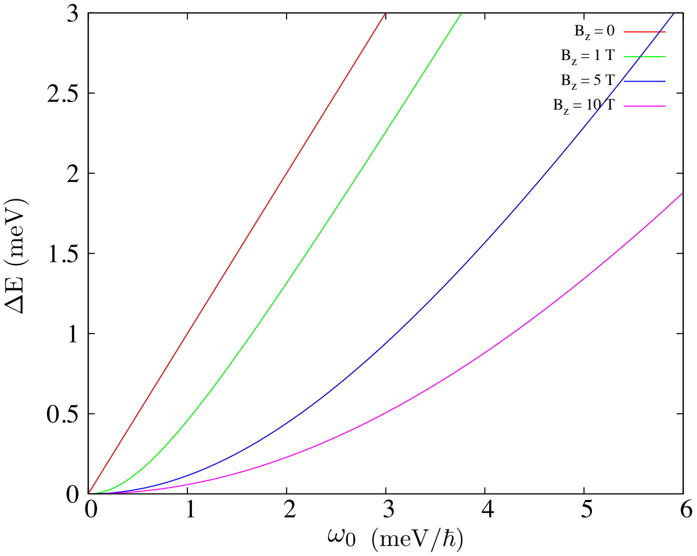

Figure 5.6: Energy difference between the single-electron ground state and first excited state in the QD as a function of ω_0 for constant magnetic fields of $B = 0$, $B = 1$ T, $B = 5$ T, and $B = 10$ T.

phonon energy for each value of B. The oscillations observed at $B = 0$ (see Fig. 5.3 (b)) are still present at large ω_0 for the finite fields investigated here, as seen in Figs. 5.4 (b), (d), and (f). The results displayed in Fig. 5.4 are consistent with those published in Ref. [100].

5.1.2 Decay Rates as a Function of Magnetic Field

We next examine the relaxation rates as a function of B at constant ω_0. Specifically we look at when $\omega_0 = 1$ meV/$\hbar$, 2 meV/$\hbar$, and 3 meV/$\hbar$. These results are shown in Fig. 5.7. As mentioned in the previous section, as B increases the energy difference between the ground state and the first excited state in the QD decreases, as is displayed on the top axes of the plots in Fig. 5.7. Consequently, the PZ interaction dominates the relaxation rate for the majority of the B-field range examined for each value of ω_0. Consistent with the results shown in Fig. 5.4 is the fact that, in general, the peaks in the relaxation rates grow in magnitude and shift to larger values of B with increasing ω_0 to accommodate the changes in energy of the emitted phonon.

The limiting behaviour of the relaxation rate as a function of B is reversed from that as a function of ω_0. In this case, since the energy of the emitted phonon decreases as B increases, the phonon density of states is depleted with increasing B, and phonon

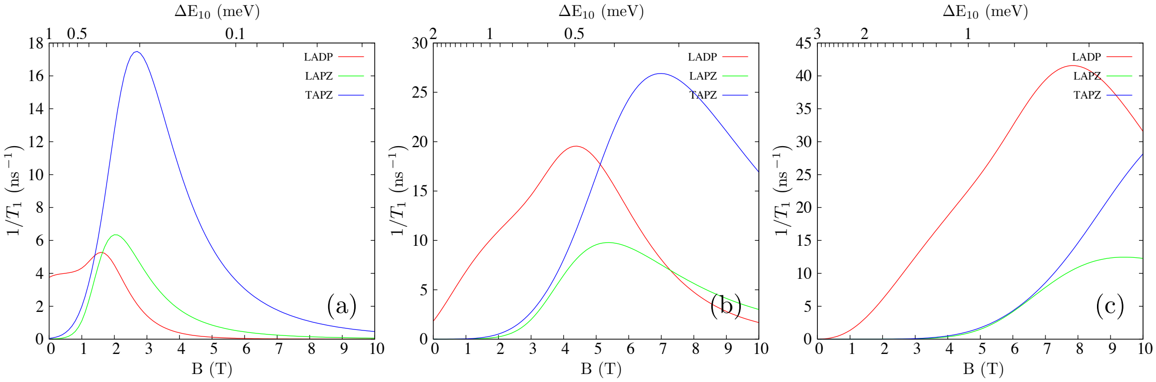

Figure 5.7: Relaxation rates from the initial $L_z = -1$ state to the final $L_z = 0$ state as a function of magnetic field B at a constant confinement frequency $\omega_0 = 1$ meV/$\hbar$ (a), $\omega_0 = 2$ meV/$\hbar$ (b), and $\omega_0 = 3$ meV/$\hbar$ (c). The upper x-axis in each plot shows the energy difference between the first excited state and the ground state for the single-electron QD.

emission becomes suppressed. On the other end, as B approaches zero, the relaxation rates do not necessarily go to zero; it depends on the value of ω_0. When ω_0 is small ($\lesssim 2$ meV/$\hbar$), λ_q for one or both types of polarization modes is greater than the smallest confinement length of the electron wave function at small B (see Fig. 5.8), in this case ℓ_z, and so the electron-phonon interaction is still effectual. However, as ω_0 increases, λ_q becomes less than ℓ_z and the electron-phonon interaction weakens at small B, as is seen in Fig. 5.7 (c) when $\omega_0 = 3$ meV/$\hbar$.

Unlike in the previously examined cases of varying ω_0 at constant B, oscillations in the relaxation rate are not always seen as B is varied at constant ω_0. As previously mentioned, the oscillations coincide with those present in the vertical component of the electron-phonon interaction. The minima occur only for values of λ_q that are smaller than ℓ_z. When $\omega_0 < 2$ meV/$\hbar$, $\lambda_q \gtrsim \ell_z$ for all values of $B \geqslant 0$, and therefore no oscillations are present in the relaxation rate. When $\omega_0 = 2$ meV/$\hbar$ a sharp minimum appears in the TA-PZ relaxation rate at $B = 0$, and when $\omega_0 = 3$ meV/$\hbar$ a sharp minimum appears in the LA relaxation rates at $B = 0$ and in the TA-PZ relaxation rate at $B = 1.1$ T (not shown). Generally speaking, since λ_q increases with increasing B, the oscillatory behaviour appears before the main peaks in the relaxation rate (when B is small, provided $\lambda_q < \ell_z$) and should not occur after the main relaxation rate peaks (when B is large). These results are consistent with those published in Ref. [100].

Clearly the relaxation rate of the electron in a QD can be tuned via both the confinement frequency and an applied external magnetic field. By using key values for each ω_0 and B the lifetime of the QD state can be increased by a few orders of magnitude.

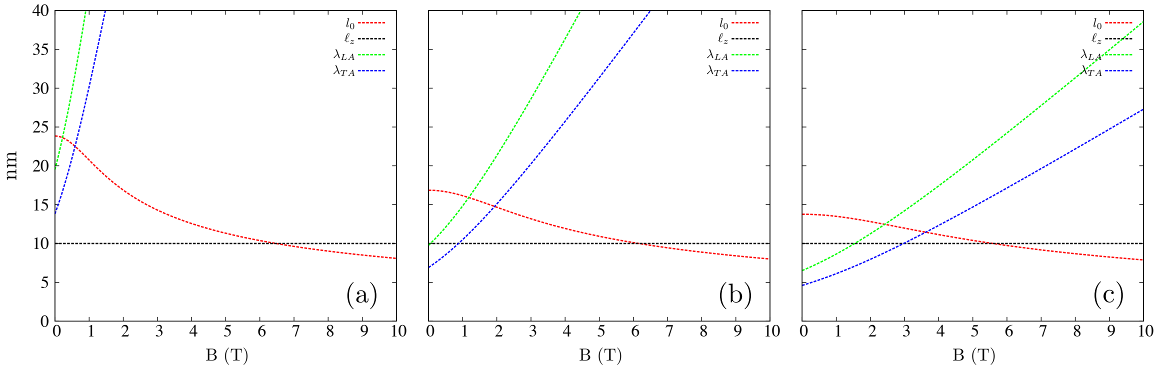

Figure 5.8: Wavelength dependence on magnetic field B at a constant confinement frequency $\omega_0 = 1$ meV/$\hbar$ (a), $\omega_0 = 2$ meV/$\hbar$ (b), and $\omega_0 = 3$ meV/$\hbar$ (c). In general, the wavelength of an emitted increases with increasing magnetic field, but decreases with increasing confinement frequency of the QD due to the phonon's increasing energy. When $\omega_0 = 3$ meV/$\hbar$, λ_q for both phonon modes is less than ℓ_z for small B.

5.2 Decay of Single-Electron States in Presence of Spin-Orbit Interaction

We next examine the effects on relaxation and decoherence rates when the SO interaction is considered in the single-electron QD. The spin of the electron becomes relevant in this case since the SO interaction mixes spin states. Since we are interested in SO effects in the lowest-lying QD states, we restrict ourselves to truncated subspaces which contain only four states for the majority of the system parameters investigated. To this extent, our model weakens as both B and ω_0 approach zero, where multiple degeneracies can occur in the ground state and first excited state of the SP spectrum.

In this section we investigate the relaxation and decoherence rates as a function of ω_0 for a constant magnetic field of $B = 1$ T. We use the following four H_{QD} eigenstates in our truncated subspace as they make up the four lowest-lying states in the SP spectrum for the majority of the B and ω_0 values investigated:

$$\begin{aligned}
|0\rangle &\equiv |L_z\!=\!0,\;\; S_z\!=\!1/2\rangle \equiv |0\,0\uparrow\rangle\,, \\
|1\rangle &\equiv |L_z\!=\!0,\;\; S_z\!=\!-1/2\rangle \equiv |0\,0\downarrow\rangle\,, \\
|2\rangle &\equiv |L_z\!=\!-1,\;\; S_z\!=\!1/2\rangle \equiv |0\,1\uparrow\rangle\,, \\
|3\rangle &\equiv |L_z\!=\!-1,\;\; S_z\!=\!-1/2\rangle \equiv |0\,1\downarrow\rangle\,,
\end{aligned} \tag{5.9}$$

where the rightmost states in the above equation are expressed using the SP orbital numbers, $|n, m, s\rangle$. Note that this particular subspace contains the proper criteria for creating the four orthogonal meron states described in Sec. 3.3, namely that each of the four meron states will be a superposition of two of the above QD states where $|L_z| \neq |L'_z|$ and $|S_z - S'_z| = 1$. Some of the lowest-lying energies in the SP QD are shown as a function of ω_0 in Fig. 5.9 for $B = 1$ T. Note that the four states listed in Eq. (5.9) do not make up the four lowest-lying states until $\omega_0 > 0.3$ meV/$\hbar$. Those states which make up the four lowest-lying states for ω_0 less than the stated threshold value do not satisfy the necessary conditions to create the four orthogonal meron states discussed above. In our model we retain the four states in Eq. (5.9) for all calculations and present results for values of ω_0 that are greater than this threshold value of ω_0.

The total Hamiltonian is $H = H_{QD} + H_{SO}$, where H_{QD} is described in Eq. (2.2a) and H_{SO} is described in Eq. (3.14). We diagonalize H in the subspace containing the four states in Eq. (5.9). Details of this calculation can be found in App. B.2. The energy eigenvalues of the resulting states, henceforth referred to as SO states, are

$$E_0 = \frac{1}{2}\left(e_0 + e_3 - \sqrt{(e_0 - e_3)^2 + 4\beta_D^2\,\mathcal{E}_-^2}\right), \tag{5.10a}$$

$$E_1 = \frac{1}{2}\left(e_1 + e_2 - \sqrt{(e_1 - e_2)^2 + 4\alpha_R^2\,\mathcal{E}_+^2}\right), \tag{5.10b}$$

$$E_2 = \frac{1}{2}\left(e_1 + e_2 + \sqrt{(e_1 - e_2)^2 + 4\alpha_R^2\,\mathcal{E}_+^2}\right), \tag{5.10c}$$

$$E_3 = \frac{1}{2}\left(e_0 + e_3 + \sqrt{(e_0 - e_3)^2 + 4\beta_D^2\,\mathcal{E}_-^2}\right), \tag{5.10d}$$

where e_i is the energy of the H_{QD} eigenstate $|i\rangle$, and $\mathcal{E}_\pm$ are defined in Eq. (3.17) by

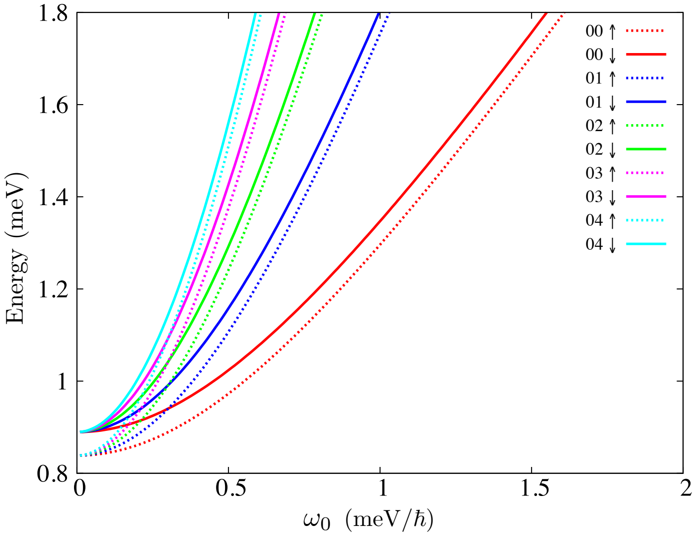

Figure 5.9: Lowest-lying energy spectra in the single-electron QD as a function of confinement frequency ω_0 at a constant magnetic field of $B = 1$. The states are labelled by their SP orbital numbers. The level crossings at smaller values of ω_0 are due to Zeeman splitting.

taking $L_z = 0$. The corresponding SO states are

$$|\psi_0\rangle = a\,|0\rangle - ib\,|3\rangle, \tag{5.11a}$$

$$|\psi_1\rangle = c\,|1\rangle - d\,|2\rangle, \tag{5.11b}$$

$$|\psi_2\rangle = d\,|1\rangle + c\,|2\rangle, \tag{5.11c}$$

$$|\psi_3\rangle = b\,|0\rangle + ia\,|3\rangle, \tag{5.11d}$$

where

$$a \equiv \frac{-(E_0 - e_3)}{\sqrt{\beta_D^2\,\mathcal{E}_-^2 + (E_0 - e_3)^2}}, \tag{5.12a}$$

$$b \equiv \frac{\beta_D\,\mathcal{E}_-}{\sqrt{\beta_D^2\,\mathcal{E}_-^2 + (E_0 - e_3)^2}}, \tag{5.12b}$$

$$c \equiv \frac{-(E_1 - e_2)}{\sqrt{\alpha_R^2\,\mathcal{E}_+^2 + (E_1 - e_2)^2}}, \tag{5.12c}$$

$$d \equiv \frac{\alpha_R\,\mathcal{E}_+}{\sqrt{\alpha_R^2\,\mathcal{E}_+^2 + (E_1 - e_2)^2}}. \tag{5.12d}$$

Note that in the event of a four-fold degeneracy between the H_{QD} eigenstates in Eq. (5.9), the four SO states in Eq. (5.11) reduce exactly to the meron states described in Eq. (3.8)[1].

---

[1] Eq. (3.8) describes a general winding state, but with $|L_z| \neq |L_z'|$ it describes a meron state.

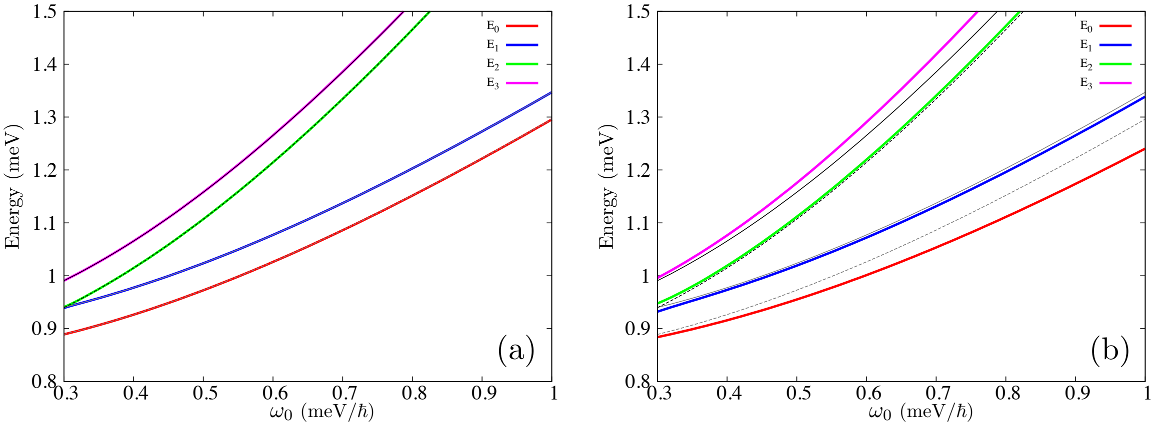

Figure 5.10: Energy spectrum of the four SO states (see Eq. (5.10)) as a function of ω_0 with (a) $\alpha_R = 1$ meV·nm and $\beta_D = 3$ meV·nm at $B = 1$ T, and (b) $\alpha_R = 10$ meV·nm and $\beta_D = 30$ meV·nm at $B = 1$ T. The grey and black lines are the energy eigenvalues of the four H_{QD} states in Eq. (5.9), where the dashed lines are the two spin-up states (e_0 and e_2) and the solid lines are the two spin-down states (e_1 and e_3). The degeneracy between E_1 and E_2 at $\omega_0 = 0.3$ meV/$\hbar$ is lifted as the strength of the SO interaction is increased.

In the following calculations we consider two sets of values for the SO parameters α_R and β_D. The first set is close to expected values for GaAs and the second set is made to be an order of magnitude larger to further illustrate the trends induced by including SO interaction in the QD. Specifically, in Sec. 5.2.2 and Sec. 5.2.3 we calculate the relaxation and decoherence rates, respectively, for $\alpha_R = 1$ meV·nm [58, 76, 91, 112] and $\beta_D = 3$ meV·nm [79, 88, 113–115], then repeat the calculations in Sec. 5.2.4 and Sec. 5.2.5 for $\alpha_R = 10$ meV·nm and $\beta_D = 30$ meV·nm. By taking $\beta_D > \alpha_R$, the SO energy eigenvalues are ordered by increasing magnitude as $E_0 < E_1 < E_2 < E_3$ (see Fig. 3.3).

The SO energies are plotted in Fig. 5.10 as a function of ω_0 for both sets of α_R and β_D at $B = 1$ T, while the modulus-squared of coefficients of the SO states are plotted in Fig. 5.11. For small SO interaction ($\alpha_R = 1$ meV·nm, $\beta_D = 3$ meV·nm), the four SO energies are nearly degenerate with the four H_{QD} state energies (indicated by the black and grey lines) for the entire range of ω_0 investigated. This is because, for this small SO strength, the SO states in Eq. (5.11) are almost exclusively (to within 99%) made up of only one H_{QD} state. Specifically, when $\omega_0 > 0.3$ meV/$\hbar$, $|\psi_0\rangle \approx |0\rangle$, $|\psi_1\rangle \approx |1\rangle$, $|\psi_2\rangle \approx |2\rangle$, and $|\psi_3\rangle \approx |3\rangle$. This is shown in Fig. 5.11 (a), where, except near the threshold value of $\omega_0 = 0.3$ meV/$\hbar$, the coefficients b and d are zero. As

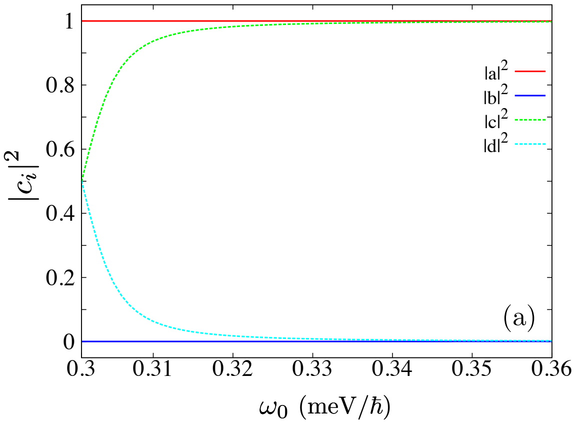

Figure 5.11: Modulus-squared values of the coefficients of the SO states in Eq. 5.11 at $B = 1$ T when $\alpha_R = 1$ meV·nm and $\beta_D = 3$ meV·nm (a), and when $\alpha_R = 10$ meV·nm and $\beta_D = 30$ meV·nm (b). The degree of basis state mixing in the SO states increases with the strength of the SO interaction.

ω_0 approaches 0.3 meV/$\hbar$, the states $|\psi_1\rangle$ and $|\psi_2\rangle$ become an equal superposition of $|1\rangle$ and $|2\rangle$. This transition coincides with the level crossing between the energies of states $|1\rangle$ and $|2\rangle$ as seen in Fig. 5.9. The states $|\psi_1\rangle$ and $|\psi_2\rangle$ become degenerate at this threshold value of ω_0.

When the SO interaction strength is increased to $\alpha_R = 10$ meV·nm and $\beta_D = 30$ meV·nm the degree of mixing between the H_{QD} states increases. This is manifested in Fig. 5.10 (b), where the SO energies diverge from the H_{QD} energies. The SO states are still dominated by a single H_{QD} basis state as when the SO strength was small, however for $|\psi_1\rangle$ and $|\psi_2\rangle$ the non-dominant basis state makes up as much as $\sim 3\%$ of the eigenstate when $\omega_0 > 0.3$ meV/$\hbar$, and for $|\psi_0\rangle$ and $|\psi_3\rangle$ the non-dominant basis state makes up as much as $\sim 10\%$ of the eigenstate. This can be seen in Fig. 5.11 (b), where the modulus-squared of each coefficient is plotted as a function of ω_0. For the larger SO strength, the degeneracy between states $|\psi_1\rangle$ and $|\psi_2\rangle$ near the threshold value of ω_0 is lifted, as seen in Fig. 5.10 (b). Additionally, the energies E_0 and E_3 split further from their unperturbed energies than do E_1 and E_2. This is due to the fact that E_0 and E_3 scale with β_D while E_1 and E_2 scale with α_R (see Eq. (5.10)), and we have taken β_D to be greater than α_R.

In the following sections we examine both the relaxation and decoherence rates of the SO states for the two different SO interaction strengths discussed above. As in the non-SO case, these decay rates are obtained by diagonalizing the Redfield tensor. In this four-level system the Redfield tensor is represented by a 16 x 16 matrix. As such the 16 eigenvalues are obtained numerically using the Eigen C++ library [116]. The relaxation rates correspond to the evolution of the diagonal elements of ρ. Therefore they are the eigenvalues of the Redfield tensor whose imaginary components are zero, since ρ is Hermitian. There are four diagonal elements of ρ in this model. One of the corresponding eigenvalues is exactly zero, however three are not. There must therefore be three different relaxation rates in the SO system, and not simply one as found in the non-SO system. In the non-SO system there can only be relaxation from the single excited state; in the SO system there are three excited states from which the system can relax. The decoherence rates are the real parts of the remaining eigenvalues of the Redfield tensor. The imaginary parts of these eigenvalues are non-zero and represent oscillatory behaviour. Because the off-diagonal elements of ρ are complex conjugates of each other, there should be a total of six unique decoherence rates in the four-level SO system. Due to the fact that, for both sets of SO parameters investigated, the SO states are predominantly of a single H_{QD} state like those investigated in Sec. 5.1, we expect the decay rates to remain primarily the same as those shown when SO is not included in the model.

5.2.1 Relaxation Rates under the Secular Approximation

In analyzing the relaxation rates of the system, it is useful to first examine the analytically derived relaxation rates obtained under the secular approximation. In the secular approximation the diagonal elements of ρ can be obtained from the Pauli Master Equation (see Ref. [97] for details). In this case, they are found to be

$$\rho_{00}(t) = \tilde{c_0} + \tilde{c_1} e^{-(W_{03}+W_{13}+W_{23})t} + \tilde{c_2} e^{-(W_{02}+W_{12})t} + \tilde{c_3} e^{-(W_{01})t}, \tag{5.13a}$$

$$\rho_{11}(t) = \tilde{c_4} e^{-(W_{03}+W_{13}+W_{23})t} + \tilde{c_5} e^{-(W_{02}+W_{12})t} + \tilde{c_6} e^{-(W_{01})t}, \tag{5.13b}$$

$$\rho_{22}(t) = \tilde{c_7} e^{-(W_{03}+W_{13}+W_{23})t} + \tilde{c_8} e^{-(W_{02}+W_{12})t}, \tag{5.13c}$$

$$\rho_{33}(t) = \tilde{c_9} e^{-(W_{03}+W_{13}+W_{23})t}, \tag{5.13d}$$

where W_{mn} is the transition rate from the SO state $|\psi_n\rangle$ to the SO state $|\psi_m\rangle$ as obtained using Fermi's Golden Rule.

In our model the transition rates W_{02} and W_{13} are equal to each other for the following two reasons: The change in orbital configuration from state $|\psi_2\rangle$ to state

$|\psi_0\rangle$ as described by W_{02} is identical to the change in orbital configuration from state $|\psi_3\rangle$ to state $|\psi_1\rangle$ as described by W_{13}, and the difference in energies between the corresponding states involved in each transition are equal to each other. W_{02} and W_{13} are expected to closely resemble the relaxation rate in the non-SO case as they each describe the transition between initial and final SO states that are predominantly the same as the initial and final states in the non-SO case. Since these initial and final SO states are also predominantly the same spin-species (recall that the electron-phonon interaction does not flip spins), the transition rates W_{02} and W_{13} will be the largest of the six found in Eq. (5.13). The remaining four transition rates, W_{01}, W_{03}, W_{12}, and W_{23} involve transitions between states that are primarily composed of opposite spin species. These transition rates will be smaller than W_{02} and W_{13} as these decay channels are less likely to be used since the electron-phonon interaction conserves spin. Just as we expect W_{02} and W_{13} to adhere to the behaviour seen in the relaxation rates in the non-SO case, W_{03} and W_{12} are expected to vary in a similar manner, albeit with a much smaller rate. This is because, like for W_{02} and W_{13}, the states involved in the respective transitions are predominantly of different orbital configurations, just like those in the non-SO case. On the other hand the rates W_{01} and W_{23}, which are also equal to each other for the same reasons as why $W_{02} = W_{13}$, should not vary much as a function of ω_0 since the SO states involved in the respective transitions primarily share the same orbital configuration and remain largely unchanged as ω_0 is varied.

In the secular approximation there are three different relaxation rates,

$$\tau_1 = W_{01}, \tag{5.14a}$$

$$\tau_2 = (W_{02} + W_{12}), \tag{5.14b}$$

$$\tau_3 = (W_{03} + W_{13} + W_{23}), \tag{5.14c}$$

where τ_1 describes the relaxation from $|\psi_1\rangle$ to the lower-lying states (in this case only $|\psi_0\rangle$), τ_2 describes the relaxation from $|\psi_2\rangle$ to the lower-lying states, and τ_3 describes the relaxation from $|\psi_3\rangle$ to the lower-lying states (see Eq. (5.11)). We expect that τ_3 should be dominated by W_{13} while τ_2 should be dominated by W_{02}. τ_1 should be small due to the difference in predominant spin of states $|\psi_0\rangle$ and $|\psi_1\rangle$.

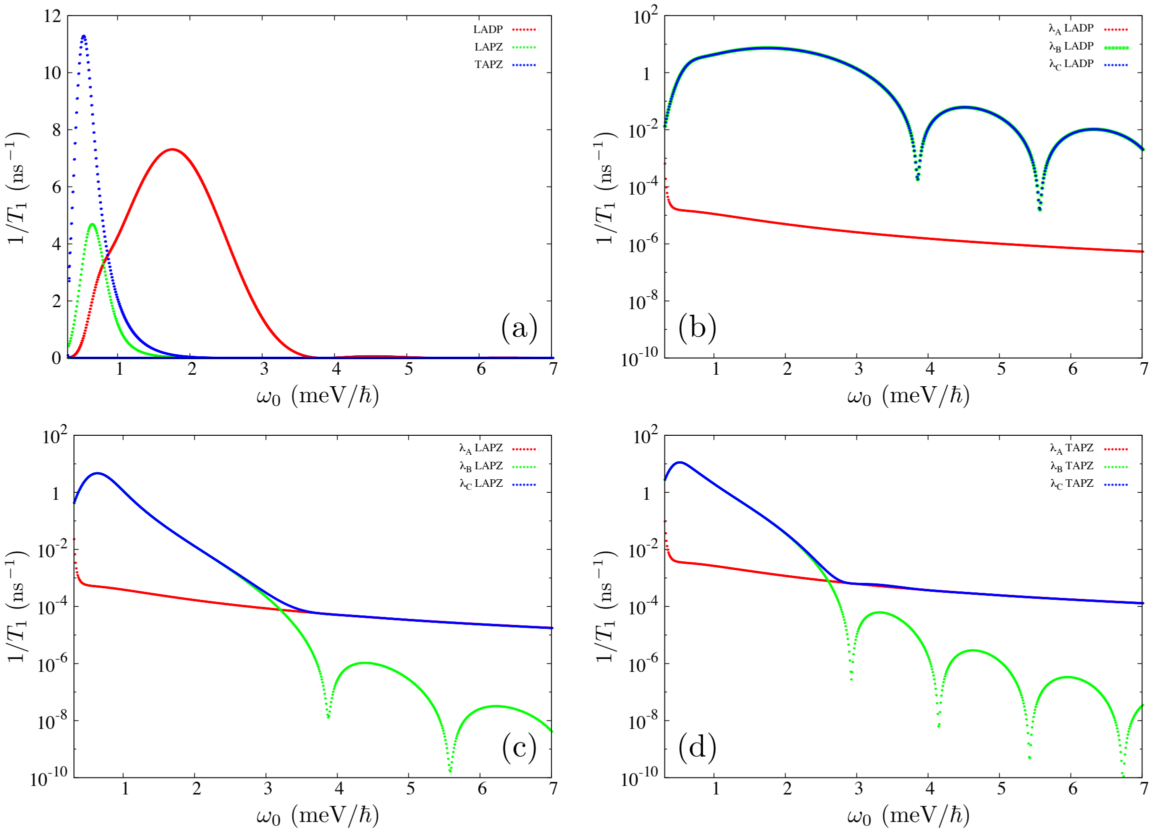

Figure 5.12: (a) Relaxation rates of the SO states with $\alpha_R = 1$ meV·nm and $\beta_D = 3$ meV·nm as a function of ω_0 at $B = 1$ T. Individual relaxation rates for the (b) LA-DP interaction, (c) LA-PZ interaction, and (d) TA-PZ interaction.

5.2.2 Relaxation Rates with Small Spin-Orbit Effect

In this section we examine the relaxation rates in the system as a function of ω_0 for small SO interaction strength. The relaxation rates with $\alpha_R = 1$ meV·nm and $\beta_D = 3$ meV·nm are shown in Fig. 5.12. The relaxation rates are plotted on a linear scale in panel (a), and appear to be identical to the relaxation rates of the non-SO case as depicted in panel (a) of Fig. 5.4. The log scale plots for each interaction (panels (b), (c), and (d) of Fig. 5.12) reveal some subtle differences. The oscillatory relaxation rates observed in the non-SO case are present for each interaction when SO is included, and are labeled as λ_B for each interaction in panels (b), (c), and (d). As expected, there are two additional relaxation rates due to the inclusion of the SO effect. For the LA-DP interaction in panel (b), one of the additional rates, labeled as λ_C, appears to be degenerate with the previously observed oscillatory branch. The other additional rate, labeled as λ_A, is a smaller, "flat" branch. Each of the PZ interactions also has a "flat" branch, also labeled as λ_A in their respective panels. For each PZ interaction, the rate λ_C transitions from the greatest peak (near $\omega_0 = 0.5$ meV/$\hbar$) to a flat curve as ω_0 increases. In fact, for each interaction, λ_C is equivalent to the sum of λ_A and λ_B.

Using the results of the secular approximation as a guide, the "flat" branch labeled λ_A in the LA-DP interaction (Fig. 5.12 (b)) is determined to be τ_1 since the transition rate W_{01} is expected to be very small. Furthermore, λ_A undergoes the least amount of change as ω_0 is varied, just as one would expect for W_{01}. The oscillatory branches, λ_B and λ_C, are each either τ_2 or τ_3. Next consider the PZ interactions in panels (c) and (d). As mentioned above, λ_C appears to be degenerate with λ_B for smaller values of ω_0, but then transitions to a degeneracy with λ_A for larger values of ω_0. λ_B is therefore τ_2 and λ_C is τ_3: τ_2 is expected to be dominated by W_{02} for the entire range of ω_0 since the contribution of both W_{02} and W_{12} is expected to be qualitatively similar with $W_{02} > W_{12}$. τ_3 would be dominated by W_{13} for smaller values of ω_0, just as τ_2 is dominated by W_{02}, but dominated by W_{23} for larger values of ω_0, since W_{23}, like W_{01}, is expected to vary very little with increasing ω_0.

The inclusion of SO at this small strength opens up new relaxation channels in the system. For the most part it does not change the original, non-SO channels except in the case of the PZ interaction at larger values of omega: When SO was neglected there were key values of ω_0 where the lifetime of an excited state could be increased by orders of magnitude as indicated by the minima in the oscillating relaxation channels. When SO is included, new relaxation channels allow for faster relaxation in the PZ interaction at these key ω_0 values. At these larger values of ω_0, all of the relaxation channels due to the PZ interaction are still very small compared to the original, oscillating LA-DP relaxation channel, except at the minima in the LA-DP channel, where some of the PZ rates are approximately the same. Therefore, in the single particle system for this set of parameters, where all three electron-phonon interactions are present, the SO interaction produces no measurable change in the relaxation rates.

5.2.3 Decoherence Rates with Small Spin-Orbit Effect

We next examine the remaining, complex, eigenvalues of the Redfield tensor, which contain information about the decoherence times of the system, when $\alpha_R = 1$ meV·nm and $\beta_D = 3$ meV·nm. As expected there are six different decoherence rates in the four-level system. These are plotted in Fig. 5.13. The panels on the left-hand side of the figure display the real parts of the eigenvalues, i.e. the decoherence rates, associated with each interaction, while the panels on the right-hand side of the figure display the magnitudes of the imaginary components of each corresponding eigenvalue. We examine the imaginary parts first. The magnitudes of the imaginary components are identical for each interaction. Two sets of them are degenerate, namely $|\lambda_{a,i}|$ and $|\lambda_{b,i}|$, and $|\lambda_{c,i}|$ and $|\lambda_{f,i}|$. Each of these imaginary components is proportional to the energy difference between the SO states. Specifically, $|\lambda_{a,i}|$ and $|\lambda_{b,i}|$ are proportional to the energy difference between states $|\psi_0\rangle$ and $|\psi_1\rangle$, and states $|\psi_2\rangle$ and $|\psi_3\rangle$ ($\Delta E_{01} = \Delta E_{23}$), $|\lambda_{c,i}|$ and $|\lambda_{f,i}|$ are proportional to the energy difference between states $|\psi_0\rangle$ and $|\psi_2\rangle$, and states $|\psi_1\rangle$ and $|\psi_3\rangle$ ($\Delta E_{02} = \Delta E_{13}$), $|\lambda_{d,i}|$ is proportional to the energy difference between states $|\psi_0\rangle$ and $|\psi_3\rangle$, and finally $|\lambda_{e,i}|$ is proportional to the energy difference between states $|\psi_1\rangle$ and $|\psi_2\rangle$.

As in the non-SO case the decoherence rates generally subscribe to being half of the relaxation rates. By comparing combinations of the relaxation rates in Fig. 5.12 to the decoherence rates in Fig. 5.13, we find for each interaction that the decoherence rates are as follows:

$$\begin{aligned}
\lambda_{a,r} &= \tfrac{1}{2}\left(\lambda_B + \lambda_C\right) \equiv \tfrac{1}{2}\left(\tau_2 + \tau_3\right) \\
\lambda_{b,r} &= \tfrac{1}{2}\,\lambda_A \equiv \tfrac{1}{2}\,\tau_1 \\
\lambda_{c,r} &= \tfrac{1}{2}\,\lambda_B \equiv \tfrac{1}{2}\,\tau_2 \\
\lambda_{d,r} &= \tfrac{1}{2}\,\lambda_C \equiv \tfrac{1}{2}\,\tau_3 \\
\lambda_{e,r} &= \tfrac{1}{2}\left(\lambda_A + \lambda_B\right) \equiv \tfrac{1}{2}\left(\tau_1 + \tau_2\right) \\
\lambda_{f,r} &= \tfrac{1}{2}\left(\lambda_A + \lambda_C\right) \equiv \tfrac{1}{2}\left(\tau_1 + \tau_3\right)
\end{aligned} \tag{5.15}$$

Under the secular approximation the eigenvalues of the Redfield tensor can be complex, with the real parts representing decay and the imaginary parts representing oscillations. We use the secular approximation again to explain the above findings. We begin with λ_b: Recall that the imaginary component of λ_b is the associated with

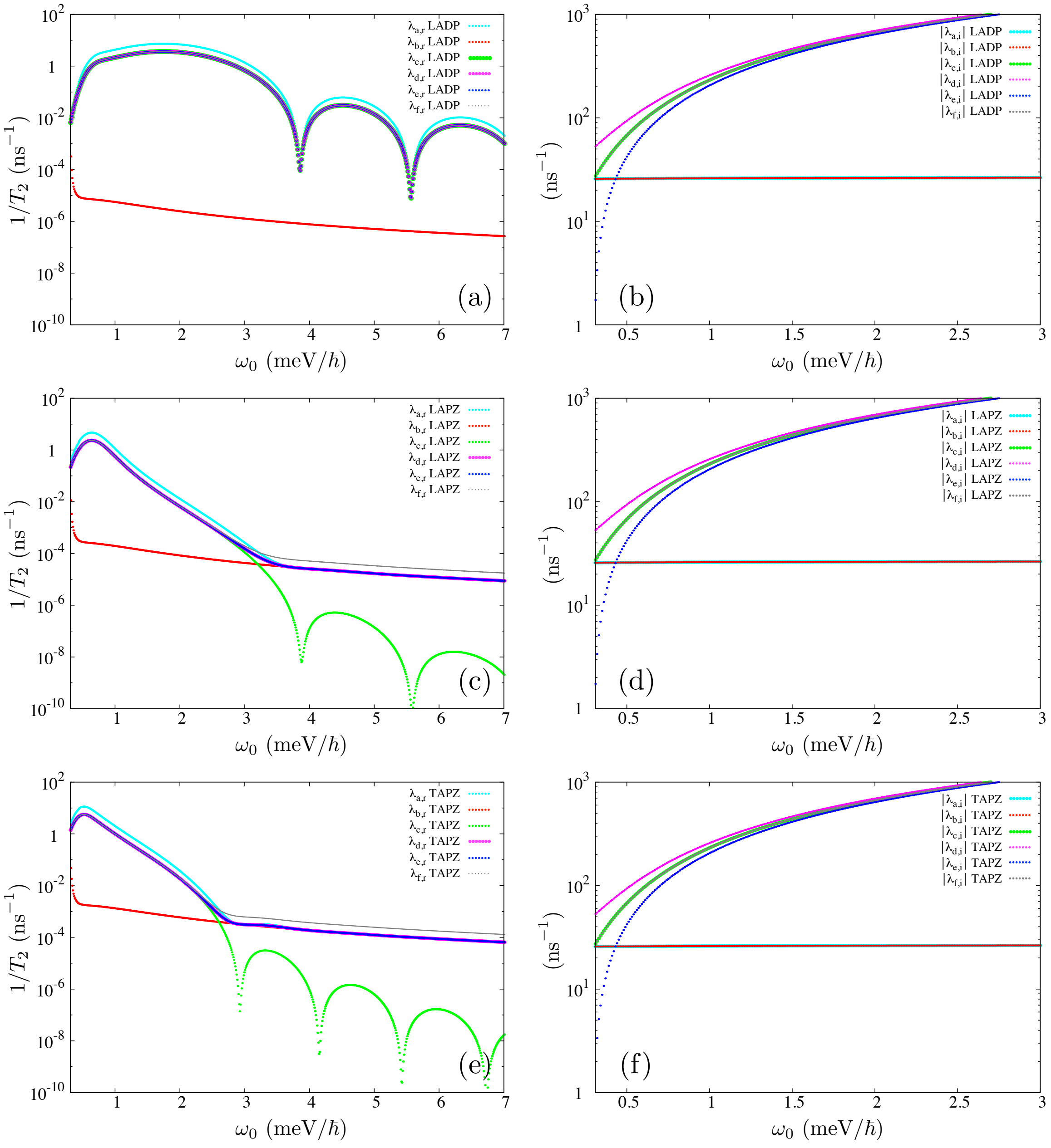

Figure 5.13: Decoherence rates of the SO states with $\alpha_R = 1$ meV·nm and $\beta_D = 3$ meV·nm as a function of ω_0 at $B = 1$ T. Panels (a), (c), and (e) display for each interaction the real parts of the complex eigenvalues of the Redfield tensor which represent the decoherence rates, while panels (b), (d), and (f) display the magnitudes of the corresponding imaginary components of each eigenvalue.

the energy difference between either $|\psi_0\rangle$ and $|\psi_1\rangle$, or $|\psi_2\rangle$ and $|\psi_3\rangle$. Since the real component of λ_b is equal to half of the relaxation rate $\tau_1 = W_{01}$, it is reasonable that $|\lambda_{b,i}|$ be identified with the energy difference between states $|\psi_0\rangle$ and $|\psi_1\rangle$. This leaves

$|\lambda_{a,i}|$ to be the energy difference between states $|\psi_2\rangle$ and $|\psi_3\rangle$, which is consistent with $\lambda_{a,r} = (\tau_2 + \tau_3)/2$ since τ_3 contains W_{23}. In the same manner, the imaginary component of λ_c is proportional to the energy difference between states $|\psi_0\rangle$ and $|\psi_2\rangle$, while the imaginary component of λ_f is proportional to the energy difference between states $|\psi_1\rangle$ and $|\psi_3\rangle$. Finally, $\lambda_{d,r}$ and $\lambda_{e,r}$ in the left panels of Fig. 5.13 can be distinguished using their respective imaginary components: Since $|\lambda_{d,i}|$ is proportional to ΔE_{03} $\lambda_{d,r}$ therefore must be $\tau_3/2$ which contains W_{03}, while the fact that $|\lambda_{e,i}|$ is proportional to ΔE_{12} means that $\lambda_{e,r}$ is equal to $(\tau_1 + \tau_2)/2$, which contains W_{12}. $\lambda_{d,r}$ and $\lambda_{e,r}$ appear to be the same in the left panels of Fig. 5.13 for the following reasons: At small ω_0, τ_1 (λ_A) is much smaller than τ_2 (λ_B) so $\lambda_{e,r} \approx \frac{1}{2}\tau_2$. Also τ_3 (λ_C) and τ_2 are approximately the same, so $\lambda_{d,r} \approx \lambda_{e,r}$. At large ω_0, τ_2 becomes much smaller than τ_1 so now $\lambda_{e,r} \approx \frac{1}{2}\tau_1$. Since τ_3 and τ_1 are now approximately the same, we again have $\lambda_{d,r} \approx \lambda_{e,r}$.

We next turn to the effect of increasing the strength of the SO interaction to $\alpha_R = 10$ meV·nm and $\beta_D = 30$ meV·nm while keeping the magnetic field at $B = 1$ T.

5.2.4 Relaxation Rates with Large Spin-Orbit Effect

The relaxation rates for in the system as a function of ω_0 with $\alpha_R = 10$ meV·nm and $\beta_D = 30$ meV·nm are plotted in Fig. 5.14. The relaxation rates found in this case are qualitatively similar to those found when $\alpha_R = 1$ meV·nm and $\beta_D = 3$ meV·nm for each interaction, however there are some differences which stand out. One of these changes is a shift toward smaller ω_0 values for peak positions. This can be attributed to the increase in the energy difference between all of the states when the SO interaction strength is increased. The relation between peak position and energy difference was first observed in Secs. 5.1.1 and 5.1.2, where the relaxation peaks shifted due to the changes in the energy difference between the QD states as ω_0 and B were varied. We found that the peaks coincided approximately with the same phonon energy, i.e. state energy difference, in all cases. Here, as the SO strength, and hence the energy differences between the SO states, is increased, the energy of the emitted phonon which coincides with the relaxation peaks occurs at smaller values of ω_0.

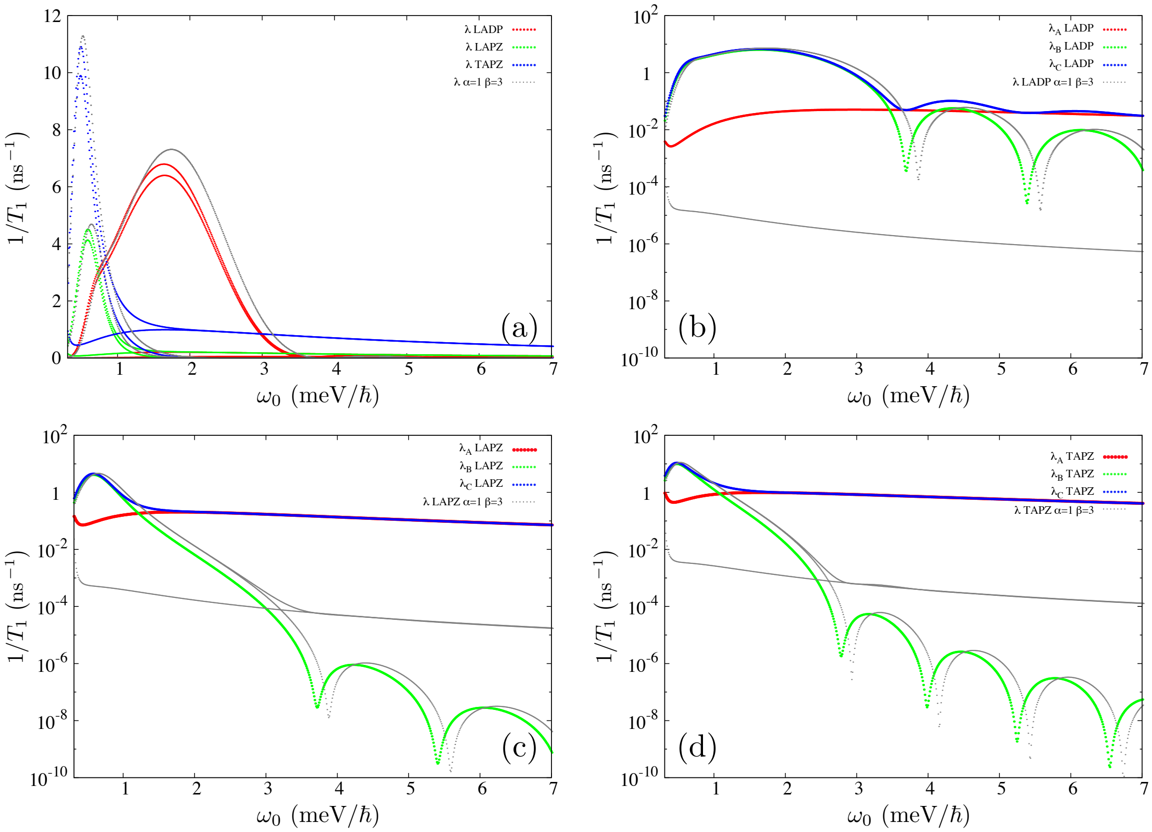

Figure 5.14: (a) Relaxation rates of the SO states with $\alpha_R = 10$ meV·nm and $\beta_D = 30$ meV·nm as a function of ω_0 at $B = 1$ T. Individual relaxation rates for the (b) LA-DP interaction, (c) LA-PZ interaction, and (d) TA-PZ interaction. The relaxation rates when $\alpha_R = 1$ meV·nm and $\beta_D = 3$ meV·nm are plotted in grey on each panel for comparison.

Other obvious, and perhaps more interesting, changes include the following: There is a general reduction in the height of the greatest peak for each interaction, which is most clear in panel (a). This shows that, with respect to these particular peaks, the relaxation time in the system *increases* with increasing SO strength. Another change is the significant increase of the relaxation rate λ_A for all interactions. Both of these changes can once again be explained in terms of the transition rates W_{ij}. As discussed previously, and as illustrated in Fig. 5.11, the balance of basis states in the SO states shifts towards a more equal distribution as the SO strength increases. This has a significant impact on the transition rates. Consider for example the transition between states $|\psi_1\rangle = c\,|0\,0\downarrow\rangle - d\,|0\,1\uparrow\rangle$ and $|\psi_3\rangle = b\,|0\,0\uparrow\rangle + ia\,|0\,1\downarrow\rangle$: As the SO strength increased, these states went from being almost exclusively spin-down states to states which contained a mix of spin-up and spin-down. For almost all values of ω_0 examined, the weight on each spin-up (spin-down) basis state in each SO state is different. This mismatch obstructs somewhat the transitions between these two states. For example, at larger values of ω_0 ($\omega_0 > 1$ meV/$\hbar$), $|\psi_3\rangle$ has about 10% of its weight on a spin-up state. $|\psi_1\rangle$ is still almost exclusively spin-down, which is largely unchanged from when the SO strength was smaller. Since the electron-phonon interaction conserves spin, the weight on the spin-down state in $|\psi_3\rangle$ can transition completely to the spin-down state in $|\psi_1\rangle$, however the weight on the spin-up state in $|\psi_3\rangle$ has very little spin-up state in $|\psi_1\rangle$ to transition to. This reduces the decay channel between these two SO states from when the two states were both almost exclusively spin-up. In other words, as α_R increases from 1 meV·nm to 10 meV·nm and β_D increases from 3 meV·nm to 30 meV·nm, the transition rate W_{13} decreases. The exception occurs near $\omega_0 = 0.43$ meV/$\hbar$, where $|a|^2 = |c|^2$ and $|b|^2 = |d|^2$. At this point the weight on each spin-species in each SO state is the same, and so the transition is unobstructed. The same can be said for W_{02}. The remaining transition rates, W_{01}, W_{03}, W_{12}, and W_{23}, increase as SO strength increases due to the change in coefficients, since transitions between states which were primarily obstructed due to spin differences now have a greater degree of spin in common. W_{01} and W_{23} will be affected more so than W_{03} and W_{12} at large values of ω_0, where the coefficients $|c|^2 \to 1$ and $|d|^2 \to 0$.

These changes explain the increase in λ_A, which was attributed to $\tau_1 = W_{01}$ in the $\alpha_R = 1$ meV·nm, $\beta_D = 3$ meV·nm case. They also explain the reduction in peak height for λ_B and λ_C. λ_B was attributed to $\tau_2 = W_{02} + W_{12}$ and W_{02} is expected to decrease in this case. Similarly, λ_C was attributed to $\tau_3 = W_{03} + W_{13} + W_{23}$, and the reduction in W_{13} reduces the height of the largest peak at the smaller end of the ω_0 scale. At large ω_0 W_{23}, which is expected to increase yet remain largely unchanged as a function of ω_0, dominates τ_3 when W_{13} becomes very small.

Another note of interest is that the apparent degeneracy between λ_B and λ_C observed for smaller values of ω_0 when the SO strength was small is lifted for this stronger SO interaction, by approximately 1 ns^{-1}, with λ_C having the slightly greater relaxation rate. This can be explained by the fact that W_{02} and W_{13}, which are equal to each other, decrease by the same amount, while W_{01} and W_{23}, which are also equal to each other, increase by the same amount. Since τ_3 contains W_{23} while τ_2 does not contain either W_{01} or W_{23}, it is reasonable that λ_C should be slightly greater than λ_B.

5.2.5 Decoherence Rates with Large Spin-Orbit Effect

The decoherence rates for $\alpha_R = 10$ meV·nm and $\beta_D = 30$ meV·nm undergo the same trends as seen in the relaxation rates. These are displayed in Fig. 5.15. Panels (a), (b), and (c) show the decoherence rates for each interaction, LA-DP, LA-PZ, and TA-PZ, respectively. Panel (d) shows the imaginary components of the corresponding eigenvalues. As in the case when the SO-interaction was small, these imaginary parts correspond to the changes in energy between all of the SO states, and are identical for each type of interaction. Furthermore, the decoherence rates are equal to the same superposition of relaxation rates as described in Eq. (5.15).

Just as seen for the relaxation rates, the ω_0 values at which peak heights occur shift slightly to smaller values. Also, the height of the largest peak shifts slightly downward from their values when SO was small for most of the decoherence rates, with the exception of $\lambda_{b,r}$, which increases significantly for all values of ω_0. $\lambda_{b,r}$ was identified earlier with the secular rate $\tau_1 = W_{01}$. Its change is consistent with that observed for the relaxation rate λ_A, which is speculated to be due to the increase in the transition rate W_{01}. $\lambda_{c,r}$ was associated with $\tau_2 = W_{02} + W_{12}$ and undergoes the least change, which is also consistent with the relaxation rate λ_B in this case. The largest degree of change for the remaining four decoherence rates occurs at large values of ω_0 ($\omega_0 > 3.5$ meV/$\hbar$ for LA-DP, and $\omega_0 > 1$ meV/$\hbar$ for PZ). Here $\lambda_{a,r}$, $\lambda_{d,r}$, $\lambda_{e,r}$, and $\lambda_{f,r}$ all increase significantly from when the SO strength was small. Each of these decoherence rates can be linked to either (or both) W_{01} or W_{23}, which as discussed above, are expected to be greatly impacted with the increase in SO strength.

A final note of interest regarding the decoherence rates is that, when the SO strength was small, $\lambda_{c,r}$, $\lambda_{d,r}$, $\lambda_{e,r}$, and $\lambda_{f,r}$ appeared to be degenerate for smaller values of ω_0 (and for all values of ω_0 in case of the LA-DP interaction). With the increase in SO strength, this degeneracy breaks very slightly, on the order of ~ 0.1 ns^{-1}, with $\lambda_{f,r}$ having the largest peak, followed by $\lambda_{d,r}$, $\lambda_{e,r}$, then $\lambda_{c,r}$. This is similar to what happens between the relaxation rates λ_B and λ_C. $\lambda_{f,r}$ contains both W_{01} and

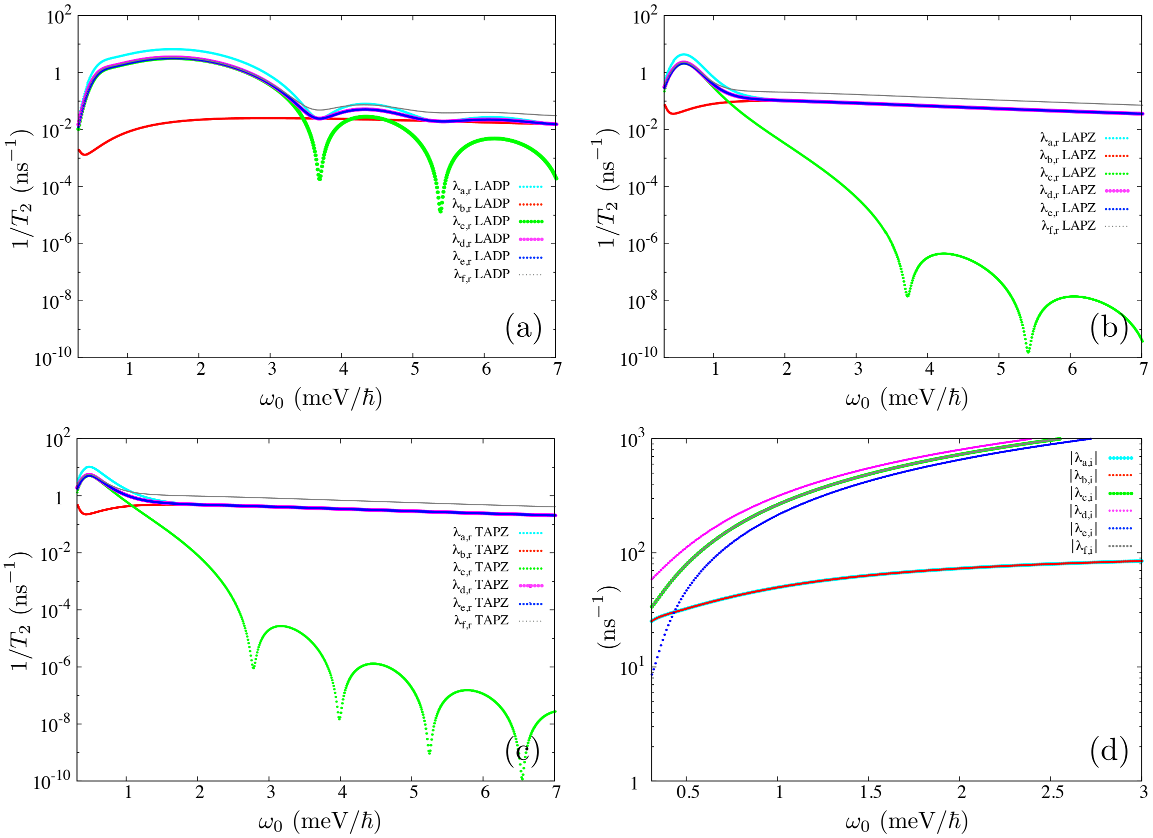

Figure 5.15: Decoherence rates of the SO states with $\alpha_R = 10$ meV·nm and $\beta_D = 30$ meV·nm as a function of ω_0 at $B = 1$ T. Panels (a), (b), and (c) display for each interaction the real parts of the complex eigenvalues which represent the decoherence rates, while panel (d) displays the magnitudes of the corresponding imaginary components of each eigenvalue. (The imaginary components are identical for all three interactions.)

W_{23}, which are expected to have the greatest increase with increasing SO strength. $\lambda_{d,r}$ contains W_{23} while $\lambda_{e,r}$ contains W_{01}, both of which should increase identically with increasing SO strength. Also, $\lambda_{d,r}$ contains W_{13} while $\lambda_{e,r}$ contains W_{02}, both of which should decrease identically with increasing SO strength. However, they each contain an additional transition rate, with W_{03} in $\lambda_{d,r}$ and W_{12} in $\lambda_{e,r}$. Since $\beta_D > \alpha_R$ in our model, the SO state coefficients a and b have a greater change than c and d (see Eqs (5.11) and (5.12) and Fig. 5.11), allowing for a larger transition rate between SO states $|\psi_0\rangle$ and $|\psi_3\rangle$ versus SO states $|\psi_1\rangle$ and $|\psi_2\rangle$ with increasing SO strength. In other words, W_{03} should be greater than W_{12}, and so $\lambda_{d,r}$ should be greater than $\lambda_{e,r}$, accordingly. Finally, $\lambda_{c,r}$ contains neither W_{01} nor W_{23}, and so it is reasonable that $\lambda_{f,r} > \lambda_{d,r} > \lambda_{e,r} > \lambda_{c,r}$.

We have shown that when ω_0 is small (less than approximately 3.5 meV/$\hbar$ for LA-DP and 1 meV/$\hbar$ for PZ) the increase in SO strength reduces slightly the relaxation and decoherence rates in the system, making the states longer-lived. However, as ω_0 increases, the stronger SO interaction introduces relaxation and decoherence channels which were relatively inconsequential in the weaker case and nonexistent when SO was absent. Favourable values of ω_0 which corresponded with minima in the relaxation and decoherence rates become obsolete due to the rise of these new decay channels.

In the next chapter we examine the effects of Coulomb interaction on the decay rates of the system when SO is both neglected and considered.

Chapter 6

Phonon-Induced Decay of a Three-Electron State

We now turn to the effects of correlations as induced by Coulomb interaction on the relaxation and decoherence rates of the system. In general a correlated state is a state which cannot be expressed as a single state in any basis; it can only be written as a superposition of basis states with clear phase relations between them. In this dissertation we describe the degree of correlation in terms of the number of basis states required to define a state such that probability is conserved ($\langle\psi|\psi\rangle = 1$). Specifically, we fix our basis to antisymmetrized products of Fock-Darwin states, Eq. (2.3). The degree of correlation is defined as the minimal number of such product-states required to achieve $\langle\psi|\psi\rangle > 0.99$. For example, in an uncorrelated state probability is conserved when the state is expressed using a single Slater determinant, however the description of a highly correlated state requires many Slater determinants to conserve probability. In this chapter we present a method for disentangling the effects of Coulomb-induced correlations in the system from the effects of Coulomb-induced energy changes on these decay rates. To our knowledge this has not been seen in the literature before.

We study a three-electron QD system where long-range Coulomb interactions exist between the electrons. The three-electron system is chosen because, as stated previously, it is the simplest interacting system which contains the meron spin textures as defined in Sec. 3.3. The relaxation and decoherence rates of the system are first calculated in the absence of the SO interaction in Sec 6.1. The exclusive impact of the Coulomb-induced electronic correlations on the system relaxation rates is studied in Sec. 6.1.1.

The effect of including the SO interaction as a perturbation in the system is examined in Sec. 6.2. We consider the same SO interaction strengths as studied in the previous chapter. The relaxation and decoherence rates for the large SO interaction strength are calculated in Sec. 6.2.2 and Sec. 6.2.2, respectively. The relaxation and decoherence rates for a SO interaction strength more conventionally accepted for GaAs are calculated in Sec. 6.2.3 and Sec. 6.2.4, respectively.

6.1 Decay of Three-Electron States in Absence of Spin-Orbit Interaction

In this section we examine the influence of Coulomb interaction on the relaxation rate between the first excited state and the ground state of the three-electron (N=3) system due to phonon-emission. The Coulomb interaction between the three electrons in the QD bring about two major changes from the single-electron (N=1) system discussed in Chap. 5, namely it changes the energy level spacings between the QD eigenstates, and introduces electronic correlations within each eigenstate. Both of these changes will have an impact on the decay rates of the system. As seen in the previous chapter, the energy level difference between the states involved in the transition is equal to the energy of the emitted phonon. The phonon energy has a direct effect on the relaxation rates, albeit in different ways depending on the type of interaction (DP or PZ). The electron correlations within each the initial and final states also affect the decay rates, as can be seen in Eq. (4.12), for example, where the states $|k\rangle$, $\left|m^{(\prime)}\right\rangle$, and $\left|n^{(\prime)}\right\rangle$ are the correlated eigenstates of the interacting system. In addition to calculating the relaxation rates in the N=3 system, we wish to isolate the effect of both correlation and energy on these rates.

Despite the introduction of Coulomb interaction between electrons in the QD, the relaxation from the initial to final state is still a two-level system in the absence of SO. The density matrix has the same general form as presented at the beginning of Sec. 5.1. The relaxation and decoherence rates in the N=3 system investigated here are the same as those in the N=1 system (Eq. (5.7), and Eq. (5.8), respectively). Because the decoherence rate is equal to half of the relaxation rate, we show results only for the relaxation rate in this section. Just as in the N=1 case, the electron-phonon interaction does not change the spin of the electron. The results presented in this section are independent of the projection of the electron-spin of the states used.

The application of an external magnetic field to the interacting many-electron QD induces energy level crossings in the ground state of the system (see Fig. 2.2 for example). Such a phenomenon is not seen in the absence of interaction (e.g. the N=1 case investigated in Chap. 5). It is near these degeneracy points where merons may occur (see Sec. 3.3). In the case of the N=3 system, the first degeneracy point in the ground state occurs between states which have the necessary quantum numbers to create meron states. In the results presented in this chapter, we keep the confinement frequency fixed and vary the magnetic field about the first degenerate point in the ground state while determining the relaxation rates.

In order to evaluate the effects of electron correlations on the relaxation rates, we vary the strength of the Coulomb interaction in our Hamiltonian (see Eq. (2.2)). We introduce here the parameter α, which scales the dielectric constant of the system. Specifically, ϵ in Eq. (2.2) is $\epsilon = \epsilon_{GaAs}/\alpha$, and ϵ_{GaAs} is the dielectric constant for GaAs. The Coulomb interaction term scales directly with α, such that when $\alpha = 0$ the system is non-interacting, and when $\alpha = 1$ the Coulomb interaction is at full strength in GaAs. This method of varying the degree of Coulomb interaction has been done in Ref. [117].

In the N=3 system, the ground state and first excited state involved in the first level crossing are defined by the quantum numbers $L_z = -1$, $S = 1/2$, and $L_z = -2$, $S = 1/2$. For the results presented in this chapter we keep the confinement frequency constant at $\omega_0 = 3$ meV/$\hbar$. Fig. 6.1 shows the energy spectrum of the lowest-lying eigenstates in the QD in the absence of Coulomb interaction between the electrons ($\alpha = 0$) and in the fully interacting GaAs system ($\alpha = 1$). In the non-interacting limit convergence between sets of states occurs as $B \to \infty$. As α increases, B^* is reduced; when $\alpha = 1$, $B^* = 1.63$ T. We vary α between 0 and 1, and calculate the relaxation rate between the first excited state and the ground state as B approaches B^*. At B^*, due to the degeneracy between the states, $1/T_1 = 0$.

We first examine the relaxation rates for the fully-interacting case, where $\alpha = 1$. These rates are shown in Fig. 6.2 for each type of electron-phonon interaction as a function of B. Trends that were observed in the N=1 system in Sec. 5.1 are seen here in the N=3 system. In the N=1 case without SO we found that when the relaxation rate is examined as a function of magnetic field, the TA-PZ interaction peaks at larger magnetic field values than the rates for both the LA-DP and LA-PZ interactions. (Refer to Fig. 5.7 for the N=1 relaxation rates as a function of B.) This is consistent with the fact that, as discussed in Sec. 5.1, the PZ interaction becomes dominant over the DP interaction as the energy of the emitted phonon decreases. In the N=3 case,

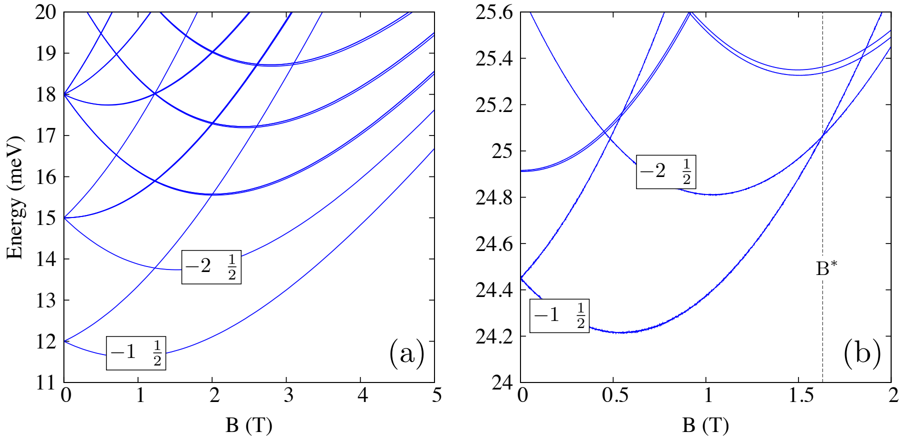

Figure 6.1: Lowest-lying energy spectrum of the N=3 interacting system as a function of B in the non-interacting limit (α=0) (a), and the fully-interacting GaAs system (α=1) (b). The confinement frequency in each plot is $\omega_0 = 3$ meV/$\hbar$. The two states used in this dissertation are labelled by their L_z and S quantum numbers.

the phonon energy decreases as B approaches B^* due to the approaching degeneracy of the ground state and the first excited state. As a consequence, the relaxation rate due to the TA-PZ interaction dominates over the rates due to both the LA-DP and the LA-PZ interactions as $B \to B^*$. This finding is observed in all N=3 cases examined in this dissertation and is independent of the strength of Coulomb interaction. For all three interaction types the relaxation rates decrease to zero at B^* due to the zero phonon density of states at this degeneracy point. In comparing the N=3 relaxation rates in Fig. 6.2 with those for N=1 at the same confinement frequency of $\omega_0 = 3$ meV/$\hbar$ (Fig. 5.7 (c)), we find that the relaxation rates decrease in the N=3 case by almost two orders of magnitude. (Though not shown in Fig. 5.7 (c), the TA-PZ relaxation rate for N=1 at $\omega_0 = 3$ meV/$\hbar$ peaks at a value of 34 ns^{-1} near $B = 12$ T.) Climente *et al.* [20] explain the reduction in relaxation rates in terms of the additional single-electron transitions that come about with increasing the number of particles in the system. In ref [20], transitions between the lowest-lying single-electron orbitals, namely the s-shell, p-shell, and d-shell orbitals, are fixed such that their transition energies are all equal. The relaxation rates between individual single-electron orbitals are then compared. They find that the $p \to s$ transition is the fastest, and so when additional particles are added to the QD, the additionally required relaxation channels via the higher occupied orbitals slow the overall relaxation rate.

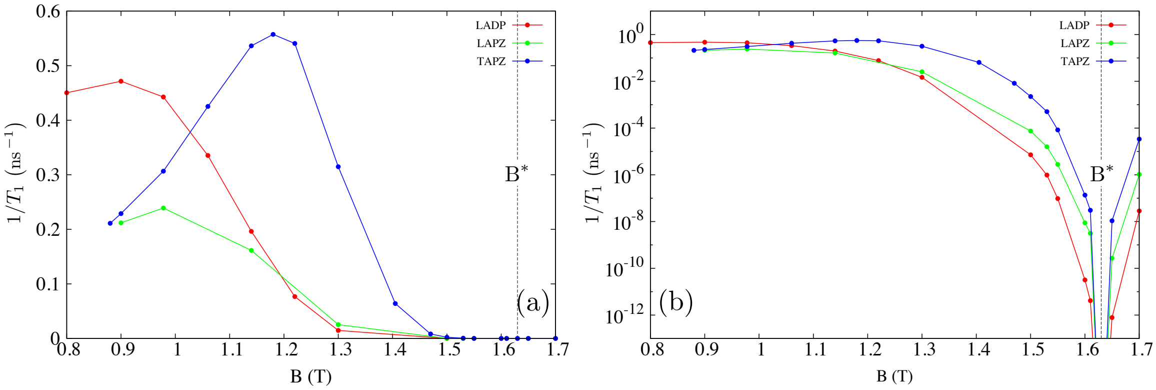

Figure 6.2: Relaxation rates for each electron-phonon interaction between the $L_z = -2$, $S = 1/2$ excited state and the $L_z = -1$, $S = 1/2$ ground state in the fully-interacting ($\alpha = 1$) QD. B^* is labelled on each plot by the vertical dashed line. The plots in both (a) and (b) display the same data, however the log plot reveals in more detail how the relaxation rates tend to zero as $B \to B^*$.

In general we have found that, although the relaxation rates for all three interactions tend to zero as $B \to B^*$, the relaxation rate due to the TA-PZ interaction is the dominant rate around B^* in all cases examined. For this reason we consider only the TA-PZ relaxation rate for the remaining cases examined in this dissertation. Additionally, the relaxation rates are observed to be approximately symmetric about B^* for a small range of B about B^*. Since rate calculations at $B > B^*$ reveal no further insight into the behaviour of the relaxation rates around B^*, we restrict our calculations to values $B < B^*$.

Here we introduce the reduced magnetic field, $B_{red} = \Delta B/B^*$, where $\Delta B = (B - B^*)$. We next compare the relaxation rates for cases with different interaction strengths (different values of α) as a function of B_{red}. As previously mentioned, B^* occurs at different magnetic fields for different interaction strengths. Additionally, B^* increases with decreasing interaction strength. Consequently, the rate of change of level spacing between the ground state and the first excited state is much slower as $B \to B^*$ when α is small. A small step in B from B^* in a weakly interacting system does not have the same impact as a small step in B from B^* in a strongly interacting system. For example, when $\alpha = 0.2$, the peak of the TA-PZ relaxation rate occurs when $\Delta B \sim -1.5$ T, however when $\alpha = 1$, the peak of the relaxation rate occurs when $\Delta B \sim -0.5$ T. By using B_{red}, B^* occurs when $B_{red} = 0$ for all α, and the peak relaxation rate for each interaction strength examined approximately coincide with

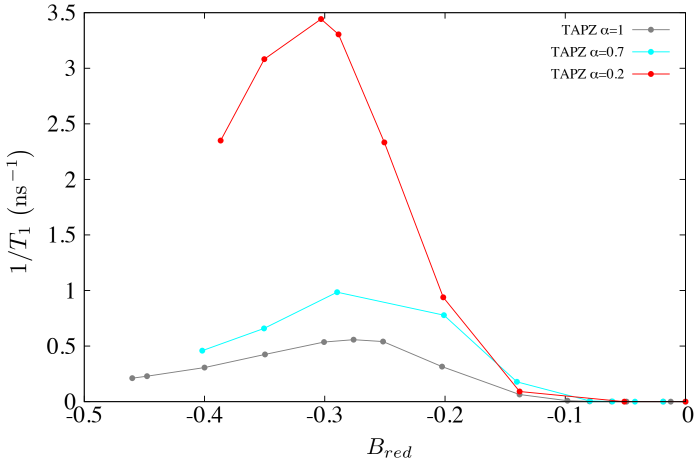

Figure 6.3: Relaxation rates for the TA-PZ electron-phonon interaction between the excited state and the ground state for the fully-interacting system when $\alpha = 1$ (grey), for an intermediate interaction strength when $\alpha = 0.7$ (cyan), and for a weakly-interacting system when $\alpha = 0.2$. B^* occurs when $B_{red} = 0$ for each case.

each other.

Fig. 6.3 shows the TA-PZ relaxation rates for three different interaction strengths, $\alpha = 0.2$, $\alpha = 0.7$, and $\alpha = 1$. When α is increased from 0.2 to 0.7, the peak of the relaxation rate decreases by ~ 2.5 ns^{-1}. When α is increased from 0.7 to 1, the peak of the relaxation rate decreases further by another ~ 0.5 ns^{-1}. Again, this reduction in the relaxation rate can be explained in terms of the single-electron relaxation rates, despite the fact that the number of electrons in the system is constant: The increase in interaction strength increases the degree of correlation in the state, reducing the dominance of the $p \to s$ transition as additional relaxation channels open between orbitals with slower relaxation rates. The overall transition rate is therefore slowed. This increase in the degree of correlation can be seen in both the ground state and the excited state in Fig. 6.4 for $\alpha = 0.2$, $\alpha = 0.7$, and $\alpha = 1$ when $B_{red} = -0.3$ (coinciding approximately with the peaks in the relaxation rates for each value of α). These histograms display the magnitude of the coefficients associated with each basis state. The basis states are ordered by decreasing weight. For both states and all interaction strengths shown, the combined weight of the first 15 basis states makes up 98.5% or more of the weight of the entire eigenstate. (The eigenstates are normalized such that $\sum_i |c_i|^2 = 1$.) The first three basis states in the ground state for each α are the same, and the first five basis states in the excited state for each α are the same. The order

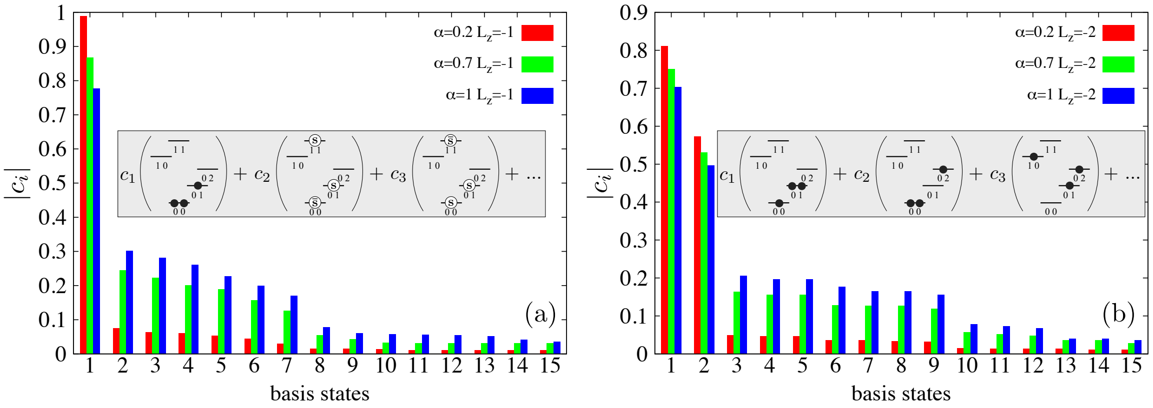

Figure 6.4: Magnitude of the coefficients for the first 15 most heavily weighted basis states in the ground state (a), and the excited state (b) for $\alpha = 0.2$ (red), $\alpha = 0.7$ (green), and $\alpha = 1$ (blue). The orbital configurations of the first three basis states are shown in the grey box for both states. (In the ground state, the second and third basis states differ only by spin.)

of the weighting of the remaining basis states varies with α. The grey box inside each panel (a) and (b) illustrates the orbital configuration of the first three basis states for each the ground state and the first excited state, respectively. In the case of the ground state, the first basis state represents the orbital configuration of the eigenstate in the non-interacting limit. As the interaction strength increases, the weight on this basis state decreases as it spreads across all other possible N=3 configurations with the same quantum numbers. In the case of the excited state, the non-interacting limit is a correlated state between the first two basis states. This correlation is not induced by Coulomb interaction, rather it is due to the degeneracy of the $L_z = -2$ state in the non-interacting limit. For this state, as the interaction strength increases, the weights on these first two basis states decrease while the weights on all other possible N=3 configurations with the same quantum numbers increase. The increase in basis state mixing with increasing α serves to increase the number of different transitions between orbitals. These additional relaxation channels replace to some degree the main $p \rightarrow s$ channel between the excited state and the ground state and reduce the overall relaxation rate.

6.1.1 Disentangling Correlation Effects from Energy Effects on Relaxation Rates

We have shown above that increasing the Coulomb interaction strength increases the degree of correlation in the states, and reduces the overall relaxation rates in the system. However, increasing the interaction strength also changes the energy levels in the system as well, and so it is not clear if the degree of correlation has a significant effect on the change in rates compared to the effects the change in energy levels could have. For example, in Fig. 6.3, consider the difference in relaxation rates between $\alpha = 0.2$ and $\alpha = 0.7$ when $B_{red} \sim -0.2$ and $B_{red} \sim -0.14$. When $B_{red} \sim -0.2$ the relaxation rate for $\alpha = 0.2$ is faster than that for $\alpha = 0.7$, although they are close (within 0.2 ns^{-1} of each other). At this point, the transition energies for each α are very close together (between $\sim$ 0.01 meV and $\sim$ 0.02 meV), however $\Delta E_{\alpha=0.7} > \Delta E_{\alpha=0.2} > \Delta E_{\alpha=1}$. (In fact, $\Delta E_{\alpha=0.7} > \Delta E_{\alpha=0.2}$ for $B_{red} >$ -0.29.) As B_{red} approaches zero, the transition energies become even smaller. When $B_{red} \sim -0.14$, the relaxation rate for $\alpha = 0.2$ actually becomes lower than that for $\alpha = 0.7$, despite the greater degree of correlation in the $\alpha = 0.7$ case. (The difference in transition energies between $\alpha = 0.7$ and $\alpha = 0.2$ are still between $\sim$ 0.01 meV and $\sim$ 0.02 meV here.) As expected, both correlations and transition energies play a role in the relaxation rate. In Ref. [19] Bertoni *et al.* isolate correlation effects from energy effects on the relaxation rate of an interacting two-electron system by artificially fixing the transition energy to the non-interacting value. In this section, we disentangle the effect of Coulomb-induced electronic correlations from the effect that the natural change in energy-level spacing has on the relaxation rates without artificially setting the transition energies.

In order to isolate the effects of correlation on the relaxation rates, we compare the relaxation rates for two different interaction strengths where their transition energies ΔE are equal for the same B_{red}. Fig. 6.5 displays the transition energies for $\alpha = 0.1$ to $\alpha = 1$ as a function of B_{red}. All transition energies become zero at the degeneracy point, when $B_{red} = 0$, however the rate at which they do so depends on the interaction strength. The transition energies for two different values of α are equal for the same B_{red} where their curves intersect. We calculate and compare the relaxation rates between these particular pairs of α.

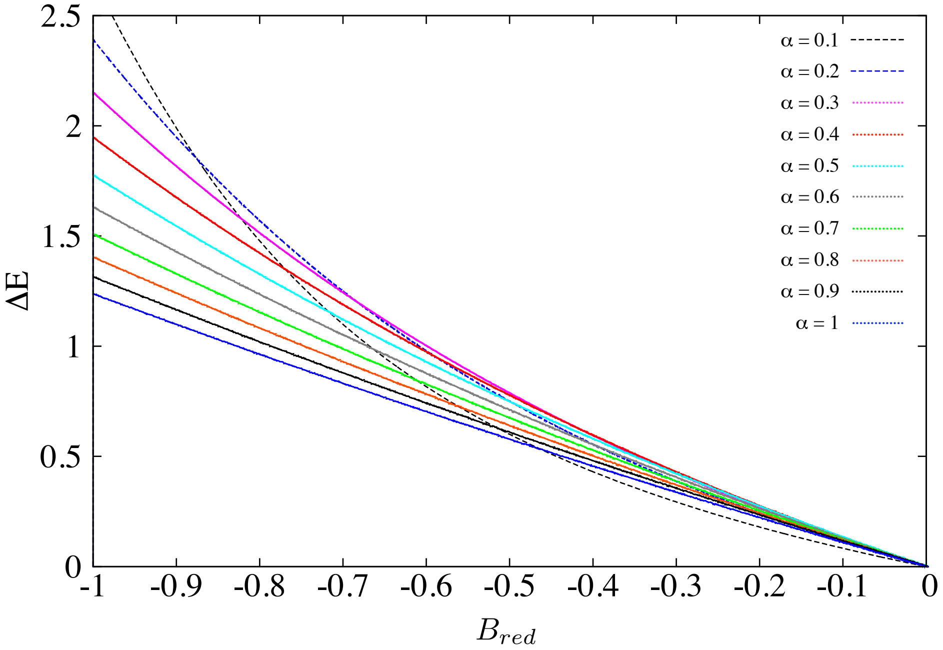

Figure 6.5: Transition energies (ΔE) for various α as a function of B_{red}.

Fig. 6.6 shows the relaxation rates for pairs of α which have the same transition energy at the same B_{red}. These calculations are done for parameter values where the transition energies are naturally equal and not fixed in any way. In each case, as the Coulomb interaction strength increases, the relaxation rate decreases. Since electronic correlations within the states are greater with stronger Coulomb interaction, these results show that correlations, independent of energy changes, act to reduce the relaxation time of the system. Note that the amount of change in the relaxation rates depends on the value of B_{red}. Generally speaking, the relaxation rates drop to zero as $B_{red} \to 0$ ($B \to B^*$) and as $B_{red} \to -1$ ($B \to 0$) (see Figs. 6.2 and 6.3). Although the relaxation rates do not necessarily peak at the exact same value of B_{red}, they all tend to peak near $B_{red} \sim -0.3$. The transition energy degeneracies do not necessarily occur near peak values in their relaxation curves as a function of B_{red}, and can align when the relaxation rates are small. For example, in the case of $\alpha = 0.2$ vs $\alpha = 0.7$ in Fig. 6.6, the transition energies for each α are equal near their peaks, where the difference in their respective transition rates are approximately at a maximum. In contrast, for $\alpha = 0.3$ vs $\alpha = 0.6$, their transition energies are equal away from their peaks, where the relaxation rates for both are small relative to their peak

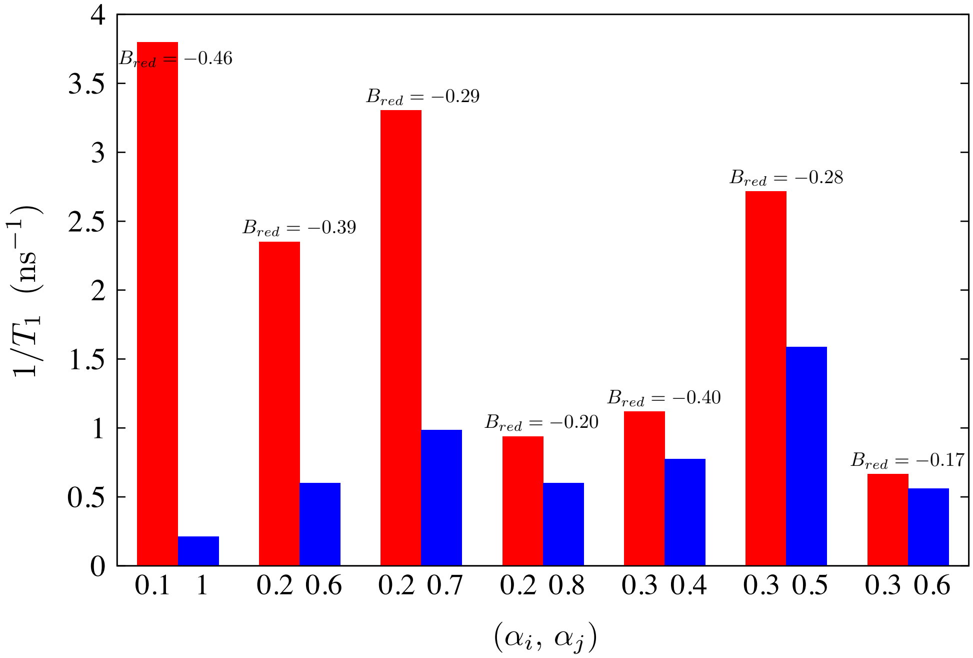

Figure 6.6: Relaxation rates for pairs of α where the transition energies are equal at the same B_{red}. In every case examined, the relaxation rate is reduced as the degree of correlation is increased with increasing interaction strength. B_{red} is indicated for each pair.

rates. Therefore, the difference in relaxation rates between different pairs of degenerate α cannot always be directly compared. There are two cases where the transition energies are degenerate near the peak values: Between $\alpha = 0.2$ and $\alpha = 0.7$, as mentioned, and also between $\alpha = 0.3$ and $\alpha = 0.5$. Note that the difference between the relaxation rates is greater in the case of $\alpha = 0.2$ vs $\alpha = 0.7$ than it is for $\alpha = 0.3$ vs $\alpha = 0.5$. In the former case the degree of correlation has the greatest amount of change. In general, for each pair investigated, the relaxation rates always decrease as the degree of correlation in the states is increased.

6.2 Decay of Three-Electron States in Presence of Spin-Orbit Interaction

In this section the effects of the SO interaction on the relaxation and decoherence rates of the three-electron QD system are considered. As in the previous section we examine the decay rates as a function of B for a constant confinement frequency of $\omega_0 = 3$ meV$/\hbar$. The Coulomb interaction strength is taken to be at full strength for

GaAs ($\alpha = 1$) for all results discussed in this section.

The SO interaction mixes states with different spin and so to accommodate this the ground state subspace must be expanded from that presented in the previous section. As in the N=1 system, this subspace in the absence of SO contains four states for the parameters investigated. For the N=3 system these states are:

$$\begin{aligned} |0\rangle &\equiv |L_z\!=\!-1,\;\; S\!=\!1/2,\;\; S_z\!=\!1/2\rangle\,, \\ |1\rangle &\equiv |L_z\!=\!-1,\;\; S\!=\!1/2,\;\; S_z\!=\!-1/2\rangle\,, \\ |2\rangle &\equiv |L_z\!=\!-2,\;\; S\!=\!1/2,\;\; S_z\!=\!1/2\rangle\,, \\ |3\rangle &\equiv |L_z\!=\!-2,\;\; S\!=\!1/2,\;\; S_z\!=\!-1/2\rangle\,. \end{aligned} \tag{6.1}$$

This subspace adheres to the requirements for meron formation, and these four states become degenerate to within the Zeeman splitting (0.02 meV) at $B^* = 1.63$ T (see Fig. 6.1 (b)). As in Sec. 5.2, when the SO interaction is included the total Hamiltonian is $H = H_{QD} + H_{SO}$. H is diagonalized in the subspace of the four states in Eq. (6.1). The form of the energy eigenvalues and eigenstates, or SO states, are identical to those expressed in Eqs. (5.10), (5.11), and (5.12), with the exception that the basis states $|0\rangle$, $|1\rangle$, $|2\rangle$, and $|3\rangle$ (see Eq. (6.1)) are each no longer a single Slater determinant as in the non-interacting case, but rather a large superposition of Slater determinants due to the Coulomb-induced correlations. As in the previous section, we calculate the decay rates for $B < B^*$. In this case, the general form of the eigenstate coefficients are identical to those expressed in Eq. (5.12). (See App. B.2 for details.) Upon calculating the SO states we make an approximation to our three-electron basis states listed in Eq. (6.1): To expedite the calculation times of the decay rates for the SO states, the basis states are truncated to a weight of 99.9% of the original state with no significant loss of fidelity. See App. B.3 for details.

We consider the same two sets of SO parameters introduced in Sec. 5.2 in the proceeding calculations, namely a small SO effect, $\alpha_R = 1$ meV·nm, $\beta_D = 3$ meV·nm, and a large SO effect, $\alpha_R = 10$ meV·nm, $\beta_D = 30$ meV·nm. The energy spectrums of the SO states for each SO parameter set are displayed in Fig. 6.7, along with the lowest-lying energies of the N=3 system in the absence of SO for reference. The energies of the basis states in Eq. (6.1) are the four lowest-lying non-SO energies in Fig. 6.7 between ~ 0.5 T $< B <\sim 1.8$ T. Note that, despite expectations, the SO effect does *not* lift the degeneracy of the four SO states at B^*. The SO energies are

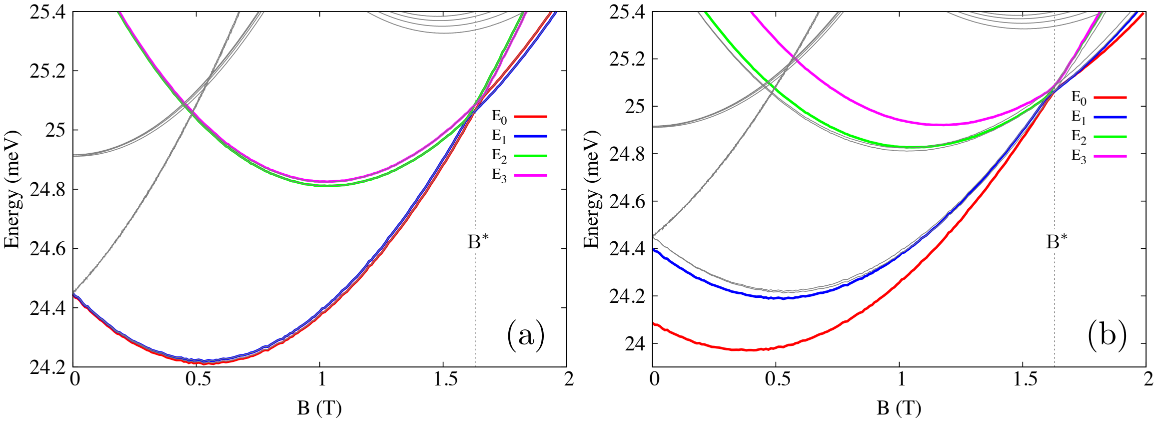

Figure 6.7: Energy spectrum of the four SO states in the N=3 interacting system as a function of B (presented in colour) with $\alpha_R = 1$ meV·nm, $\beta_D = 3$ meV·nm (a), and $\alpha_R = 10$ meV·nm, $\beta_D = 30$ meV·nm (b). The grey lines are the lowest-lying energies of the N=3 system in the absence of SO. B^* is labelled on each plot by the vertical dashed line.

scaled by $\mathcal{E}_\pm^2$ (see Eqs. (3.17) and (5.10)). Analytically, as $B \to B^*$ the SO energies become

$$E_0 \to e - \beta_D \mathcal{E}_-, \tag{6.2a}$$

$$E_1 \to e - \alpha_R \mathcal{E}_+, \tag{6.2b}$$

$$E_2 \to e + \alpha_R \mathcal{E}_+, \tag{6.2c}$$

$$E_3 \to e + \beta_D \mathcal{E}_-, \tag{6.2d}$$

where e is the degenerate energy of the four basis states in Eq. (6.1) at B^*. However, as indicated in Fig. 6.8, $\mathcal{E}_\pm$ approaches zero as $B \to B^*$, and therefore, regardless of the strength of the SO interaction, the degeneracy is not lifted in this case. Generally speaking, the linear SO Hamiltonian can only mix unperturbed QD eigenstates which differ in both L_z and S_z by only one quantum. It is reasonable that SO states which are a superposition of such QD states transition smoothly through B* without breaking the underlying degeneracy of the unperturbed system. On the other hand, other degeneracy points in the unperturbed QD spectrum which involve states with L_z and S_z values which differ by more than one quantum cannot be mixed by the linear SO effect, and so these degeneracy points might transform into anti-crossings when SO is included as a perturbation.

When the SO interaction strength is small the SO energies do not vary significantly

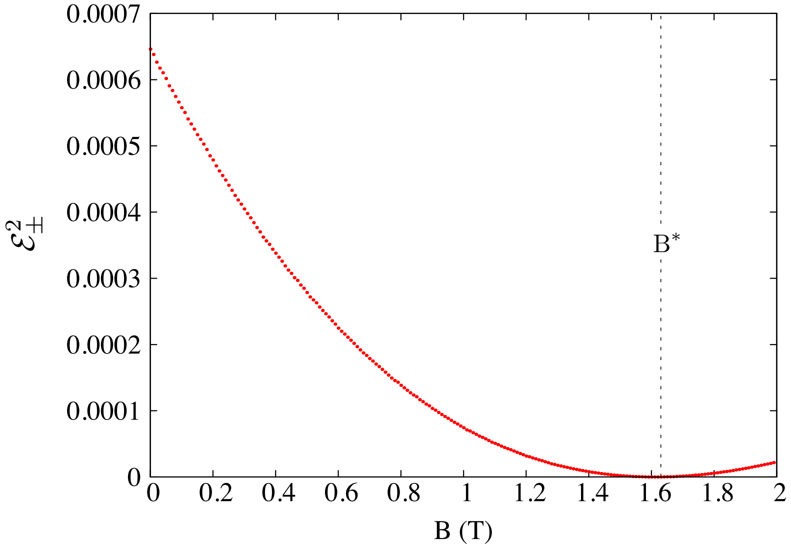

Figure 6.8: $\mathcal{E}^2_{\pm}$ a function of B in the N=3 ground state subspace defined in Eq. (6.1) ($\omega_0 = 3$ meV$/\hbar$). The energies of the SO states depend on $\mathcal{E}^2_{\pm}$; as $\mathcal{E}^2_{\pm} \to 0$ at B^* the SO energies become degenerate with each other.

from those of the basis states. Just as in the N=1 case (Sec. 5.1.1), the SO states are almost exclusively composed of a single H_{QD} state for the entire range of magnetic field investigated except within ~ 0.05 T of B^*. For $B < B^*$ $|\psi_0\rangle \approx |0\rangle$, $|\psi_1\rangle \approx |1\rangle$, $|\psi_2\rangle \approx |2\rangle$, and $|\psi_3\rangle \approx |3\rangle$; for $B > B^*$ $|\psi_0\rangle \approx |3\rangle$, $|\psi_1\rangle \approx |2\rangle$, $|\psi_2\rangle \approx |1\rangle$, and $|\psi_3\rangle \approx |0\rangle$. The degree of mixing increases as B approaches B^* because the magnitude of the coefficients in the SO states become equal.

For the stronger SO effect the degree of mixing between the H_{QD} states increases and the energies of the SO states differ from the energies of the basis states for the majority of the range of magnetic field investigated except near the degeneracy point, where the behaviour is the same as in the case of the small SO effect. For the majority of the magnetic field range investigated the non-dominant basis state makes up $\sim 4\%$ of the eigenstates $|\psi_1\rangle$ and $|\psi_2\rangle$ and $\sim 18\%$ of the eigenstates $|\psi_0\rangle$ and $|\psi_3\rangle$. This is an increase in the weights of the non-dominant states over those found for the N=1 system. Just as in the N=1 case, the difference in the amount of mixing between the SO states is because β_D mixes the basis states $|0\rangle$ and $|3\rangle$ while α_R mixes the basis states $|1\rangle$ and $|2\rangle$ (see Eqs. (5.11) and (5.12)), and we have taken $\beta_D > \alpha_R$.

In the next two sections we examine the effects of the larger SO interaction on the relaxation and decoherence rates in the fully interacting ($\alpha = 1$) three-electron

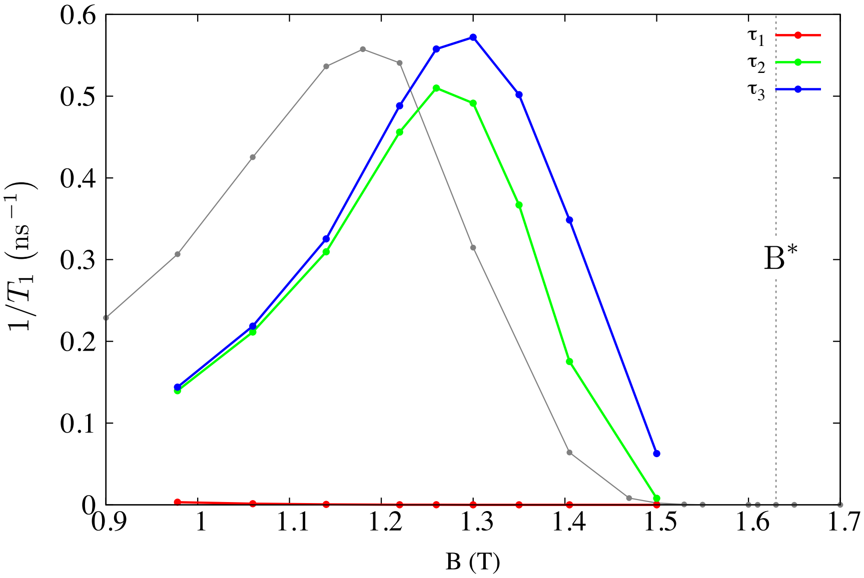

Figure 6.9: TA-PZ relaxation rates of the N=3 SO states with $\alpha_R = 10$ meV·nm and $\beta_D = 30$ meV·nm as a function of B at $\omega = 3$ meV/$\hbar$. The relaxation rate of the N=3 system in the absence of SO is plotted in grey for reference.

system. This is done for clarity because the effects are more pronounced when the SO strength is large. The chapter then concludes with results for the smaller SO interaction which is more conventional for a GaAs QD.

6.2.1 Relaxation Rates with Large Spin-Orbit Effect

In this section we examine the relaxation rates of the interacting three-electron system as a function of B when the SO interaction strength is large. The results displayed in this section are for a constant confinement frequency of $\omega_0 = 3$ meV/$\hbar$. The relaxation rates are plotted in Fig. 6.9. For comparison the relaxation rate for the non-SO case is also displayed in this figure. As seen in the single-electron QD system there are three relaxation rates in the three-electron system when SO is included: τ_1, τ_2, and τ_3 (see Eq. (5.14)). One relaxation rate, τ_1, is very small. The other two rates, τ_2 and τ_3, are of similar magnitude to the relaxation rate in the non-SO three-electron system, however, in comparing them to the non-SO case, there is a shift in where their peaks occur as a function of B.

We consider first the peak heights of each τ_1, τ_2, and τ_3. The smallest rate, τ_1, describes the relaxation between the SO states $|\psi_1\rangle$ and $|\psi_0\rangle$. These states are primarily composed of opposite spin-species (see Eqs. (5.11), and (6.1)). Since the electron-phonon interaction conserves spin, the relaxation rate between these states should be very small. The two larger rates, τ_2 and τ_3, describe the relaxation from the two highest-energy states, $|\psi_2\rangle$ and $|\psi_3\rangle$, respectively, to the lower-lying states. These rates are similar to those in the non-SO case because their main relaxation channels (W_{02} and W_{13}, respectively), involve transitions between states that are similar to those in the non-SO case, namely a transition from the $L_z = -2$ state to the $L_z = -1$ state with the same S_z. In the strong SO regime the peak of τ_2 drops by ~ 0.05 ns^{-1} in comparison to the non-SO case. This reduction in τ_2 occurred in the N=1 system when the SO strength was increased. The relaxation rate τ_2 takes into account the transition rates from the SO state $|\psi_2\rangle$ to the SO states $|\psi_0\rangle$ and $|\psi_1\rangle$ (W_{02} and W_{12}, respectively). The state $|\psi_0\rangle$ is primarily composed of the same spin as the state $|\psi_2\rangle$, while the state $|\psi_1\rangle$ is primarily composed of the opposite spin. Therefore W_{02} is greater than W_{12} for the spin-conserving electron-phonon interaction. In this case W_{02} decreases due to the reduced overlap between SO states $|\psi_0\rangle$ and $|\psi_2\rangle$, just as in the N=1 case (see Sec. 5.2.4). Though W_{12} increases, the overlap induced by the increased SO strength between states $|\psi_1\rangle$ and $|\psi_2\rangle$ is still small enough that it does not increase the overall relaxation rate.

Unlike what was observed in the N=1 system, the peak of τ_3 actually increases slightly, by ~ 0.02 ns^{-1}. Recall $\tau_3 = W_{03} + W_{13} + W_{23}$ (Eq. (5.14)). As discussed in the N=1 case when SO strength was increased (Sec. 5.2.4), W_{13} is reduced exactly like W_{02}, while W_{01}, W_{03}, W_{12}, and W_{23} all increase. In the strong SO regime, since the weight of the non-dominant basis state is greater in the N=3 system than it is in the N=1 system, these transition rates have a greater increase. Except near B^*, due to the change in the SO state coefficients with increasing SO strength, the overlap between $|\psi_0\rangle$ and $|\psi_3\rangle$ has the greatest increase. The overlap between $|\psi_0\rangle$ and $|\psi_1\rangle$ is the same as the overlap between $|\psi_2\rangle$ and $|\psi_3\rangle$, and has the next greatest increase. The overlap between $|\psi_1\rangle$ and $|\psi_2\rangle$ has the smallest increase. Since τ_3 contains W_{03} and W_{23} it is logical that the peak in τ_3 be greater than the peak in τ_2.

We now consider the shift in the peak locations of τ_2 and τ_3 as a function of B when compared to the non-SO case. Recall that τ_1, τ_2, and τ_3 correspond to relaxation from SO states $|\psi_1\rangle$, $|\psi_2\rangle$, and $|\psi_3\rangle$, respectively. As the SO strength increases so does

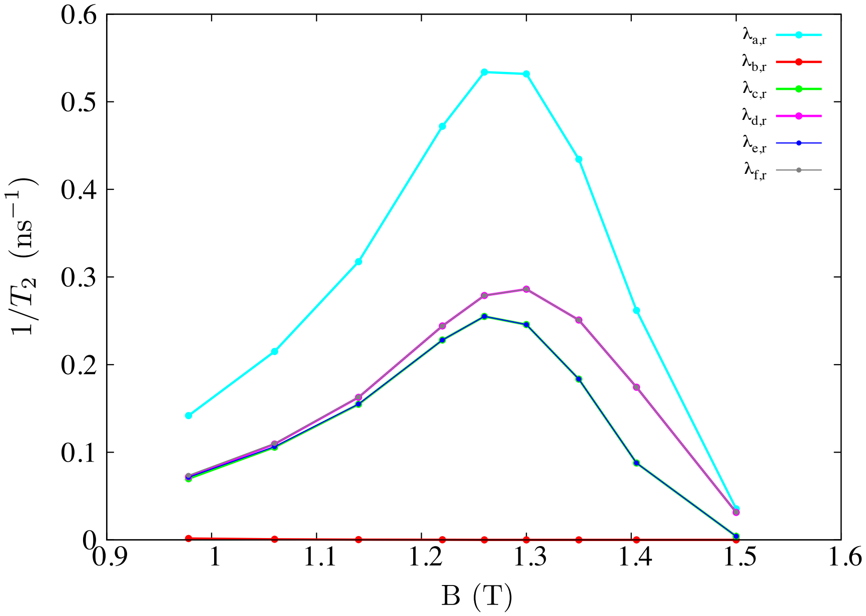

Figure 6.10: TA-PZ decoherence rates of the N=3 SO states with $\alpha_R = 10$ meV·nm and $\beta_D = 30$ meV·nm as a function of B at $\omega = 3$ meV/$\hbar$.

the energy difference between the SO states as a function of B. Recall from Sec. 5.1 that for the non-SO N=1 case the peaks of the relaxation rates coincided with the same SO state energy change, i.e. the same emitted phonon energy, as ω_0 and B were varied. Here, as the SO strength increases, the phonon energies shift to larger values of B to stay the same, and so the peaks in τ_2 and τ_3 shift accordingly. Since relaxation from $|\psi_3\rangle$ produces a phonon with an average energy greater than that emitted via relaxation from $|\psi_2\rangle$, it is logical that τ_3 peaks at a larger value of B than τ_2.

6.2.2 Decoherence Rates with Large Spin-Orbit Effect

We next look at the decoherence rates for the three-electron system in the strong SO regime. These rates are shown in Fig. 6.10. Just as in the N=1 SO case there are six decoherence rates observed for this case. Using the same analysis as described in

Sec. 5.2.3, the decoherence rates are found to be

$$\begin{aligned} \lambda_{a,r} &= \tfrac{1}{2}\left(\tau_2 + \tau_3\right) \\ \lambda_{b,r} &= \tfrac{1}{2}\,\tau_1 \\ \lambda_{c,r} &= \tfrac{1}{2}\,\tau_2 \\ \lambda_{d,r} &= \tfrac{1}{2}\,\tau_3 \\ \lambda_{e,r} &= \tfrac{1}{2}\left(\tau_1 + \tau_2\right) \\ \lambda_{f,r} &= \tfrac{1}{2}\left(\tau_1 + \tau_3\right). \end{aligned} \tag{6.3}$$

These decoherence rates are in fact the same as those identified in the single-electron SO system (see Eq. 5.15).

In this case we see that $\lambda_{c,r} \approx \lambda_{e,r}$, and $\lambda_{d,r} \approx \lambda_{f,r}$. This is because the relaxation rate τ_1 is much smaller than the relaxation rates τ_2 and τ_3 (see Fig. 6.9). This effectively makes $\lambda_{e,r} \approx \frac{1}{2}\,\tau_2 = \lambda_{c,r}$ and $\lambda_{f,r} \approx \frac{1}{2}\,\tau_3 = \lambda_{d,r}$.

We now investigate the effect of decreasing the SO strength on the relaxation and decoherence rates to values more acceptable for a GaAs QD. As above the confinement frequency is kept at $\omega_0 = 3$ meV/$\hbar$ while the magnetic field is varied.

6.2.3 Relaxation Rates with Small Spin-Orbit Effect

Figure 6.11 displays the relaxation rates for the N=3 system when $\alpha_R = 1$ meV·nm, $\beta_D = 3$ meV·nm. Just as when the SO interaction strength is large, we see that one relaxation rate, τ_1, is very small. The other two relaxation rates, τ_2 and τ_3, are almost the same as the relaxation rate in the non-SO three electron system (also displayed in Fig. 6.11).

In comparing τ_1 here to the case when the SO interaction was large, it has decreased by several orders of magnitude (not shown). When the SO interaction strength is small the energy levels of the states involved in the transition, $|\psi_0\rangle$ and $|\psi_1\rangle$, are nearly identical (see Fig. 6.7 (a)), depleting the phonon density of states. Furthermore, the smaller SO strength does not induce as much mixing between the basis states in each SO state, and so $|\psi_0\rangle$ and $|\psi_1\rangle$ are almost exclusively composed of opposite spin-species. For these two reasons the relaxation rate due to the spin-conserving electron-phonon interaction between these states is much smaller than when the SO interaction strength is large.

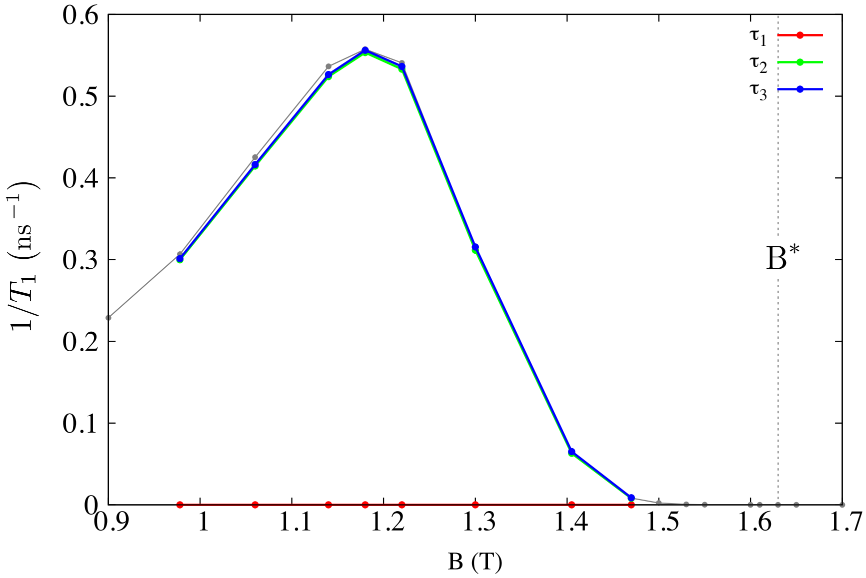

Figure 6.11: TA-PZ relaxation rates of the N=3 SO states with $\alpha_R = 1$ meV·nm and $\beta_D = 3$ meV·nm as a function of B at $\omega = 3$ meV/$\hbar$. The relaxation rate of the N=3 system in the absence of SO is plotted in grey for reference.

Next we consider the two larger rates, τ_2 and τ_3. Recall $\tau_2 = (W_{02} + W_{12})$ and describes the relaxation from the excited state $|\psi_2\rangle$ while $\tau_3 = (W_{03} + W_{13} + W_{23})$ and describes the relaxation from the excited state $|\psi_3\rangle$ (see Eq. (5.14)). As in the N=1 case, W_{02} and W_{13} are identical to each other. Since τ_3 otherwise contains an additional transition rate, it is reasonable that τ_3 be slightly larger than τ_2, just as it is in the large SO case discussed in Sec. 6.2.2. Additionally, since the small SO effect does not cause the energies of the SO states $|\psi_2\rangle$ and $|\psi_3\rangle$ to deviate significantly from the energy level of the excited state in the non-SO N=3 case, nor induce a significant amount of basis state mixing in the SO states for the majority of the B range investigated, it is expected that their relaxation rates be nearly identical to that in the non-SO N=3 case. Unlike when the SO interaction strength was large, the peak locations of each τ_2 and τ_3 do not shift to a higher magnetic field. For this small SO interaction strength the transition energies of the main relaxation channels for the states $|\psi_2\rangle$ and $|\psi_3\rangle$ (W_{02} and W_{13}, respectively) are each nearly identical to the transition energy between the excited state and the ground state in the non-SO case. Relaxation from either SO state $|\psi_2\rangle$ or SO state $|\psi_3\rangle$ emits a phonon with approximately the same energy since the SO energy levels for $|\psi_2\rangle$ and $|\psi_3\rangle$ are nearly

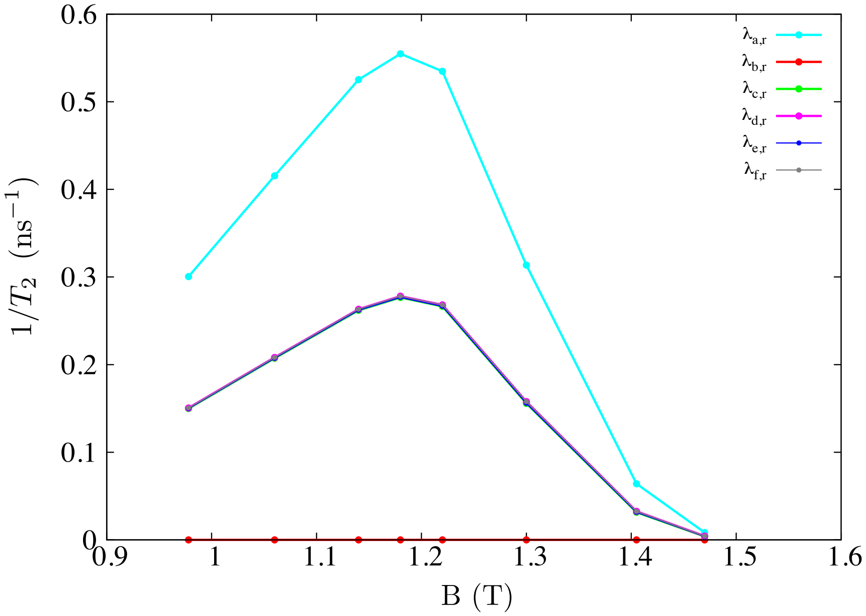

Figure 6.12: TA-PZ decoherence rates of the N=3 SO states with $\alpha_R = 1$ meV·nm and $\beta_D = 3$ meV·nm as a function of B at $\omega = 3$ meV/$\hbar$.

degenerate, as are the energy levels for $|\psi_0\rangle$ and $|\psi_1\rangle$. Therefore the peaks of both τ_2 and τ_3 coincide at the same value of B. Increasing the SO strength lifts this degeneracy[1], and so the peaks not only shift to higher values of B, they additionally do not occur at the same value of B.

6.2.4 Decoherence Rates with Small Spin-Orbit Effect

We finally turn to the decoherence rates in the N=3 system when the SO interaction strength is small. Figure 6.12 displays the decoherence rates as a function of B for $\alpha_R = 1$ meV·nm and $\beta_D = 3$ meV·nm. These decoherence rates are the same as those found when the SO interaction was large (see Eq. (6.3)). Here we see that $\lambda_{c,r} \approx \lambda_{d,r} \approx \lambda_{e,r} \approx \lambda_{f,r}$. The relaxation rate τ_1 is much smaller than the relaxation rates τ_2 and τ_3, on the order of 10^{-10} ns^{-1} or smaller, and is effectively zero (see Fig. 6.11). Just as when the SO interaction strength was large, this makes $\lambda_{e,r} \approx \frac{1}{2}\tau_2 = \lambda_{c,r}$ and $\lambda_{f,r} \approx \frac{1}{2}\tau_3 = \lambda_{d,r}$. In this case it is also true that $\tau_2 \approx \tau_3$, and so these four decoherence rates appear to be the same in Fig. 6.12.

In comparing the decoherence rates for each SO strength the following observations

---

[1] The degeneracy is not lifted at B^*.

can be made. $\lambda_{b,r}$ increases by several orders of magnitude when the SO strength is increased; this is a direct reflection of the increase in the relaxation rate τ_1. Despite the increase this decoherence rate is still very small relative to the other five rates. The peaks in the remaining decoherence rates shift to larger values of B when the SO strength is large, consistent with the shift in the relaxation rates. The peak height of $\lambda_{a,r}$ remains approximately the same for both SO regimes. Recall that for strong SO the relaxation rate τ_3 increased slightly while τ_2 decreased slightly; $\lambda_{a,r}$ is an average of these two rates and so remains effectively unchanged with the change in SO parameters. For both $\lambda_{c,r}$ and $\lambda_{e,r}$ the peaks shrink with increasing SO strength. This is a direct reflection of the reduction experienced by τ_2. Finally, the peaks in $\lambda_{d,r}$ and $\lambda_{f,r}$ undergo a very slight increase with increasing SO strength, due to the change in τ_3.

Overall, the SO interaction affects the transition rates between each SO state differently. Depending on the value of the SO parameters, the overlap between different SO states is either increased or decreased, which impacts the relaxation and decoherence channels accordingly. It is reasonable that there exists a material whose intrinsic SO parameters reduce the dominant decay channels while still keeping the other decay channels suppressed enough such that the SO interaction acts to increase the lifetime and coherence times of the system.

Chapter 7

Conclusion

Using density matrix theory, we developed a foundation for determining relaxation and decoherence rates in a general quantum system *without* applying the secular approximation. The exclusion of this approximation permits the application of this framework to calculating decay rates between system energy levels that may be close together, such as near a degeneracy point. This framework, our generalized Master equation, was then tailored to fit a parabolic QD system. The system-reservoir interaction considered to trigger relaxation and decoherence in the QD system was the electron-phonon interaction, specifically the deformation potential by longitudinal acoustic phonons (LA-DP), and the piezoelectric effect by both longitudinal acoustic phonons (LA-PZ) and transverse acoustic phonons (TA-PZ).

We examined the relaxation and decoherence rates in one-electron and three-electron QDs, both in the absence of and in the presence of the linear spin-orbit (SO) interaction. When the SO effect is neglected, both the one-electron and three-electron QD systems are described as a two-level system. The energy levels are doubly degenerate where the two states in each level differ by their spin. Because the electron-phonon interaction conserves spin, the decay rates are independent of the spin of the states (provided that both initial and final states have the same spin). In the one-electron system, the decay rates between these states were calculated as a function of both confinement frequency ω_0 and applied magnetic field B. Depending on value of these parameters, either the LA-DP interaction or the TA-PZ interaction was found to dominate the decay of the QD system eigenstates, depending on the energy of the emitted phonon. Consistent with the literature, we found that when the phonon energy is small (the phonon wavelength long), the PZ interaction governs the relaxation and decoherence rates. When the phonon energy is large (the phonon wavelength short), the DP interaction governs the rates. Additionally, for particular values of ω_0 and B we found oscillations in the relaxation and decoherence rates, also consistent with the literature. The parameters ω_0 and B affect both the electron wave function and the phonon wave function. The maxima and minima of these oscillations, which can be orders of magnitude apart, correspond to when the overlap between the electron wave function and the phonon wave function is maximized or minimized. It is therefore possible to dampen the decay rates in the QD system by tuning ω_0 and/or B to particular values.

In the three-electron non-SO system the decay rates between the ground state and first excited state were calculated as a function of B near the lowest-lying degeneracy point B^* in the spectrum. Relaxation rates were found to peak before B^*, where they went to zero due to the degeneracy of the eigenstates. In the fully-interacting case (for GaAs) the relaxation rates were found to decrease by approximately two orders of magnitude over those of the single-electron case. We then examined the impact of the Coulomb interaction on the relaxation rates in the three-electron system in more detail, specifically with respect to the role of the Coulomb-induced correlations in the eigenstates. Coulomb interaction affects both the energy level spacings of the eigenstates as well as their degree of correlation. Coulomb interaction between the electrons reduces the relaxation rate in the system, however it is not clear if the Coulomb-induced correlations play a significant role in this rate reduction or if this is due primarily to energy effects. Bertoni *et al.* examine the effect of Coulomb-induced correlations within a two-electron system by forcing the transition energies to be the same as in the single-electron case [19]. In this project we have developed a unique method for decoupling these two properties without having to artificially hold either of them constant. To our knowledge this is the first demonstration of such a technique. By isolating the effects of correlations from the energy changes in the three-electron system, we have shown that correlations alone can play a significant role in reducing the relaxation rates of the system.

When the SO effect is included in the QD model, the number of levels in both the one-electron and three-electron QD systems doubles to four. This is because the SO effect lifts the degeneracy of the levels in the unperturbed system and mixes states of different spin. Spin must be considered to distinguish the states in the manifold. Near the degeneracy point in the three-electron system, the eigenstates of the system with the SO perturbation are meron states. The SO-induced four-level system contains two additional relaxation rates over the non-SO two-level system to account for decay from the two additional excited states. Two SO interaction strengths were examined, a smaller one to take into account the SO effect in GaAs, and a larger one to emphasize the SO effect on decay rates in general.

In both the one-electron and three-electron system, when the SO effect was small, the resulting states were still almost identical to the system states in the absence of SO. Consequently, the dominant relaxation rates were found to be nearly identical to those in the non-SO system. Furthermore, the relaxation rates from the two higher-excited states were found to be nearly identical to each other about the dominant peak. This was due to the lack of any significant degeneracy breaking between both the two higher energy states and the two lower energy states by the small SO strength. When the SO strength was increased, the degeneracy between the two larger relaxation rates was broken. For the set of SO parameters investigated, these relaxation rates saw a slight decrease in the single-electron system, indicating that the SO perturbation in the single-electron system can work to increase the lifetime of the states. In the three-electron system, while one of the dominant relaxation rates decreased with increasing SO strength, the other showed a slight increase. For both SO strengths in both the single-electron and three-electron systems, six different decoherence rates were found, each of which was proportional to a specific single or pair of relaxation rates, independent of the electron-phonon interaction examined. These findings are commensurate with those in the non-SO case, where the decoherence rate was also found to be proportional to the relaxation rate of the system.

Despite our expectations, the meron states induced by the SO parameters investigated in this dissertation did not, on average, significantly reduce relaxation rates in the three-electron system. It is possible that by increasing the number of electrons in the system the lifetimes of the meron states could be increased. The electron-phonon interaction involves the transition of a single electron. A topological state with a greater number of electrons may be better insulated from the effects of a single-electron interaction. In addition, the SO interaction did not seem to break the degeneracy of these meron states at B^*, though it did break the two-fold degeneracy of the upper two and lower two states in the ground state subspace away from B^* when the SO parameters were large enough. In general, it may be possible to find a material with the right balance of the SO parameters α_R and β_D such that the main relaxation channels are significantly reduced while the other channels are not greatly increased, resulting in an overall increased system lifetime. We have already demonstrated the impact of correlations alone in reducing relaxation rates.

Note that in this dissertation we examined each electron-phonon interaction (LA-DP, LA-PZ, and TA-PZ) separately, and did not consider the effect of the total electron-phonon interaction, that is, how the concurrent impact of all three interactions on the system propagate through time. Our aims were to disentangle the effects of correlations from energy on the lifetime of a dissipative QD system, as well as investigate the role of SO in such a system. To study the effects of all three interactions at the same time would not have revealed additional insight into these findings. Furthermore, for the majority of the parameters investigated, especially in the three-electron system near the degeneracy point, there was a single dominant electron-phonon interaction. For materials or system parameters where there is more than one prevalent electron-phonon interaction, the total interaction can be evaluated by summing over each individual interaction, $V(t)^\nu$. The interaction operator $V(t)$ in the Liouville equation at the beginning of Chap. 4 can then be expressed as

$$\begin{aligned} V(t) &= \sum_\nu V(t)^\nu \\ &= \sum_\nu \sum_i F(t)_i^\nu Q(t)_i, \end{aligned} \tag{7.1}$$

where, as in this dissertation, the different interactions are manifest in the reservoir operators ($F_i \equiv \sum_\nu F_i^\nu$). Cross-terms between the different types of interactions ν must then be considered in the time correlation functions $\langle F(t)_i \, F_j \rangle$.

The studies conducted in this dissertation were performed for various QD parameters. Further explorations into the effects of global correlations on the lifetime of the QD system will require the development of a complete analytical framework. Such a framework would allow for the optimization of various QD parameters including B, ω_0, α_R, and β_D. This in turn would aid in selecting a desirable material in which to create the QD system where relaxation and decoherence times in the system are favourable for applications such as quantum computing.

Appendix A

Chirality

A.1 Chiral Spin Current

In this section we derive the expression for the chiral spin current of the spin density vector field in a QD. We begin with the definition of the chirality of a vector field where the QD is taken to lie in the x-y plane. This is expressed in Eq. (3.5), and is written again here for convenience:

$$C_z(r) = \frac{1}{2\pi}\int_0^{2\pi} d\theta \, \frac{\boldsymbol{z}\cdot(\boldsymbol{S}(r,\theta)\times\partial_\theta \boldsymbol{S}(r,\theta))}{|\boldsymbol{S}_\perp(r,\theta)|^2}, \tag{A.1}$$

where $\boldsymbol{S}_\perp(r,\theta) = \boldsymbol{z}\times\boldsymbol{S}(r,\theta)$. Consider first $\boldsymbol{S}(r,\theta)$. Using the definition of $\hat{\boldsymbol{S}}(\boldsymbol{r})$ in Eq. (3.1), we have

$$\begin{aligned} \boldsymbol{S}(r,\theta) &\equiv \langle \hat{\boldsymbol{S}}(r,\theta)\rangle \\ &= \frac{\hbar}{2}\sum_{ss'} \hat{\boldsymbol{\sigma}}_{ss'}\langle \hat{\Psi}^\dagger_s(r,\theta)\hat{\Psi}_{s'}(r,\theta)\rangle, \end{aligned} \tag{A.2}$$

where $\hat{\Psi}^\dagger_\sigma(\boldsymbol{r})$ ($\hat{\Psi}_\sigma(\boldsymbol{r})$) is the field operator creating (annihilating) a fermion with spin $\pm\hbar/2$ at position $\boldsymbol{r}$ (see Eq. (3.2)) and $\hat{\boldsymbol{\sigma}}$ is the vector of Pauli matrices. Then,

$$\begin{aligned} \boldsymbol{S}(r,\theta)\times\partial_\theta\boldsymbol{S}(r,\theta) &= \frac{\hbar^2}{4}\sum_{s_1s_2s_3s_4} \hat{\boldsymbol{\sigma}}_{s_1s_2}\langle\hat{\Psi}^\dagger_{s_1}(r,\theta)\hat{\Psi}_{s_2}(r,\theta)\rangle\times\partial_\theta\hat{\boldsymbol{\sigma}}_{s_3s_4}\langle\hat{\Psi}^\dagger_{s_3}(r,\theta)\hat{\Psi}_{s_4}(r,\theta)\rangle \\ &= \frac{\hbar^2}{4}\sum_{s_1s_2s_3s_4} \hat{\boldsymbol{\sigma}}_{s_1s_2}\times\hat{\boldsymbol{\sigma}}_{s_3s_4}\langle\hat{\Psi}^\dagger_{s_1}(r,\theta)\hat{\Psi}_{s_2}(r,\theta)\rangle\,\partial_\theta\langle\hat{\Psi}^\dagger_{s_3}(r,\theta)\hat{\Psi}_{s_4}(r,\theta)\rangle \end{aligned} \tag{A.3}$$

Consider now the cross product of the Pauli matrices. In the S_z basis, the x and y components of the Pauli matrices are

$$\hat{\sigma}^x = \begin{pmatrix} 0 & 1 \\ 1 & 0 \end{pmatrix}, \tag{A.4a}$$

$$\hat{\sigma}^y = \begin{pmatrix} 0 & -i \\ i & 0 \end{pmatrix}. \tag{A.4b}$$

We express their components as

$$\hat{\sigma}^x_{ss'} = 1 - \delta_{ss'}, \tag{A.5a}$$

$$\hat{\sigma}^y_{ss'} = i(1 - \delta_{ss'})s', \tag{A.5b}$$

where $s^{(')} = \pm 1$ represents the projection of the spin along the z axis. The z-component of the cross-product of the Pauli matrices is then

$$\begin{aligned}\boldsymbol{z} \cdot \hat{\boldsymbol{\sigma}}_{s_1 s_2} \times \hat{\boldsymbol{\sigma}}_{s_3 s_4} &= \left(\hat{\sigma}^x_{s_1 s_2}\hat{\sigma}^y_{s_3 s_4} - \hat{\sigma}^y_{s_1 s_2}\hat{\sigma}^x_{s_3 s_4}\right)\\ &= i\left(s_4(1-\delta_{s_1 s_2})(1-\delta_{s_3 s_4}) - s_2(1-\delta_{s_1 s_2})(1-\delta_{s_3 s_4})\right)\\ &= i(1-\delta_{s_1 s_2})(1-\delta_{s_3 s_4})(s_4 - s_2)\\ &= 2is_4(1-\delta_{s_1 s_2})(1-\delta_{s_3 s_4})(1-\delta_{s_4 s_2}),\end{aligned} \tag{A.6}$$

where in the last line we use the fact that $(s_4 - s_2) = 2s_4(1 - \delta_{s_4 s_2})$. From Eqs. (A.3) and (A.6) the numerator of the integrand in Eq. (A.1) becomes

$$\begin{aligned}\boldsymbol{z} \cdot (\boldsymbol{S}(r,\theta) \times \partial_\theta \boldsymbol{S}(r,\theta)) &= \frac{i\hbar^2}{2}\sum_s s\langle \hat{\Psi}^\dagger_s(r,\theta)\hat{\Psi}_{\bar{s}}(r,\theta)\rangle\, \partial_\theta \langle \hat{\Psi}^\dagger_{\bar{s}}(r,\theta)\hat{\Psi}_s(r,\theta)\rangle\\ &= \frac{i\hbar^2}{2}\sum_s s S_s \partial_\theta S^*_s\\ &= \frac{i\hbar^2}{2}\left(S_+\partial_\theta S^*_+ - S_-\partial_\theta S^*_-\right)\\ &= \frac{i\hbar^2}{2}\left(S_+\partial_\theta S^*_+ - S^*_+\partial_\theta S_+\right),\end{aligned} \tag{A.7}$$

where $\bar{s} = -s$, $S_s \equiv \langle \hat{\Psi}^\dagger_s(r,\theta)\hat{\Psi}_{\bar{s}}(r,\theta)\rangle$, and $S_{\bar{s}} \equiv \langle \hat{\Psi}^\dagger_{\bar{s}}(r,\theta)\hat{\Psi}_s(r,\theta)\rangle = S^*_s$.

Consider next the denominator of the integrand in Eq. (A.1). With

$$S_x(r,\theta) \equiv \langle \hat{S}_x(r,\theta)\rangle = \frac{\hbar}{2}\sum_{ss'} \hat{\sigma}^x_{ss'}\langle \hat{\Psi}^\dagger_s(r,\theta)\hat{\Psi}_{s'}(r,\theta)\rangle, \tag{A.8a}$$

$$S_y(r,\theta) \equiv \langle \hat{S}_y(r,\theta)\rangle = \frac{\hbar}{2}\sum_{ss'} \hat{\sigma}^y_{ss'}\langle \hat{\Psi}^\dagger_s(r,\theta)\hat{\Psi}_{s'}(r,\theta)\rangle, \tag{A.8b}$$

and using Eq. (A.5), the denominator in the integrand is

$$
\begin{aligned}
|\boldsymbol{S}_\perp(r,\theta)|^2 &= |\boldsymbol{z}\times\boldsymbol{S}(r,\theta)|^2\\
&= S_x(r,\theta)^2 + S_y(r,\theta)^2\\
&= \frac{\hbar^2}{4}\sum_{s_1s_2s_3s_4}(1-\delta_{s_1s_2})(1-\delta_{s_3s_4})\langle\hat\Psi^\dagger_{s_1}(r,\theta)\hat\Psi_{s_2}(r,\theta)\rangle\langle\hat\Psi^\dagger_{s_3}(r,\theta)\hat\Psi_{s_4}(r,\theta)\rangle\\
&-\frac{\hbar^2}{4}\sum_{s_1s_2s_3s_4}s_2s_4(1-\delta_{s_1s_2})(1-\delta_{s_3s_4})\langle\hat\Psi^\dagger_{s_1}(r,\theta)\hat\Psi_{s_2}(r,\theta)\rangle\langle\hat\Psi^\dagger_{s_3}(r,\theta)\hat\Psi_{s_4}(r,\theta)\rangle\\
&= \frac{\hbar^2}{4}\sum_{s_1\ldots s_4}(1-\delta_{s_1s_2})(1-\delta_{s_3s_4})(1-s_2s_4)\langle\hat\Psi^\dagger_{s_1}(r,\theta)\hat\Psi_{s_2}(r,\theta)\rangle\langle\hat\Psi^\dagger_{s_3}(r,\theta)\hat\Psi_{s_4}(r,\theta)\rangle\\
&= \frac{\hbar^2}{2}\sum_{s_1\ldots s_4}(1-\delta_{s_1s_2})(1-\delta_{s_3s_4})(1-\delta_{s_2s_4})\langle\hat\Psi^\dagger_{s_1}(r,\theta)\hat\Psi_{s_2}(r,\theta)\rangle\langle\hat\Psi^\dagger_{s_3}(r,\theta)\hat\Psi_{s_4}(r,\theta)\rangle\\
&= \frac{\hbar^2}{2}\sum_{s}\langle\hat\Psi^\dagger_{s}(r,\theta)\hat\Psi_{\bar s}(r,\theta)\rangle\langle\hat\Psi^\dagger_{\bar s}(r,\theta)\hat\Psi_{s}(r,\theta)\rangle\\
&= \frac{\hbar^2}{2}\sum_{s}S_sS_{\bar s}\\
&= \frac{\hbar^2}{2}(S_+S_- + S_-S_+)\\
&= \hbar^2\,|S_+|^2
\end{aligned}
\tag{A.9}
$$

where we have used the fact that $(1-s_2s_4) = 2(1-\delta_{s_2s_4})$, and in the last step bore in mind that $S_- = S_+^*$ and $S_\pm$ are not operators, they are expectation values.

Now, with both Eq. (A.7) and Eq. (A.9), the chirality in Eq. (A.1) becomes

$$
\begin{aligned}
C_z(r) &= \frac{i}{4\pi}\int_0^{2\pi}d\theta\,\frac{\left(S_+\partial_\theta S_+^* - S_+^*\partial_\theta S_+\right)}{|S_+|^2}\\
&= \frac{1}{2\pi}\int_0^{2\pi}d\theta\, j_{\mathrm{spin}}(r,\theta),
\end{aligned}
\tag{A.10}
$$

where

$$
j_{\mathrm{spin}}(r,\theta) = \frac{i}{2\,|S_+|^2}\,\left(S_+\partial_\theta S_+^* - S_+^*\partial_\theta S_+\right) \tag{A.11}
$$

takes the form of a current and is called the chiral spin current density.

A.2 Chirality in a QD

In this section we evaluate the chirality (Eq. (3.6)) of a state of the form

$$|\psi\rangle = \frac{1}{\sqrt{2}}(|L_z\, S_z\rangle + \gamma|L'_z\, S'_z\rangle), \tag{A.12}$$

where $|L_z\, S_z\rangle$ and $|L'_z\, S'_z\rangle$ can be either SP eigenstates of the QD or fully interacting N-particle eigenstates.

The chirality is written here for reference:

$$C_z(r) = \frac{i}{4\pi}\int_0^{2\pi} d\theta\, \frac{S_+\partial_\theta S_+^* - S_+^*\partial_\theta S_+}{|S_+|^2} \tag{A.13}$$

Consider the first term $S_+\partial_\theta S_+^*$ in the numerator of the integrand above. Using the definitions of the field operators $\hat{\Psi}_\sigma^{(\dagger)}(r,\theta)$ in Eq. (3.2), and the definition of the single-particle orbital wave function in position space in Eq. (2.5), we have

$$\begin{aligned}
S_+\partial_\theta S_+^* &\equiv \langle\hat{\Psi}_\uparrow^\dagger(r,\theta)\hat{\Psi}_\downarrow(r,\theta)\rangle\partial_\theta\langle\hat{\Psi}_\downarrow^\dagger(r,\theta)\hat{\Psi}_\uparrow(r,\theta)\rangle \\
&= \sum_{n_1m_1n_2m_2} \phi_{n_1m_1}^*(r,\theta)\,\phi_{n_2m_2}(r,\theta)\,\langle\hat{c}_{n_1m_1\uparrow}^\dagger\hat{c}_{n_2m_2\downarrow}\rangle \\
&\qquad\times\partial_\theta \sum_{n_3m_3n_4m_4} \phi_{n_3m_3}^*(r,\theta)\,\phi_{n_4m_4}(r,\theta)\,\langle\hat{c}_{n_3m_3\downarrow}^\dagger\hat{c}_{n_4m_4\uparrow}\rangle \\
&= \sum_{\substack{n_1m_1n_2m_2\\ n_3m_3n_4m_4}} \phi_{n_1m_1}^*(r,\theta)\,\phi_{n_2m_2}(r,\theta)\;\partial_\theta\left(\phi_{n_3m_3}^*(r,\theta)\,\phi_{n_4m_4}(r,\theta)\right) \\
&\qquad\times\langle\hat{c}_{n_1m_1\uparrow}^\dagger\hat{c}_{n_2m_2\downarrow}\rangle\langle\hat{c}_{n_3m_3\downarrow}^\dagger\hat{c}_{n_4m_4\uparrow}\rangle \\
&= i\sum_{\substack{n_1m_1\cdots\\ \cdots n_4m_4}} ((n_4-m_4)-(n_3-m_3))\,\phi_{n_1m_1}^*(r,\theta)\,\phi_{n_2m_2}(r,\theta)\,\phi_{n_3m_3}^*(r,\theta)\,\phi_{n_4m_4}(r,\theta) \\
&\qquad\times\langle\hat{c}_{n_1m_1\uparrow}^\dagger\hat{c}_{n_2m_2\downarrow}\rangle\langle\hat{c}_{n_3m_3\downarrow}^\dagger\hat{c}_{n_4m_4\uparrow}\rangle.
\end{aligned} \tag{A.14}$$

Similarly, the second term $S_+^* \partial_\theta S_+$ in the numerator of the integrand in Eq. (A.13) is

$$\begin{aligned} S_+^* \partial_\theta S_+ &= i \sum_{\substack{n_1 m_1 \ldots \\ \ldots n_4 m_4}} \left((n_4 - m_4) - (n_3 - m_3)\right) \phi^*_{n_1 m_1}(r,\theta)\, \phi_{n_2 m_2}(r,\theta)\, \phi^*_{n_3 m_3}(r,\theta)\, \phi_{n_4 m_4}(r,\theta) \\ &\qquad \times \langle \hat{c}^\dagger_{n_1 m_1 \downarrow} \hat{c}_{n_2 m_2 \uparrow} \rangle \langle \hat{c}^\dagger_{n_3 m_3 \uparrow} \hat{c}_{n_4 m_4 \downarrow} \rangle \\ &= i \sum_{\substack{n_1 m_1 \ldots \\ \ldots n_4 m_4}} \left((n_2 - m_2) - (n_1 - m_1)\right) \phi^*_{n_1 m_1}(r,\theta)\, \phi_{n_2 m_2}(r,\theta)\, \phi^*_{n_3 m_3}(r,\theta)\, \phi_{n_4 m_4}(r,\theta) \\ &\qquad \times \langle \hat{c}^\dagger_{n_1 m_1 \uparrow} \hat{c}_{n_2 m_2 \downarrow} \rangle \langle \hat{c}^\dagger_{n_3 m_3 \downarrow} \hat{c}_{n_4 m_4 \uparrow} \rangle, \end{aligned} \tag{A.15}$$

where in the last line above we have made a change of indices in the sum. Then

$$\begin{aligned} S_+ \partial_\theta S_+^* - S_+^* \partial_\theta S_+ = i \sum_{\substack{n_1 m_1 \ldots \\ \ldots n_4 m_4}} &\left((n_4 - m_4) - (n_3 - m_3) - (n_2 - m_2) + (n_1 - m_1)\right) \\ \times\ &\phi^*_{n_1 m_1}(r,\theta)\, \phi_{n_2 m_2}(r,\theta)\, \phi^*_{n_3 m_3}(r,\theta)\, \phi_{n_4 m_4}(r,\theta)\, \langle \hat{c}^\dagger_{n_1 m_1 \uparrow} \hat{c}_{n_2 m_2 \downarrow} \rangle \langle \hat{c}^\dagger_{n_3 m_3 \downarrow} \hat{c}_{n_4 m_4 \uparrow} \rangle. \end{aligned} \tag{A.16}$$

For the state in Eq. (A.12),

$$\begin{aligned} \langle \hat{c}^\dagger_{nm\uparrow} \hat{c}_{n'm'\downarrow} \rangle &= \frac{1}{2} \Big(\left(\langle L_z\, S_z| + \gamma^* \langle L'_z\, S'_z|\right) \hat{c}^\dagger_{nm\uparrow} \hat{c}_{n'm'\downarrow} \left(|L_z\, S_z\rangle + \gamma |L'_z\, S'_z\rangle\right) \Big) \\ &= \frac{1}{2} \Bigg(\langle L_z\, S_z| \hat{c}^\dagger_{nm\uparrow} \hat{c}_{n'm'\downarrow} |L_z\, S_z\rangle + \gamma \langle L_z\, S_z|\, \hat{c}^\dagger_{nm\uparrow} \hat{c}_{n'm'\downarrow} |L'_z\, S'_z\rangle \\ &\qquad + \gamma^* \langle L'_z\, S'_z|\, \hat{c}^\dagger_{nm\uparrow} \hat{c}_{n'm'\downarrow} |L_z\, S_z\rangle + |\gamma|^2 \langle L'_z\, S'_z|\, \hat{c}^\dagger_{nm\uparrow} \hat{c}_{n'm'\downarrow} |L'_z\, S'_z\rangle \Bigg). \end{aligned} \tag{A.17}$$

We can generally define the QD eigenstate $|L_z\, S_z\rangle$ as

$$|L_z\, S_z\rangle = \sum_i \alpha_i |l\, s\rangle_i, \tag{A.18}$$

where $|l\, s\rangle$ is an antisymmetric N-particle state. Furthermore, the quantum numbers L_z and S_z of the QD eigenstate are preserved in this superposition. (This superposition of antisymmetric N-particle states is due to either the Coulomb interaction between the particles in the QD, or any spin correlations which can arise by requiring that the total spin S of the QD eigenstate be a good quantum number (see Ref. [117]), either of which conserves L_z and S_z.) Therefore, we have

$$l = L_z, \tag{A.19a}$$

$$s = S_z. \tag{A.19b}$$

When acting on this state, the operator $\hat{c}_{nm\sigma}$ removes a particle of spin σ from the $[n\,m]$ orbital while maintaining the antisymmetry of the state. This lowers the orbital angular momentum of the state $|l\,s\rangle$ by a value of $(n-m)$ and also lowers the spin angular momentum by a value of σ. Effectively,

$$\hat{c}_{nm\sigma}|l\,s\rangle_i = \sum_j a^i_j\,|l-(n-m), s-\sigma\rangle_j, \tag{A.20}$$

where the states in the sum over j are $(N-1)$-particle states. Similarly,

$$_i\langle l\,s|\hat{c}^\dagger_{nm\sigma} = \sum_j (a^i_j)^*\,{}_j\langle l-(n-m), s-\sigma|. \tag{A.21}$$

The first term and the last term in the final line of Eq. (A.17) are each zero because $\hat{c}^\dagger_{nm\uparrow}\hat{c}_{n'm'\downarrow}$ does not conserve spin. The first non-zero term is

$$\begin{aligned}
\langle L_z\,S_z|\,\hat{c}^\dagger_{nm\uparrow}\hat{c}_{n'm'\downarrow}\,|L'_z\,S'_z\rangle &= \sum_{ij}\alpha^*_i\alpha_j\,{}_i\langle l\,s|\hat{c}^\dagger_{nm\uparrow}\hat{c}_{n'm'\downarrow}|l'\,s'\rangle_j \\
&= \sum_{ijkl}\alpha^*_i\alpha_j(a^i_k)^*a^j_l\,{}_k\langle l-(n-m), s-\tfrac{1}{2}|l'-(n'-m'), s'+\tfrac{1}{2}\rangle_l \\
&= \sum_{ijkl}\alpha^*_i\alpha_j(a^i_k)^*a^j_l\,\delta_{l-(n-m),l'-(n'-m')}\delta_{s-\frac{1}{2},s'+\frac{1}{2}}\delta_{k,l} \\
&= \sum_{ijk}\alpha^*_i\alpha_j(a^i_k)^*a^j_k\,\delta_{l-l',(n-m)-(n'-m')}\delta_{s-s',1}
\end{aligned} \tag{A.22}$$

Similarly, the second non-zero term is

$$\langle L'_z\,S'_z|\,\hat{c}^\dagger_{nm\uparrow}\hat{c}_{n'm'\downarrow}\,|L_z\,S_z\rangle = \sum_{ijk}\beta^*_i\beta_j(b^i_k)^*b^j_k\,\delta_{l'-l,(n-m)-(n'-m')}\delta_{s'-s,1} \tag{A.23}$$

Eq. (A.17) becomes

$$\begin{aligned}
\langle\hat{c}^\dagger_{nm\uparrow}\hat{c}_{n'm'\downarrow}\rangle = \frac{1}{2}\sum_{ijk}\big(&\gamma\alpha^*_i\alpha_j(a^i_k)^*a^j_k\,\delta_{l-l',(n-m)-(n'-m')}\delta_{s-s',1} \\
&+\gamma^*\,\beta^*_i\beta_j(b^i_k)^*b^j_k\,\delta_{l'-l,(n-m)-(n'-m')}\delta_{s'-s,1}\big).
\end{aligned} \tag{A.24}$$

Similarly,

$$
\begin{aligned}
\langle \hat{c}^{\dagger}_{nm\downarrow}\hat{c}_{n'm'\uparrow}\rangle = \frac{1}{2}\sum_{ijk}\big(&\gamma\alpha_i^*\alpha_j(a_k^i)^*a_k^j\,\delta_{l-l',(n-m)-(n'-m')}\delta_{s'-s,1} \\
&+\gamma^*\,\beta_i^*\beta_j(b_k^i)^*b_k^j\,\delta_{l'-l,(n-m)-(n'-m')}\delta_{s-s',1}\big).
\end{aligned}
\tag{A.25}
$$

Then

$$
\begin{aligned}
\langle \hat{c}^{\dagger}_{n_1m_1\uparrow}\hat{c}_{n_2m_2\downarrow}\rangle\langle \hat{c}^{\dagger}_{n_3m_3\downarrow}\hat{c}_{n_4m_4\uparrow}\rangle &= \frac{1}{4}\sum_{ijkpqr}\big(\gamma\alpha_i^*\alpha_j(a_k^i)^*a_k^j\,\delta_{l-l',(n_1-m_1)-(n_2-m_2)}\delta_{s-s',1} \\
&\quad+\gamma^*\,\beta_i^*\beta_j(b_k^i)^*b_k^j\,\delta_{l'-l,(n_1-m_1)-(n_2-m_2)}\delta_{s'-s,1}\big) \\
&\quad\times\big(\gamma\alpha_p^*\alpha_q(a_r^p)^*a_r^q\,\delta_{l-l',(n_3-m_3)-(n_4-m_4)}\delta_{s'-s,1} \\
&\quad+\gamma^*\,\beta_p^*\beta_q(b_r^p)^*b_r^q\,\delta_{l'-l,(n_3-m_3)-(n_4-m_4)}\delta_{s-s',1}\big) \\
&= \frac{|\gamma|^2}{4}\sum_{ijkpqr}\big(\alpha_i^*\alpha_j(a_k^i)^*a_k^j\beta_p^*\beta_q(b_r^p)^*b_r^q \\
&\quad\times\delta_{l-l',(n_1-m_1)-(n_2-m_2)}\delta_{l'-l,(n_3-m_3)-(n_4-m_4)}\delta_{s-s',1} \\
&\quad+\alpha_p^*\alpha_q(a_r^p)^*a_r^q\beta_i^*\beta_j(b_k^i)^*b_k^j \\
&\quad\times\delta_{l'-l,(n_1-m_1)-(n_2-m_2)}\delta_{l-l',(n_3-m_3)-(n_4-m_4)}\delta_{s'-s,1}\big) \\
&= \frac{|\gamma|^2}{4}\sum_{ijkpqr}\alpha_i^*\alpha_j(a_k^i)^*a_k^j\beta_p^*\beta_q(b_r^p)^*b_r^q \\
&\quad\times\big(\delta_{l-l',(n_1-m_1)-(n_2-m_2)}\delta_{l'-l,(n_3-m_3)-(n_4-m_4)}\delta_{s-s',1} \\
&\quad+\delta_{l'-l,(n_1-m_1)-(n_2-m_2)}\delta_{l-l',(n_3-m_3)-(n_4-m_4)}\delta_{s'-s,1}\big) \\
&= \frac{|\gamma|^2}{4}\sum_{ijkpqr}A_{ijkpqr}\delta_{(n_1-m_1)-(n_2-m_2),(n_4-m_4)-(n_3-m_3)} \\
&\quad\times\big(\delta_{l-l',(n_1-m_1)-(n_2-m_2)}\delta_{s-s',1}+\delta_{l'-l,(n_1-m_1)-(n_2-m_2)}\delta_{s'-s,1}\big)
\end{aligned}
\tag{A.26}
$$

where in the second line two of the four terms in the product are zero by the spin-conserving Kronecker deltas, in the second-to-last line we have made a change of indices in the second term of the sum, and finally $A_{ijkpqr} \equiv \alpha_i^*\alpha_j(a_k^i)^*a_k^j\beta_p^*\beta_q(b_r^p)^*b_r^q$.

Inserting Eq. (A.26) into Eq. (A.16) gives

$$\begin{aligned}
S_+\partial_\theta S_+^* - S_+^*\partial_\theta S_+ &= \frac{i|\gamma|^2}{4}\sum_{ijkpqr} A_{ijkpqr} \sum_{\substack{n_1m_1\ldots\\ \ldots n_4m_4}} ((n_4-m_4)-(n_3-m_3)-(n_2-m_2)+(n_1-m_1)) \\
&\quad \times\ \phi^*_{n_1m_1}(r,\theta)\,\phi_{n_2m_2}(r,\theta)\,\phi^*_{n_3m_3}(r,\theta)\,\phi_{n_4m_4}(r,\theta)\,\delta_{(n_1-m_1)-(n_2-m_2),(n_4-m_4)-(n_3-m_3)} \\
&\quad \times\ \big(\delta_{l-l',(n_1-m_1)-(n_2-m_2)}\delta_{s-s',1} + \delta_{l'-l,(n_1-m_1)-(n_2-m_2)}\delta_{s'-s,1}\big) \\
&= \frac{i|\gamma|^2}{2}\sum_{ijkpqr} A_{ijkpqr} \sum_{\substack{n_1m_1\ldots\\ \ldots n_4m_4}} ((n_1-m_1)-(n_2-m_2)) \\
&\quad \times\ \phi^*_{n_1m_1}(r,\theta)\,\phi_{n_2m_2}(r,\theta)\,\phi^*_{n_3m_3}(r,\theta)\,\phi_{n_4m_4}(r,\theta)\,\delta_{(n_1-m_1)-(n_2-m_2),(n_4-m_4)-(n_3-m_3)} \\
&\quad \times\ \big(\delta_{l-l',(n_1-m_1)-(n_2-m_2)}\delta_{s-s',1} + \delta_{l'-l,(n_1-m_1)-(n_2-m_2)}\delta_{s'-s,1}\big),
\end{aligned} \tag{A.27}$$

where in the last line we have taken advantage of $\delta_{(n_1-m_1)-(n_2-m_2),(n_4-m_4)-(n_3-m_3)}$.

Now consider the denominator of the integrand in Eq. (A.13). Using Eq. (A.26), we have

$$\begin{aligned}
|S_+|^2 &= \sum_{\substack{n_1m_1\ldots\\ \ldots n_4m_4}} \phi^*_{n_1m_1}(r,\theta)\,\phi_{n_2m_2}(r,\theta)\,\phi^*_{n_3m_3}(r,\theta)\,\phi_{n_4m_4}(r,\theta)\,\langle \hat{c}^\dagger_{n_1m_1\uparrow}\hat{c}_{n_2m_2\downarrow}\rangle\langle \hat{c}^\dagger_{n_3m_3\downarrow}\hat{c}_{n_4m_4\uparrow}\rangle \\
&= \frac{|\gamma|^2}{4}\sum_{ijkpqr} A_{ijkpqr} \sum_{\substack{n_1m_1\ldots\\ \ldots n_4m_4}} \delta_{(n_1-m_1)-(n_2-m_2),(n_4-m_4)-(n_3-m_3)}\phi^*_{n_1m_1}(r,\theta)\,\phi_{n_2m_2}(r,\theta) \\
&\qquad \times \phi^*_{n_3m_3}(r,\theta)\,\phi_{n_4m_4}(r,\theta)\,\big(\delta_{l-l',(n_1-m_1)-(n_2-m_2)}\delta_{s-s',1} + \delta_{l'-l,(n_1-m_1)-(n_2-m_2)}\delta_{s'-s,1}\big).
\end{aligned} \tag{A.28}$$

To evaluate the integrand in Eq. (A.13) we must consider the cases of the spins of the states (s and s'). If $s - s' = 1$, then by the Kronecker delta $\delta_{l-l',(n_1-m_1)-(n_2-m_2)}$ we have $((n_1-m_1)-(n_2-m_2)) = l - l'$ (the term with $\delta_{s'-s,1}$ in both Eq. (A.27) and Eq. (A.28) is zero in this case), and the integrand reduces to

$$\frac{S_+\partial_\theta S_+^* - S_+^*\partial_\theta S_+}{|S_+|^2} = 2i(l-l'). \tag{A.29}$$

If $s' - s = 1$ (i.e. $s - s' = -1$), then we have $((n_1-m_1)-(n_2-m_2)) = l' - l$, and the integrand reduces to

$$\begin{aligned}
\frac{S_+\partial_\theta S_+^* - S_+^*\partial_\theta S_+}{|S_+|^2} &= 2i(l'-l) \\
&= -2i(l-l').
\end{aligned} \tag{A.30}$$

We can account for each case by expressing the integrand as

$$\frac{S_+\partial_\theta S_+^* - S_+^*\partial_\theta S_+}{|S_+|^2} = 2i(l-l')(s-s')\delta_{|s-s'|,1}. \tag{A.31}$$

In evaluating the integral in Eq. (A.13), the chirality takes the form

$$\begin{aligned} C_z(r) &= \frac{i}{4\pi}\int_0^{2\pi} d\theta\,\frac{S_+\partial_\theta S_+^* - S_+^*\partial_\theta S_+}{|S_+|^2} \\ &= -\frac{1}{2\pi}\int_0^{2\pi} d\theta\,(l-l')(s-s')\delta_{|s-s'|,1} \\ &= (l'-l)(s-s')\delta_{|s-s'|,1} \\ &= (L_z'-L_z)(S_z-S_z')\delta_{|S_z-S_z'|,1}, \end{aligned} \tag{A.32}$$

where in the last line we have used Eq. (A.19). Note that the chirality is independent of the phase γ between the two 'base' QD eigenstates in Eq. (A.12). Additionally, this expression is also independent of r, and so we can write the chirality of a state of the form given in Eq. (A.12) as

$$C_z = (L_z'-L_z)(S_z-S_z')\delta_{|S_z-S_z'|,1}, \tag{A.33}$$

which agrees with Eq. (3.7) in this disseration.

A.3 General Winding State

The winding state in Eq. (A.12) can be generalized to

$$\begin{aligned} |QC\rangle = \frac{1-c}{2\sqrt{2}}&(|L_z,S_z\rangle + \gamma q\,|L_z',S_z'\rangle) \\ &+ \frac{1+c}{2\sqrt{2}}(|L_z,S_z'\rangle + \gamma' q\,|L_z',S_z\rangle), \end{aligned} \tag{A.34}$$

where $L_z \neq L_z'$, $|S_z - S_z'| = 1$, $c \equiv C/|C|$, $q \equiv Q/|Q|$, and $\gamma^{(\prime)}$ is a general coefficient. This state takes into account four different types of winding states. For example, if the winding of the spin density field in position space is *counter-clockwise* along a closed curve about the centre of the QD, then C is defined to be some positive integer (the magnitude of which depends on the difference in orbital angular momentum of the states, $L_z' - L_z$). Magnitude aside, let us write C as + to denote the counter-clockwise winding. For a counter-clockwise winding, we have that $c = C/|C| = 1$.

Furthermore, if the topological charge is 1, then $q = Q/|Q| = 1$, and we write Q as $+$. In this case, Eq. (A.34) becomes

$$\begin{aligned} |QC\rangle \to |++\rangle &= \frac{1-1}{2\sqrt{2}}(|L_z, S_z\rangle + \gamma\, |L'_z, S'_z\rangle) \\ &\quad + \frac{1+1}{2\sqrt{2}}(|L_z, S'_z\rangle + \gamma'\, |L'_z, S_z\rangle) \\ &= \frac{1}{\sqrt{2}}(|L_z, S'_z\rangle + \gamma'\, |L'_z, S_z\rangle). \end{aligned} \tag{A.35}$$

This state is of the same form as that in Eq. (A.12), and thus its chirality can be defined using Eq. (A.33) to be

$$C_z = (L'_z - L_z)(S'_z - S_z)\delta_{|S_z - S'_z|,1}. \tag{A.36}$$

Similarly, in the case of a winding state with a *clockwise* winding of the spin density field along the same closed curve and an opposite topological charge to the previous example, we have $C \to -$ and $Q \to -1$. Then $c = -1$ and $q = -1$, and Eq. (A.34) becomes

$$\begin{aligned} |QC\rangle \to |--\rangle &= \frac{1-(-1)}{2\sqrt{2}}(|L_z, S_z\rangle - \gamma\, |L'_z, S'_z\rangle) \\ &\quad + \frac{1+(-1)}{2\sqrt{2}}(|L_z, S'_z\rangle - \gamma'\, |L'_z, S_z\rangle) \\ &= \frac{1}{\sqrt{2}}(|L_z, S_z\rangle - \gamma\, |L'_z, S'_z\rangle). \end{aligned} \tag{A.37}$$

Since the chirality in Eq. (A.33) is independent of the phase $(-\gamma)$ its chirality is

$$C_z = (L'_z - L_z)(S_z - S'_z)\delta_{|S_z - S'_z|,1}. \tag{A.38}$$

Note that in comparing Eq. (A.36) and Eq. (A.38) it is clear that these two states defined in Eq. (A.35) and Eq. (A.37) have opposite chirality. (The expression for chirality in Eq. (A.33) does *not* distinguish the topological charge of each state.)

The remaining two cases are $C \to +$ and $Q \to -1$ with $c = 1$ and $q = -1$, and $C \to -$ and $Q \to 1$ with $c = -1$ and $q = 1$. Then the state

$$|QC\rangle \to |-+\rangle = \frac{1}{\sqrt{2}}(|L_z, S'_z\rangle - \gamma'\, |L'_z, S_z\rangle) \tag{A.39}$$

has a chirality of

$$C_z = (L'_z - L_z)(S'_z - S_z)\delta_{|S_z - S'_z|,1}, \tag{A.40}$$

just like state $|++\rangle$. The state

$$|QC\rangle \rightarrow |+-\rangle = \frac{1}{\sqrt{2}}(|L_z, S_z\rangle + \gamma\,|L'_z, S'_z\rangle) \tag{A.41}$$

has a chirality of

$$C_z = (L'_z - L_z)(S_z - S'_z)\delta_{|S_z - S'_z|,1}, \tag{A.42}$$

just like state $|--\rangle$. Note the four states $|++\rangle$, $|--\rangle$, $|-+\rangle$, and $|+-\rangle$ are all orthogonal to each other.

Appendix B

Diagonalization of the Spin-Orbit Hamiltonian

B.1 Diagonalization of H_{SO}

The SO Hamiltonian is the sum of the Rashba SO Hamiltonian in Eq. (3.12) and the linear part of the Dresselhaus SO Hamiltonian in Eq. (3.13), and is written here again for reference:

$$\hat{H}_{SO} = \frac{\alpha_R}{\hbar}\left(\hat{\sigma}_x \hat{\mathrm{P}}_y - \hat{\sigma}_y \hat{\mathrm{P}}_x\right) - \frac{\beta_D}{\hbar}\left(\hat{\sigma}_x \hat{\mathrm{P}}_x - \hat{\sigma}_y \hat{\mathrm{P}}_y\right). \tag{B.1}$$

It is treated perturbatively and is diagonalized in the subspace of the four lowest-lying states where merons can form. Eq. (B.1) can be expressed in a more convenient form,

$$\begin{aligned}\hat{H}_{SO} = \lambda\Big(&\hat{\sigma}_+ \left[\left(1+\tfrac{1}{\nu}\right)\left(\alpha_R \hat{a} - i\beta_D \hat{a}^\dagger\right) + \left(1-\tfrac{1}{\nu}\right)\left(-\alpha_R \hat{b}^\dagger + i\beta_D \hat{b}\right)\right] \\ &+ \hat{\sigma}_- \left[\left(1+\tfrac{1}{\nu}\right)\left(\alpha_R \hat{a}^\dagger + i\beta_D \hat{a}\right) + \left(1-\tfrac{1}{\nu}\right)\left(-\alpha_R \hat{b} - i\beta_D \hat{b}^\dagger\right)\right]\Big).\end{aligned} \tag{B.2}$$

Note $\hat{H}_{SO} = \hat{H}_{SO}^\dagger$. To obtain this form we express the Pauli spin matrices in terms of spin raising and lowering operators, $\hat{\sigma}_x = (\hat{\sigma}_+ + \hat{\sigma}_-)/2$, $\hat{\sigma}_y = i(\hat{\sigma}_- - \hat{\sigma}_+)/2$. With $\hat{\mathrm{P}}_x = \hat{\mathrm{p}}_x - (eB)/(2c)\hat{y}$ and $\hat{\mathrm{P}}_y = \hat{\mathrm{p}}_y + (eB)/(2c)\hat{x}$, we can rewrite the canonical momentum in terms of the Bose annihilation and creation operators, a, b, $a^\dagger$, $b^\dagger$ using the following:

$$\hat{x} = l_0(a^\dagger + a + b^\dagger + b)/\sqrt{2}, \tag{B.3a}$$

$$\hat{y} = -i\, l_0(a^\dagger - a - b^\dagger + b)/\sqrt{2}, \tag{B.3b}$$

$$\hat{p_x} = i\lambda(a^\dagger - a + b^\dagger - b), \tag{B.3c}$$

$$\hat{p_y} = \lambda(a^\dagger + a - b^\dagger - b), \tag{B.3d}$$

where $\lambda = 1/(2\sqrt{2}l_0)$ and $\nu = \sqrt{1 + 4\omega_0^2/\omega_c^2}$.

Note that the linear SO interaction contains orbital and spin raising and lowering operators to linear order only. Therefore it can only be diagonalized in a subspace of states which contain orbital angular momentum states with L_z values that differ by 1 only, and spin angular momentum states with S_z values that differ by 1 only. (This condition on the difference in spin is compliant with the winding criteria in Eq. (3.7)). The SO interaction should, in principle, break the degeneracy of meron states in some of the four-fold degenerate subspaces found in the $N = 1$ and $N = 3$ systems, where $|L_z - L'_z| = 1$ and S_z values are limited to $\pm 1/2$. Using the form of the general winding states in Eq. (3.8), these meron states can be expressed as

(B.4)

where $C = \pm 1$ and $Q = \pm 1$.

Eq. (B.1) is diagonalized in the subspace of the four lowest-lying $\hat{H}_{QD}$ eigenstates, which in cases studied in this dissertation can be generalized to

$$\begin{aligned} |0\rangle &\equiv \left|L_z,\ \ S_z = \tfrac{1}{2}\right\rangle, \\ |1\rangle &\equiv \left|L_z,\ \ S_z = -\tfrac{1}{2}\right\rangle, \\ |2\rangle &\equiv \left|L_z - 1,\ \ S_z = \tfrac{1}{2}\right\rangle, \\ |3\rangle &\equiv \left|L_z - 1,\ \ S_z = -\tfrac{1}{2}\right\rangle. \end{aligned} \tag{B.5}$$

In this basis, the matrix form of $\hat{H}_{SO}$ becomes

$$\hat{H}_{SO} = \begin{pmatrix} 0 & 0 & 0 & H_{03} \\ 0 & 0 & H_{12} & 0 \\ 0 & H_{21} & 0 & 0 \\ H_{30} & 0 & 0 & 0 \end{pmatrix}, \tag{B.6}$$

where

$$H_{03} = -i\beta_D \lambda \left\langle L_z, \tfrac{1}{2} \right| \hat{\sigma}_+ \big(\hat{a}^\dagger \left(1 + \tfrac{1}{\nu}\right) - \hat{b}\left(1 - \tfrac{1}{\nu}\right)\big) \left| L_z - 1, -\tfrac{1}{2} \right\rangle \tag{B.7a}$$

$$H_{12} = \alpha_R \lambda \left\langle L_z, -\tfrac{1}{2} \right| \hat{\sigma}_- \big(\hat{a}^\dagger \left(1 + \tfrac{1}{\nu}\right) - \hat{b}\left(1 - \tfrac{1}{\nu}\right)\big) \left| L_z - 1, \tfrac{1}{2} \right\rangle \tag{B.7b}$$

$$H_{21} = \alpha_R \lambda \left\langle L_z - 1, \tfrac{1}{2} \right| \hat{\sigma}_+ \big(\hat{a} \left(1 + \tfrac{1}{\nu}\right) - \hat{b}^\dagger \left(1 - \tfrac{1}{\nu}\right)\big) \left| L_z, -\tfrac{1}{2} \right\rangle \tag{B.7c}$$

$$H_{30} = i\beta_D \lambda \left\langle L_z - 1, -\tfrac{1}{2} \right| \hat{\sigma}_- \big(\hat{a} \left(1 + \tfrac{1}{\nu}\right) - \hat{b}^\dagger \left(1 - \tfrac{1}{\nu}\right)\big) \left| L_z, \tfrac{1}{2} \right\rangle \tag{B.7d}$$

Since $\hat{H}_{SO}$ is Hermitian, it must be that $H_{03} = H^*_{30}$ and $H_{12} = H^*_{21}$. The coefficients of the $\hat{H}_{QD}$ eigenstates in Eq. (B.5) are real, as are α_R, β_D, λ, and ν, and so we can express the matrix form of $\hat{H}_{SO}$ more succinctly by defining

$$\begin{aligned}\mathcal{E}_+ &\equiv \lambda \left\langle L_z - 1, \tfrac{1}{2}\right| \hat{\sigma}_+\big(\hat{a}\left(1+\tfrac{1}{\nu}\right) - \hat{b}^\dagger\left(1-\tfrac{1}{\nu}\right)\big) \left|L_z, -\tfrac{1}{2}\right\rangle \\ &= \lambda \left\langle L_z, -\tfrac{1}{2}\right| \hat{\sigma}_-\big(\hat{a}^\dagger\left(1+\tfrac{1}{\nu}\right) - \hat{b}\left(1-\tfrac{1}{\nu}\right)\big) \left|L_z - 1, \tfrac{1}{2}\right\rangle\end{aligned} \tag{B.8a}$$

$$\begin{aligned}\mathcal{E}_- &\equiv \lambda \left\langle L_z - 1, -\tfrac{1}{2}\right| \hat{\sigma}_-\big(\hat{a}\left(1+\tfrac{1}{\nu}\right) - \hat{b}^\dagger\left(1-\tfrac{1}{\nu}\right)\big) \left|L_z, \tfrac{1}{2}\right\rangle \\ &= \lambda \left\langle L_z, \tfrac{1}{2}\right| \hat{\sigma}_+\big(\hat{a}^\dagger\left(1+\tfrac{1}{\nu}\right) - \hat{b}\left(1-\tfrac{1}{\nu}\right)\big) \left|L_z - 1, -\tfrac{1}{2}\right\rangle,\end{aligned} \tag{B.8b}$$

or more compactly,

$$\mathcal{E}_\pm \equiv \lambda \left\langle L_z - 1, \pm\tfrac{1}{2}\right| \hat{\sigma}_\pm\big(\hat{a}\left(1+\tfrac{1}{\nu}\right) - \hat{b}^\dagger\left(1-\tfrac{1}{\nu}\right)\big) \left|L_z, \mp\tfrac{1}{2}\right\rangle. \tag{B.9}$$

Then the matrix form of $\hat{H}_{SO}$ becomes

$$\hat{H}_{SO} = \begin{pmatrix} 0 & 0 & 0 & -i\beta_D\mathcal{E}_- \\ 0 & 0 & \alpha_R\mathcal{E}_+ & 0 \\ 0 & \alpha_R\mathcal{E}_+ & 0 & 0 \\ i\beta_D\mathcal{E}_- & 0 & 0 & 0 \end{pmatrix} \tag{B.10}$$

The effect of the SO interaction on the meron states in Eq. (B.4) can be determined by taking the expectation value of $\hat{H}_{SO}$ with these states, $\langle QC|\,\hat{H}_{SO}\,|QC\rangle$, which results in the four unique perturbation energies

$$\mathrm{E}_{QC} = \frac{Q}{2}\big(\alpha_R\mathcal{E}_+(1+C) + \beta_D\mathcal{E}_-(1-C)\big). \tag{B.11}$$

B.2 Diagonalization of Effective Hamiltonian $H = H_{QD} + H_{SO}$

When the SO interaction is included in the model the total Hamiltonian becomes $\hat{H} = \hat{H}_{QD} + \hat{H}_{SO}$, where $\hat{H}_{QD}$ is described in Eq. (2.2a) and $\hat{H}_{SO}$ is described in Eq. (B.1). As in the previous section, $\hat{H}$ is diagonalized in the subspace containing the four $\hat{H}_{QD}$ eigenstates listed in Eq. (B.5). The matrix form of $\hat{H}$ becomes

$$\hat{H} = \begin{pmatrix} e_0 & 0 & 0 & -i\beta_D\mathcal{E}_- \\ 0 & e_1 & \alpha_R\mathcal{E}_+ & 0 \\ 0 & \alpha_R\mathcal{E}_+ & e_2 & 0 \\ i\beta_D\mathcal{E}_- & 0 & 0 & e_3 \end{pmatrix}, \tag{B.12}$$

where e_i are the energies of the H_{QD} eigenstates $|i\rangle$, and $\mathcal{E}_\pm$ is defined in Eq. (B.9) above. The energy eigenvalues of $\hat{H}$ are

$$E_0 = \frac{1}{2}\left(e_0 + e_3 - \sqrt{(e_0 - e_3)^2 + 4\beta_D^2\,\mathcal{E}_-^2}\right), \tag{B.13a}$$

$$E_1 = \frac{1}{2}\left(e_1 + e_2 - \sqrt{(e_1 - e_2)^2 + 4\alpha_R^2\,\mathcal{E}_+^2}\right), \tag{B.13b}$$

$$E_2 = \frac{1}{2}\left(e_1 + e_2 + \sqrt{(e_1 - e_2)^2 + 4\alpha_R^2\,\mathcal{E}_+^2}\right), \tag{B.13c}$$

$$E_3 = \frac{1}{2}\left(e_0 + e_3 + \sqrt{(e_0 - e_3)^2 + 4\beta_D^2\,\mathcal{E}_-^2}\right). \tag{B.13d}$$

The eigenstates corresponding to the eigenvalues in Eq. (B.18) are:

$$|\psi_0\rangle = a\,|0\rangle - ib\,|3\rangle, \tag{B.14a}$$

$$|\psi_1\rangle = c\,|1\rangle - d\,|2\rangle, \tag{B.14b}$$

$$|\psi_2\rangle = d\,|1\rangle + c\,|2\rangle, \tag{B.14c}$$

$$|\psi_3\rangle = b\,|0\rangle + ia\,|3\rangle, \tag{B.14d}$$

where, for $B < B^*$,

$$a \equiv \frac{-(E_0 - e_3)}{\sqrt{\beta_D^2\,\mathcal{E}_-^2 + (E_0 - e_3)^2}}, \tag{B.15a}$$

$$b \equiv \frac{\beta_D\,\mathcal{E}_-}{\sqrt{\beta_D^2\,\mathcal{E}_-^2 + (E_0 - e_3)^2}}, \tag{B.15b}$$

$$c \equiv \frac{-(E_1 - e_2)}{\sqrt{\alpha_R^2\,\mathcal{E}_+^2 + (E_1 - e_2)^2}}, \tag{B.15c}$$

$$d \equiv \frac{\alpha_R\,\mathcal{E}_+}{\sqrt{\alpha_R^2\,\mathcal{E}_+^2 + (E_1 - e_2)^2}}. \tag{B.15d}$$

Note that in the single-electron system the degeneracy point $B^* = \infty$ and therefore the coefficients described above are correct for all values of B. In the three-electron system B^* is finite. In the cases investigated in this dissertation, the $\hat{H}_{QD}$ energies e_i of the L_z states are smaller than those of the $L_z - 1$ states when $B < B^*$, however for $B > B^*$ the energies of the L_z states become larger than those of the $L_z - 1$ states.

If $B > B^*$ the coefficients must be expressed as

$$a \equiv \frac{\beta_D\,\mathcal{E}_-}{\sqrt{\beta_D^2\,\mathcal{E}_-^2 + (E_0 - e_0)^2}}, \tag{B.16a}$$

$$b \equiv \frac{-(E_0 - e_0)}{\sqrt{\beta_D^2\,\mathcal{E}_-^2 + (E_0 - e_0)^2}}, \tag{B.16b}$$

$$c \equiv \frac{\alpha_R\,\mathcal{E}_+}{\sqrt{\alpha_R^2\,\mathcal{E}_+^2 + (E_1 - e_1)^2}}, \tag{B.16c}$$

$$d \equiv \frac{-(E_1 - e_1)}{\sqrt{\alpha_R^2\,\mathcal{E}_+^2 + (E_1 - e_1)^2}}. \tag{B.16d}$$

In the absence of SO, i.e. in the limit that both $\alpha_R \to 0$ and $\beta_D \to 0$, when $B < B^*$ the eigenstates $|\psi_0\rangle$, $|\psi_1\rangle$, $|\psi_2\rangle$, and $|\psi_3\rangle$ reduce to $|0\rangle$, $|1\rangle$, $|2\rangle$, and $|3\rangle$, respectively, to within an overall phase. When $B > B^*$ the eigenstates $|\psi_0\rangle$, $|\psi_1\rangle$, $|\psi_2\rangle$, and $|\psi_3\rangle$ reduce to $|3\rangle$, $|2\rangle$, $|1\rangle$, and $|0\rangle$, respectively, to within an overall phase. The energy eigenvalues reduce correspondingly.

In the limit that $B \to B^*$ the eigenstates reduce to the meron states described in Eq. (B.4). Specifically,

$$|\psi_0\rangle \to \frac{1}{\sqrt{2}}\left(|0\rangle - i\,|3\rangle\right) \equiv |Q{=}1, C{=}{-1}\rangle\,, \tag{B.17a}$$

$$|\psi_1\rangle \to \frac{1}{\sqrt{2}}\left(|1\rangle - |2\rangle\right) \equiv |Q{=}{-1}, C{=}1\rangle\,, \tag{B.17b}$$

$$|\psi_2\rangle \to \frac{1}{\sqrt{2}}\left(|1\rangle + |2\rangle\right) \equiv |Q{=}1, C{=}1\rangle\,, \tag{B.17c}$$

$$|\psi_3\rangle \to \frac{1}{\sqrt{2}}\left(|0\rangle + i\,|3\rangle\right) \equiv |Q{=}{-1}, C{=}{-1}\rangle\,. \tag{B.17d}$$

In this degenerate[1] subspace where $e_0 = e_2 \approx e_1 = e_3 \equiv e$, the energy eigenvalues of $\hat{H}$ become

$$E_0 \to e - \beta_D\mathcal{E}_-, \tag{B.18a}$$

$$E_1 \to e - \alpha_R\mathcal{E}_+, \tag{B.18b}$$

$$E_2 \to e + \alpha_R\mathcal{E}_+, \tag{B.18c}$$

$$E_3 \to e + \beta_D\mathcal{E}_-, \tag{B.18d}$$

as expected according to Eq. (B.11).

---

[1] At B^* the L_z and $L_z - 1$ states with the same spin are exactly degenerate. All four states are degenerate to within the Zeeman splitting energy.

B.3 Truncation of N=3 H_{QD} Eigenstates

The eigenstates of the interacting $N = 3$ QD system are expressed as a linear combination of all possible orbital configurations which conserve the quantum numbers of the state (N, L_z, S_z, S^2):

$$|\Psi\rangle = \sum_i c_i \, |S, S_z, L_z, i\rangle \tag{B.19}$$

We use up to 500 three-particle basis states (Slater determinants which are constructed from the single-particle QD states) to diagonalize $\hat{H}_{QD}$ (Eq. (2.2a)), the unperturbed QD. These states are used to calculate the relaxation and decoherence rates when the SO interaction is not included in the model (see Sec. 6.1).

Due to the large superposition of Slater determinants, calculating the relaxation rates in the interacting case is already computationally expensive, however when SO is included as a perturbation it becomes significantly more laborious. In the absence of SO the Redfield tensor contains 16 elements. Expressed as a matrix, it can be diagonalized analytically to obtain the relaxation rate (see Sec. 5.1). This relaxation rate requires the evaluation of a single $\Gamma^{+}_{nmm'n'}$ element (see Eq. (5.7), and Eq. (4.45a)). The states $|n\rangle$, $|m\rangle$, $|m'\rangle$, and $|n'\rangle$ used in $\Gamma^{+}_{nmm'n'}$ are the interacting QD eigenstates, each containing up to $\sim$ 500 basis states.

When SO is included, the number of elements in the Redfield tensor increases to 256. Expressed as a matrix, it is diagonalized numerically to obtain the relaxation rates. In this case the relaxation rate is not determined analytically. For phonon emission only, 96 $\Gamma^{+}_{nmm'n'}$ elements must be evaluated in order to diagonalize the Redfield tensor. Furthermore, the states $|n\rangle$, $|m\rangle$, $|m'\rangle$, and $|n'\rangle$ used in $\Gamma^{+}_{nmm'n'}$ are now the SO states, which are each a superposition of two QD eigenstates.

Most of the basis states which make up the interacting QD eigenstates have a weight that is almost zero. To calculate the relaxation and decoherence rates of the SO states in the three-electron system (Sec. 6.2), we remove these low-weight basis states such that the QD eigenstates retain a probability of 99.9% or more. They are then renormalized for calculating the relaxation and decoherence rates. By truncating the QD eigenstates to within 0.1% of their original weight the basis size is reduced to between approximately 80 and 100 basis states. In other words, almost all of the weight of the eigenstate is found on the first 80 to 100 basis states; the remaining 300

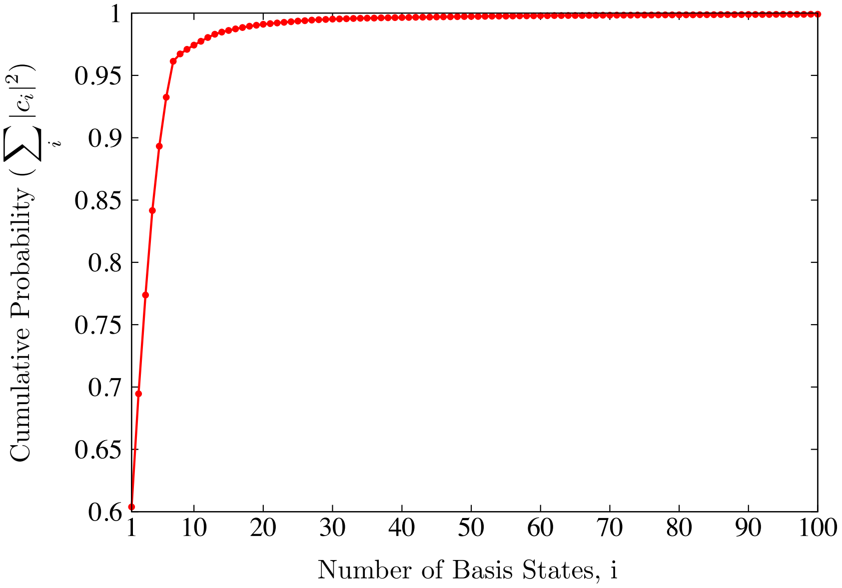

Figure B.1: Cumulative probability of a typical interacting three-electron QD eigenstate (in this case, the $L_z = -1$ ground state) when $\hat{H}_{QD}$ is diagonalized with 500 three-particle basis states (Slater determinants). The majority of the weight of the state (to 0.999 probability) is held within the first 100 basis states.

to 400 basis states contain less than 0.1% of the weight of the state (see Fig. B.1). By truncating the states the numerical processing times required for determining the decay rates are reduced by approximately an order of magnitude. Note that, when using the *truncated* states, the time required to determine the relaxation and decoherence times for a single QD parameter set in the $\hat{H}_{QD} + \hat{H}_{SO}$ system is approximately 25 to 30 hrs on a 2.7 GHz Intel Core i7 Macbook Pro with 16 GB RAM.

As an example, Fig. B.2 displays the absolute difference in the relaxation rates between the original, "full" states and the truncated states for full interaction strength ($\alpha = 1$) in the non-SO system due to the TA-PZ electron-phonon interaction. For each compared point the absolute difference in $1/T_1$ is between 0.002 and 0.01 ns^{-1}. The relative change is between 0.5 and 2%, except at $B = 1.4$ T where it is 3.3%. (Note that the relaxation rate at $B = 1.4$ T is small relative to the peak value.)

The quantitative differences in the relaxation and decoherence rates of the QD system with the full eigenstates versus the truncated eigenstates are small. Qualitatively the trends remain the same. Trunctating the H_{QD} eigenstates to within 0.01% of their original weight significantly reduces the basis size and therefore the computation time required to obtain the decay rates. We believe this approximation

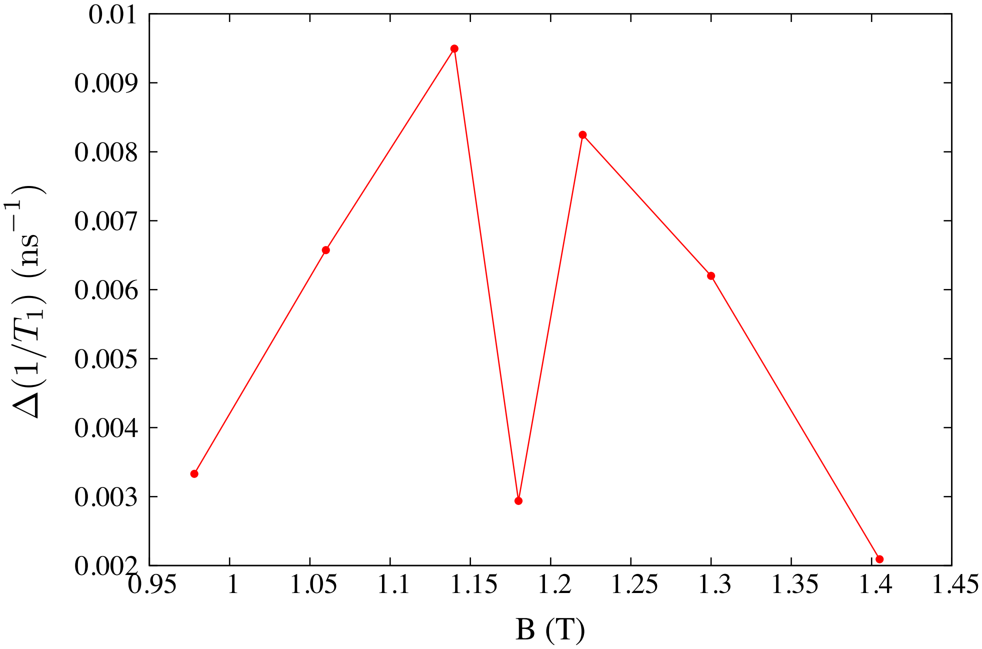

Figure B.2: Difference of relaxation rates between the QD system with full H_{QD} eigenstates and the QD system where the H_{QD} eigenstates have been truncated to within 0.01 % of the original weight for the TA-PZ electron-phonon interaction.

is justified in calculating the decay rates of the interacting QD system.

Appendix C

Numerical Integration

The integrals over r, r', z, z', and ϕ_q in the expression

$$\mathbb{I}_{ijkl}^{nm,\nu} = \int_0^{\pi} d\phi_q \sin\phi_q \, \mathbb{I}_{\theta_q}^{\nu}(\phi_q) \, \mathbb{I}_r^{ij}(\phi_q) \, \mathbb{I}_{r'}^{lk}(\phi_q) \, \mathbb{I}_z(\phi_q) \, \mathbb{I}_{z'}^{*}(\phi_q), \tag{C.1}$$

(see Eq. (4.53) and surrounding text in Sec. 4.3 for details), were performed using Maple(TM) 14.00 for each interaction type, $\nu = \{\text{LA-DP, LA-PZ, TA-PZ}\}$. The order of integration is irrelevant since the integrals are all independent of each other with the exception of their dependence on the variable ϕ_q. The integral over ϕ_q is therefore performed last.

In all cases, Maple(TM) numerically evaluates the integrals in the following default manner[1]: The integration is first passed to a one-dimensional NAG (Numerical Algorithms Group) integration routine, either nag_1d_quad_gen (d01ajc), nag_1d_quad_osc (d01akc), or nag_1d_quad_inf (d01amc). The first routine, d01ajc, is a general purpose integrator limited to a finite integration interval and can be used to evaluate integrands which contain singularities. The second routine, d01akc, is also evaluated over a finite interval. It can accommodate integrands with oscillatory behaviour. The third routine, d01amc, evaluates integrals over a semi-infinite or infinite interval. Further details of these routines can be found at www.nag.com. In Maple(TM), these NAG routines are compiled in a C library.

The above NAG routines are limited in their precision to 15 or fewer digits. In the event that greater precision is required, native Maple routines are employed as follows: The Clenshaw-Curtis quadrature method (CCquad) is applied first. This method is based on expanding the integrand into Chebyshev polynomials, which are then integrated term-by-term [118]. If the integrand contains singularities in or near the interval of integration, the interval is subdivided and an adaptive double-exponential quadrature method (Dexp) is called.

---

[1] Maple(TM) 14.00 Help (© Maplesoft, a division of Waterloo Maple Inc., Waterloo, Ontario)

Bibliography

[1] M. A. Nielsen and I. L. Chuang, *Quantum Computation and Quantum Information* (Cambridge University Press, Cambridge, 2000).

[2] D. Loss and D. DiVincenzo, Physical Review A **57**, 120 (1998).

[3] M. E. Reimer *et al.*, Physica E-Low-Dimensional Systems & Nanostructures **40**, 1790 (2008).

[4] J. Jefferson, M. Fearn, D. Tipton, and T. Spiller, Physical Review A **66**, 042328 (2002).

[5] J. Jefferson and W. Hausler, Molecular Physics Reports **17**, 81 (1997).

[6] S. Tarucha, D. Austing, T. Honda, R. vanderHage, and L. Kouwenhoven, Physical Review Letters **77**, 3613 (1996).

[7] H. Chang, R. Grundbacher, D. Jovanovic, J. Leburton, and I. Adesida, Journal of Applied Physics **76**, 3209 (1994).

[8] A. M. See *et al.*, Applied Physics Letters **96**, 112104 (2010).

[9] H. A. Engel, L. P. Kouwenhoven, D. Loss, and C. M. Marcus, Quantum Information Processing **3**, 115 (2004).

[10] J. Taylor *et al.*, Nature Physics **1**, 177 (2005).

[11] S. Foletti, H. Bluhm, D. Mahalu, V. Umansky, and A. Yacoby, Nature Physics **5**, 903 (2009).

[12] E. A. Laird *et al.*, Physical Review B **82**, 075403 (2010).

[13] M. V. G. Dutt *et al.*, Physical Review B **74**, 125306 (2006).

[14] J. Berezovsky, M. H. Mikkelsen, N. G. Stoltz, L. A. Coldren, and D. D. Awschalom, Science **320**, 349 (2008).

[15] D. Press, T. D. Ladd, B. Zhang, and Y. Yamamoto, Nature **456**, 218 (2008).

[16] A. Greilich *et al.*, Nature Physics **5**, 262 (2009).

[17] G. Cao *et al.*, Nature Communications **4**, 1401 (2013).

[18] T. Fujisawa, D. G. Austing, Y. Tokura, Y. Hirayama, and S. Tarucha, Nature **419**, 278 (2002).

[19] A. Bertoni, M. Rontani, G. Goldoni, and E. Molinari, Physical Review Letters **95**, 066806 (2005).

[20] J. I. Climente, A. Bertoni, M. Rontani, G. Goldoni, and E. Molinari, Physical Review B **74**, 125303 (2006).

[21] L. Jacak, P. Hawrylak, and A. Wojs, *Quantum Dots* (Springer-Verlag, Berlin, 1998).

[22] U. Meirav, M. Kastner, and S. Wind, Physical Review Letters **65**, 771 (1990).

[23] L. P. Kouwenhoven, A. Johnson, N. Vandervaart, C. Harmans, and C. Foxon, Physical Review Letters **67**, 1626 (1991).

[24] J. Kyriakidis, M. Pioro-Ladriere, M. Ciorga, A. Sachrajda, and P. Hawrylak, Physical Review B **66**, 035320 (2002).

[25] D. Hessman, P. Castrillo, M.-E. Pistol, C. Pryor, and L. Samuelson, Applied Physics Letters **69**, 749 (1996).

[26] D. R. Stewart, D. Sprinzak, C. M. Marcus, C. I. Duruöz, and J. S. Harris Jr., Science **5**, 1788 (1997).

[27] T. Fujisawa *et al.*, Science **282**, 932 (1998).

[28] T. Fujisawa, D. G. Austing, Y. Tokura, Y. Hirayama, and S. Tarucha, Journal of Physics: Condensed Matter **15**, R1395 (2003).

[29] T. Fujisawa, Y. Tokura, and Y. Hirayama, Physical Review B **63**, 081304(R) (2001).

[30] C. Volk *et al.*, Nature Communications **4**, 1753 (2013).

[31] J. Gupta, D. Awschalom, X. Peng, and A. Alivisatos, Physical Review B **59**, 10421 (1999).

[32] J. Petta *et al.*, Science **309**, 2180 (2005).

[33] D. Press *et al.*, Nature Photonics **4**, 367 (2010).

[34] F. H. L. Koppens *et al.*, Nature **442**, 766 (2006).

[35] K. C. Nowack, F. H. L. Koppens, Y. V. Nazarov, and L. M. K. Vandersypen, Science **318**, 1430 (2007).

[36] S. Amasha *et al.*, Physical Review Letters **100** (2008).

[37] S. Das Sarma, M. Freedman, and C. Nayak, Physics Today **59**, 32 (2006).

[38] K. Berggren, C. Besev, and Z. Ji, Physica Scripta **T42**, 141 (1992).

[39] S. L. Sondhi, A. Karlhede, S. A. Kivelson, and E. H. Rezayi, Physical Review B **47**, 16419 (1993).

[40] K. Moon *et al.*, Physical Review B **51**, 5138 (1995).

[41] H. Saarikoski, A. Harju, M. J. Puska, and R. M. Nieminen, Physical Review Letters **93**, 116802 (2004).

[42] H. Saarikoski and A. Harju, Physical Review Letters **94**, 246803 (2005).

[43] N. Yang, J. L. Zhu, Z. Dai, and Y. Wang, arXiv:cond-mat/0701766v1 [cond-mat.str-el] (2007).

[44] T. Oosterkamp *et al.*, Physical Review Letters **82**, 2931 (1999).

[45] H. Fertig *et al.*, Physical Review B **55**, 10671 (1997).

[46] L. Brey, H. A. Fertig, R. Côté, and A. H. MacDonald, Physical Review Letters **75**, 2562 (1995).

[47] S. Barrett, G. Dabbagh, L. Pfeiffer, K. West, and R. Tycko, Physical Review Letters **74**, 5112 (1995).

[48] E. Aifer, B. Goldberg, and D. Broido, Physical Review Letters **76**, 680 (1996).

[49] P. Khandelwal *et al.*, Physical Review Letters **86**, 5353 (2001).

[50] G. Gervais *et al.*, Physical Review Letters **94** (2005).

[51] S. Muehlbauer *et al.*, Science **323**, 915 (2009).

[52] A. D. Guclu, P. Potasz, O. Voznyy, M. Korkusinski, and P. Hawrylak, Physical Review Letters **103** (2009).

[53] S.-R. E. Yang, N. Y. Hwang, and S. Park, Physical Review B **72** (2005).

[54] A. Petkovic and M. V. Milovanovic, Physical Review Letters **98**, 066808 (2007).

[55] M. V. Milovanovic, E. Dobardzic, and Z. Radovic, Physical Review B **80**, 125305 (2009).

[56] P. A. Maksym and T. Chakraborty, Physical Review Letters **65**, 108 (1990).

[57] S. Reimann and M. Manninen, Reviews of Modern Physics **74**, 1283 (2002), Reviews of Modern Physics.

[58] M. Florescu and P. Hawrylak, Physical Review B **73** (2006).

[59] M. Genkin, E. Waltersson, and E. Lindroth, Physical Review B **79**, 245310 (2009).

[60] H. Ibach and H. Luth, *Solid-State Physics*, 3rd ed. (Springer - Verlag, 2003).

[61] A. Bertoni, M. Rontani, G. Goldoni, F. Troiani, and E. Molinari, Applied Physics Letters **85**, 4729 (2004).

[62] B. G. Streetman and S. Banerjee, *Solid State Electronic Devices*, 5th ed. (Prentice Hall, Upper Saddle River, N.J., 1999).

[63] M. Yu, Peter Y.; Cardona, *Fundamentals of Semiconductors*, 3rd ed. (Springer - Verlag, 2001).

[64] I. Strzalkowski, S. Joshi, and C. R. Crowell, Applied Physics Letters **28**, 350 (1976).

[65] P. Hai, W. Chen, I. Buyanova, H. Xin, and C. Tu, Applied Physics Letters **77**, 1843 (2000).

[66] V. Fock, Zeitschrift für Physik **47**, 446 (1928).

[67] C. Darwin, Mathematical proceedings of the Cambridge Philosophical Society. **27**, 86 (1930).

[68] C. J. Stevenson and J. Kyriakidis, Physical Review B **83**, 115306 (2011).

[69] M. Abramowitz and I. A. Stegun, *Handbook of Mathematical Functions: With formulas, graphs, and mathematical tables* (Dover Publications, New York, 1965).

[70] C. J. Stevenson and J. Kyriakidis, Physical Review B **84**, 075303 (2011).

[71] A. D. Güçlü and C. J. Umrigar, Physical Review B **72**, 045309 (2005).

[72] J. J. Sakurai and S. F. Tuan, *Modern Quantum Mechanics*, Rev. ed. (Addison-Wesley Pub. Co., Reading, Mass., 1994).

[73] J. J. Sakurai, *Advanced Quantum Mechanics* (Addison-Wesley Pub. Co, Reading, Mass., 1967).

[74] J. Könemann, R. J. Haug, D. K. Maude, V. I. Fal'ko, and B. L. Altshuler, Phys Rev Lett **94**, 226404 (2005).

[75] S. Giglberger *et al.*, Physical Review B **75**, 035327 (2007).

[76] L. Meier *et al.*, Nature Physics **3**, 650 (2007).

[77] S. M. Huang *et al.*, Physical Review B **84**, 085325 (2011).

[78] M. Li *et al.*, Solid State Communications **151**, 1958 (2011).

[79] M. P. Walser *et al.*, Physical Review B **86**, 195309 (2012).

[80] P. P. Ruden *et al.*, IEEE Transactions on Electron Devices **37**, 2171 (1990).

[81] R. Winkler, *Spin-Orbit Coupling Effects in Two-Dimensional Electron and Hole Systems* (Springer-Verlag Berlin Heidelberg, 2003).

[82] J. Nitta, T. Akazaki, H. Takayanagi, and T. Enoki, Physical Review Letters **78**, 1335 (1997).

[83] G. Engels, J. Lange, T. Schapers, and H. Luth, Physical Review B **55**, R1958 (1997).

[84] D. Grundler, Phys Rev Lett **84**, 6074 (2000).

[85] M. Studer, G. Salis, K. Ensslin, D. C. Driscoll, and A. C. Gossard, Physical Review Letters **103**, 027201 (2009).

[86] G. Dresselhaus, Physical Review **100**, 580 (1955).

[87] E. P. O'Reilly, *Quantum theory of solids*The Taylor Francis Masters Series in Physics and Astronomy (Taylor Francis, London, 2002).

[88] J. Zhou, J. L. Cheng, and M. W. Wu, Physical Review B **75**, 045305 (2007).

[89] M. Studer *et al.*, Physical Review B **82**, 235320 (2010).

[90] I. Zutic, J. Fabian, and S. Das Sarma, Reviews of Modern Physics **76**, 323 (2004), Reviews of Modern Physics.

[91] Y. Bychkov and E. Rashba, JETP Letters **39**, 78 (1984).

[92] M. D'yakonov and V. Perel', Soviet Physics, Solid State **13**, 3023 (1972).

[93] E. A. de Andrada e Silva, G. Larocca, and F. Bassani, Physical Review B **50**, 8523 (1994).

[94] E. A. de Andrada e Silva, G. C. LaRocca, and F. Bassani, Physical Review B **55**, 16293 (1997).

[95] R. de Sousa and S. Das Sarma, Physical Review B **68**, 155330 (2003).

[96] L. Challis, editor, *Electron-Phonon Interactions in Low-Dimensional Structures*Series on Semiconductor Science and Technology (Book 10) (Oxford University Press, USA, 2003).

[97] K. Blum, *Density Matrix Theory and Applications*, 2nd ed. (Plenum Press, New York, 1996).

[98] U. Bockelmann, Physical Review B **50**, 17271 (1994).

[99] J. Cheng, M. Wu, and C. Lu, Physical Review B **69**, 115318 (2004).

[100] J. I. Climente, A. Bertoni, G. Goldoni, and E. Molinari, Physical Review B **74**, 035313 (2006).

[101] J. I. Climente, A. Bertoni, G. Goldoni, and E. Molinari, Physical Review B **75**, 245330 (2007).

[102] J. S. Blakemore, Journal of Applied Physics **53**, R123 (1982).

[103] G. D. Mahan, *Many-Particle Physics*, 3rd ed. (Kluwer Academic/Plenum Publishers, New York, 2000).

[104] J. D. Zook, Physical Review **136**, A869 (1964).

[105] N. Goldenfeld, *Lectures on phase transitions and the renormalization group*, Frontiers in Physics Vol. 85 (Addison-Wesley, Advanced Book Program, Reading, Mass., 1992).

[106] A. Khaetskii, D. Loss, and L. Glazman, Physical Review B **67**, 195329 (2003).

[107] G. Burkard, R. H. Koch, and D. P. DiVincenzo, Physical Review B **69**, 064503 (2004).

[108] J. Kyriakidis and G. Burkard, Physical Review B **75**, 115324 (2007).

[109] A. Abragam, *The Principles of Nuclear Magnetism* (Oxford University Press, 1961).

[110] V. May and O. Kühn, *Charge and Energy Transfer Dynamics in Molecular Systems*, 3rd ed. (Wiley-VCH, Weinheim, 2011).

[111] R. K. Nagle, E. B. Saff, and A. D. Snider, *Fundamentals of differential equations and boundary value problems*, 4th ed. (Pearson Addison Wesley, Boston, 2004).

[112] D. Stich *et al.*, Physical Review B **76**, 073309 (2007).

[113] W. Knap *et al.*, Physical Review B **53**, 3912 (1996).

[114] J. J. Krich and B. I. Halperin, Physical Review Letters **98**, 226802 (2007).

[115] J. B. Miller *et al.*, Physical Review Letters **90**, 076807 (2003).

[116] G. Guennebaud *et al.*, Eigen v3, http://eigen.tuxfamily.org, 2010.

[117] C. J. Stevenson and J. Kyriakidis, Canadian Journal of Physics **89**, 213 (2011).

[118] K. O. Geddes and G. Labahn, Proceedings of the First Asian Technology Conference in Mathematics , 377 (1995).